Nanoscaled SnO_2 sensors for analysis of VOCs: Quasi-online monitoring of dissolved VFAs in biogas fermentation processes

Zur Erlangung des akademischen Grades eines

DOKTORS DER INGENIEURWISSENSCHAFTEN

von der KIT-Fakultät für Chemieingenieurwesen und Verfahrenstechnik des Karlsruher Instituts für Technologie (KIT)
genehmigte

DISSERTATION

von
(M.Sc.) Binayak Ojha
aus Kathmandu, Nepal

Tag der mündlichen Prüfung: 16.12.2024

Erstgutachter: Prof. Dr. -Ing. Matthias Franzreb

Zweitgutachter: Prof. Dr. rer. nat. Heinz Kohler

ABSTRACT

In the first part of this thesis, a comparative study of the gas sensing performance of two thermo-cyclically operated metal oxide gas sensor arrays to volatile organic compounds (VOCs) is presented. This was possible by using a silicon rubber membrane-based carrier gas probe which enables sensing tests with evaporated VOCs (acetic acid, propionic acid, ethanol, and acetone) dissolved in water. Each of the sensor arrays comprises a pure SnO_2 and three different SnO_2/additive-layers (additives: alumina, Yttria-stabilized zirconia (YSZ), sodium super ion conductor (NASICON)) as sensing layers which were separately deposited as thick-film layers in Pt-Interdigtal Electrodes (IDE) of fourfold sensor array chip by use of a micro-dispensing technique. These layers of the two sensor arrays differ by the SnO_2 powder synthesis routes applied, namely the Flame Spray Pyrolysis (FSP) and the Sol-Gel (SG) technique. This allowed comparative studies of the influence of the layer morphology on the VOCs sensing characteristics. The morphologies were investigated by Environmental Scanning Electron Microscopy (ESEM) analysis and Energy-Dispersive X-Ray Spectroscopy (EDS).

The resulting Conductance-over-Time-Profiles (CTPs), as produced by thermo-cyclic operation, highlighted better sensitivities of most of the FSP-layers to all the investigated analytes compared to the SG-layers. Furthermore, the CTP-shapes of the FSP-layers show clearly enhanced specificity representing the individual analyte components. Correspondingly, these results promise better chemical analysis capability of dissolved VOCs by numerical analysis of the CTP of the FSP-layers.

In the second part of the thesis, for the first time, a quasi-online method for monitoring of dissolved volatile fatty acids (VFAs) in biogas fermentation processes was demonstrated by combined use of above mentioned thermo-cyclically operated sensor arrays and the carrier gas probe. For sensitive determination of the dissolved VFAs like acetic or propionic acid in presence of high concentrations of biogas components like CO, CH_4 or H_2, at first, a pre-treatment routine of the fermentation sample was introduced to get rid of those physically dissolved biogases without the loss of the VFAs. Next, the CTPs of the eight different SnO_2/additives-layers (four layers on each chip) were measured simultaneously at exposure to the gases extracted from the pre-treated fermentation sample. This allowed variation of the fraction of undissociatively dissolved VFAs in the fermentation sample, their concentration in the carrier gas, and consequently allowed to investigate their influence on the CTPs.

Almost all the investigated SnO_2/additive-layers showed CTP-features which could be clearly correlated with the undissociated VFA content measured at different pH-values even at concentrations well below 120 ppm as referenced by GC analysis measurements. This detection limit is well below the inhibitory concentration limit for biogas fermentation processes. As expected, most pronounced CTPs representing the actual VFAs situation in the fermentation sample were measured at pH 3, which is well below the pKa of the VFAs. Like the measurement with model VOCs, the FSP-layers highlighted clearly better sensitivity compared to SG-layers and provided CTP specificity of higher quality. This was interpreted to be the consequence of the extremely fine, scarcely agglomerated grain morphology of FSP-layers and their very narrow grain size distribution which provide better conditions for enhanced gas specific surface reactions. In particular, among the SnO_2/additives investigated, the CTP-features of the SnO_2(FSP)/NASICON-layer and SnO_2(SG)/NASICON-layer were found to show the best specificity to acetic and propionic acid. This impressive sensing behaviour could be related to the role of NASICON which could cause amplification of the sensitivity behaviour by Na^+-e^- interactions across the SnO_2-NASICON interface, as already assumed in a hypothetical model presented in earlier studies.

In this work, for the first time, it was demonstrated that quasi-online monitoring of VFAs using thermo-cyclically operated metal oxide gas sensors is possible and this enables early warning of VFA-development in biogas fermentation processes.

ZUSAMMENFASSUNG

Im ersten Teil dieser Thesis wird eine vergleichende Untersuchung der Gassensoreigenschaften von zwei thermozyklisch betriebenen Metalloxid-Gassensorarrays für flüchtige organische Verbindungen (VOC) vorgestellt. Mithilfe einer mit einer Silikonmembran bespannten Trägergas-Sonde konnten Sensitivitätstests von in Wasser gelösten flüchtigen Kohlenwasserstoffen (VOC) wie Essigsäure, Propionsäure, Ethanol und Aceton an diesen Gassensorarrays durchgeführt werden. Jedes der beiden Sensorarrays besteht aus je einer sensitiven Wirkschicht aus reinem SnO_2 und drei verschiedenen SnO_2/Additiv-Kompositen (Additive: Aluminiumoxid, Yittrium stabilisiertes Zirkondioxid (YSZ) und NASICON (NAtrium Super Ionic CONductor)), die jeweils als Dickschicht mittels einer Mikrodispenstechnik auf eine Interdigital-Elektrodenstruktur aufgebracht wurden. Die Schichten der beiden Sensorarrays unterscheiden sich durch die beiden Syntheseverfahren der SnO_2-Pulver, nämlich die Flammen-Sprüh-Pyrolyse (FSP) und die Sol-Gel (SG)-Technik. Dies ermöglichte erstmals vergleichende Studien zum Einfluss der Schicht-Morphologie auf die VOC-Sensitivitätseigenschaften (Schichtwiderstandsänderung).

Die unterschiedlichen Morphologien der Schichten wurde durch Rasterelektronenmikroskopie (Environmental Scanning Electron Microscope) und energiedispersive Röntgenspektrometrie (EDS) untersucht.

Die resultierenden Leitwert-Zeit-Profile (LZP), die durch Sensitivitätsmessungen im thermozyklischen Betrieb erhalten werden, zeigen insbesondere eine deutlich bessere Empfindlichkeit der meisten FSP-Schichten gegenüber allen untersuchten Analyten im Vergleich zu den SG-Schichten. Darüber hinaus zeigen die LZP-Merkmale der FSP-Schichten deutlich verbesserte Spezifität gegenüber den einzelnen Analyt-Komponenten. Entsprechend versprechen diese Ergebnisse eine bessere chemische Analysefähigkeit von gelösten VOCs, wenn die LZP der FSP-Schichten numerisch analysiert werden.

Im zweiten Teil der Thesis konnte erstmals eine quasikontinuierliche Methode zur Überwachung der Entwicklung von gelösten flüchtigen Fettsäuren (VFAs) in Biogas-Fermentationsprozessen durch die kombinierte Anwendung der oben genannten thermozyklisch betriebenen Sensorarrays mit einer Trägergas-Sonde demonstriert werden. Zur empfindlichen Bestimmung der gelösten VFA wie Essig- oder Propionsäure in Gegenwart hoher Konzentrationen von Biogas-Komponenten wie CO, CH_4 oder H_2 musste zunächst ein Konditionierungsverfahren der Fermentationsprobe eingeführt werden, um diese physikalisch

gelösten Biogase ohne Verlust der VFA zu entfernen. Danach wurden die LZP der acht verschiedenen SnO_2/Additiv-Kompositen (vier Schichten auf jedem Chip) während der Exposition mit den aus der vorbehandelten Fermentationsprobe extrahierten Gasen gemessen. Diese Messungen wurden bei verschiedenen pH-Werten der Fermentationsbrühe durchgeführt, um den Einfluss der Änderungen der Gaszusammensetzung infolge der Variation des Anteils nicht-dissoziativ gelöster VFA in der Fermentationsprobe und ihrer Konzentration im Trägergas auf die LZP zu untersuchen.

Nahezu alle untersuchten SnO_2/Additiv-Kompositen zeigen LZP-Merkmale, die deutlich mit dem undissoziierten VFA-Gehalt bei verschiedenen pH-Werten korreliert werden konnten. Dies war selbst bei Konzentrationen möglich, die weit unter 120 ppm liegen, wie durch GC-Referenzmessungen gezeigt wurde. Die Nachweisgrenze liegt folglich weit unterhalb der hemmenden Konzentrationsgrenze von VFA für Biogas-Fermentationsprozesse. Die deutlichsten LZP-Merkmale, die die aktuelle VFA-Situation in der Fermentationsprobe repräsentieren, wurden wie erwartet bei einem pH-Wert von 3 gemessen. Dieser Wert liegt weit unterhalb des pKs-Werts der VFA.

Die FSP-Schichten wiesen im Vergleich zu den SG-Schichten eine deutlich höhere Empfindlichkeit auf und zeigten LZP-Spezifitäten von höherer Qualität, ähnlich wie dies anhand der Messungen mit Modell-VOC bereits beobachtet worden war. Dies wurde als Folge der extrem feinen, kaum agglomerierten Kornmorphologie der FSP-Schichten und ihrer sehr engen Korngrößenverteilung interpretiert, die bessere Bedingungen für erhöhte gasspezifische Oberflächenreaktionen bieten. Insbesondere zeigen unter den untersuchten SnO_2/Additiv-Schichten die LZP-Merkmale der SnO_2(FSP)/NASICON- und SnO_2(SG)/NASICON-Schichten die beste Spezifität für Essig- und Propionsäure. Dieses beeindruckende Sensorverhalten könnte auf die Rolle des NASICON zurückgeführt werden, das durch Na^+-e^- Wechselwirkung über die SnO_2/NASICON-Korngrenzen eine Verstärkung der molekülspezifischen Sensitivität bewirken könnte, wie dies in einem hypothetischen Modell in früheren Studien bereits vorgeschlagen wurde.

Damit wurde in dieser Arbeit zum ersten Mal gezeigt, dass die quasikontinuierliche Überwachung von gelöstem VFA in Biogas-Fermentationprozessen durch die Verwendung von thermozyklisch betriebenen Metalloxid-Gas-Sensoren möglich ist. Dies eröffnet eine frühzeitige Warnung vor der Entwicklung von VFA im Fermentierprozess.

ACKNOWLEDGEMENTS

Foremost, I would like to thank the Department of Chemical and Process Engineering at Karlsruhe Institute of Technology (KIT) for accepting my application for pursuing a doctoral degree. My sincere gratitude to my supervisors Prof. Dr. -Ing. Matthias Franzreb and Prof. Dr. rer. nat. Heinz Kohler. I thank them for their charismatic, constructive, and motivating guidance and for their patience at times.

A major part of this doctoral work is based on my research activities in EBIPREP project between August 2017 to October 2020. I would like to thank Prof. Dr. rer. nat. Heinz Kohler again for his great trust in my work and for providing opportunity to work on the project. In addition, with gratitude, I would also like to acknowledge EBIPREP collaboration project (www.ebiprep.eu, EU International Programme INTERREG V Oberrhein, 2017-2020) for providing financial support for this work.

I would like to acknowledge all the faculty members and staff of the Faculty of Electrical Engineering and Information Technology and the Center of Applied Research at Karlsruhe University of Applied Sciences for their support throughout my work.

I am grateful to Dr. Margarita Aleksandrova for her efforts in preparing various metal oxide powders for screening tests and especially for preparation of the NASICON-powders.

Further, I would like to extend my thanks to Prof. Dr. Andreas Güntner, Mr. Sebastian Abbeg and Mr. Nicolay Pineau from Dept. of Mechanical and Process Engineering, ETH Zürich (CH) for providing SnO_2 powder prepared by Flame Spray Pyrolysis (FSP) method.

I would like to thank Mr. Jan Wernthal and Mr. Gerd Westermann for their exceptional support in constructing carrier gas probe and other various mechanical parts of the measurement setup.

I would like to extend my sincere thanks to Dr. Matthias Schwotzer from Institute of Functional Interface (IFG), KIT for his close association throughout the thesis work and for his expertise support in ESEM measurements and EDS analysis.

A special thanks to Regina Brämer from Offenburg University of Applied Sciences for making the GC analysis of fermentation samples.

In addition, a special gratitude to the former colleagues of the ISIS-sensor group; Dr Navas Illyaskutty, Dr. Xin Zhang, and Mr. Jens Knoblauch for many highly stimulating discussions and all the memorable moments we had during several research projects and in all day work.

No gratitude is sufficient to repay the endless love and support of my parents and family. I thank them for giving me the drive and passion to pursue my goals.

PREFACE

Biogas fermentation is very complex process of successive and interacting degradation steps. A reliable monitoring of the key process parameters allows precise control of the biochemical process, which is crucial to achieve efficient, reliable, and economically profitable biogas production.

Volatile fatty acids (VFAs) are one of the substances formed during the fermentation process, but their accumulation is highly undesired because high VFA concentrations strongly inhibit the fermentation process. In ideal case, these intermediates are consumed to produce biogas and other intermediates, but this rate of degradation is influenced by the composition of the feed materials. Thus, a stable and undisturbed fermentation process usually exhibits very low VFA concentrations. This means, there is a direct correlation between fermentation process stability and VFAs concentration, and correspondingly, it is well acknowledged that VFAs provide quick and reliable information about the current process state [1–11].

Up to now, estimation of this important information about the actual state of VFA concentrations is based on classical lab-analysis methods in which the samples are extracted from the fermentation reactor from time to time. This periodic procedure is costly and time consuming. There is no reliable and cost-effective method established for in-situ monitoring of VFAs. Combining the information of the actual process state provided by the VFAs with other process parameters like pH would enable early warning of such undesired development of VFAs formation and allow development of reliable and robust control strategies for automated process optimization.

Thus, continuous, and reliable measurement of VFAs in biogas fermentation processes is of high scientific relevance and high practical significance.

In this doctoral thesis work, done in the framework of EBIPREP international collaboration project (www.ebiprep.eu) [12], for the first time a sensor system based on the combination of metal oxide gas sensors with a carrier gas probe for quasi online analysis of VFAs in biogas fermentation processes was developed.

The core aim of the EBIPREP was to develop new fermentation processes with the usage of the wood juice extracted during the mechanical drying process of wood chips. In addition to the development of a sensor system for VFA analysis in fermentation processes, which is the topic

of this thesis, the investigation of wood chip gasification and catalytic cleaning of syngas was studied as well by EBIPREP. In this context, I could also contribute to the development of a novel and very sensitive method for online monitoring of tar in syngas[13]. In general, tar is a highly undesired byproduct in gasification processes.

Overall, the major focus of EBIPREP-studies was on the use of wood juice and dried beer marc as co-substrates in biogas fermentation processes as well as on use of wood juice in the biotechnological production of valuable products such as enzyme production.

TABLE OF CONTENTS

LIST OF FIGURES

LIST OF TABLES

LIST OF ABBREVIATIONS

Abbreviation	Definition
CGP	Carrier Gas Probe
CTP	Conductance over Time Profile
DAC	Digital to Analog Converter
DIO	Digital Input/Output
EDS/EDX	Energy Dispersive Spectroscopy
EPR	Electron Paramagnetic Resonance
ER	Eley-Rideal
ESEM	Environmental Scanning Electron Microscope
FEG	Field Emission Gun
FFT	Fast Fourier Transform
FSP	Flame Spray Pyrolysis
FTIR	Fourier Transform Infrared Spectroscopy
GC	Gas Chromatography
HPLC	High-performance Liquid Chromatography
IDE	Interdigital Electrodes
IR	Infrared
LH	Langmuir-Hinshelwood
MCA	Multi Component Analysis
MFC	Mass Flow Controller
MO	Metal Oxide
MOG	Metal Oxide Gas Sensors
MvK	Mars van Krevelen
PCA	Principal Component Analysis
SA	Sensor Array
SG	Sol Gel
TA	Total Alkalinity
TPD	Temperature Programmed Desorption
UV	UltraViolet
VFAs	Volatile Fatty Acids
VOCs	Volatile Organic Compounds
XRD	X-ray Diffractometer

LIST OF SYMBOLS

Symbol	Definition
$Go_x(air)$	Conductance measured at sampling point x on exposure to dry synthetic air
$G_x(c)$	Conductance measured at sampling point x on exposure to analyte concentration c
K_A	Equilibrium constant of gas species A
K_B	Equilibrium constant of gas species B
K_H	Henry's law constant
N_S	Charge carrier concentration
O^-_{ads}	Oxygen surface states
$O_{2\ ads}$	Adsorbed oxygen molecule
$O^-_{2\ ads}$	Oxygen surface states
O^{2-}_{ads}	Oxygen surface states
$V_{\ddot{O}}$	Oxygen vacancy
k	Reaction rate constant
k_B	Boltzmann constant
k_{ads}	Rate of adsorption
k_{des}	Rate of desorption
k_{diff}	Rate of diffusion
p_A	Partial pressure of gas species A
p_B	Partial pressure of gas species B
ε_0	absolute permittivity
ε_r	relative permittivity
θ_A	Fractional coverage of gas species A
θ_B	Fractional coverage of gas species B
ΔE_{ads}	Adsorption enthalpy
ΔE_{des}	Desorption enthalpy
ΔrG	Change in Gibbs free reaction energy
ΔrH	Reaction enthalpy
ΔrS	Change in entropy
c	Gas concentration
D	Grain diameter
e	Electron charge
E_a	Activation energy

E_C	Conduction band
Go(dry air)	CTP measured on exposure to dry synthetic air
Go(hum. air)	CTP measured on exposure to humidified synthetic air
L_D	Debye length
O^{2-}	Oxide ion
R_H	Hydrocarbon molecule
R_O	Oxidation product of hydrocarbon
G	Conductance
T	Temperature
p	Partial pressure
$p(O_2)$	Partial pressure of oxygen
α	Pre-exponential factor in power law
β	Power law exponent
θ	Fractional coverage
σ	Electrical conductivity

1. INTRODUCTION

1.1. Background

Different types of gas sensors, namely optical, electrochemical, and chemoresistive have been reported in literature. Optical sensors offer accurate detection and discrimination ability of multicomponent test gases, but their instrumentation, in most cases, is sophisticated and the service efforts in case of applications in harsh environments increase the cost of operation. Electrochemical sensors are generally relatively economic, but several types of this sensor family are unsuitable for long-term applications.

In contrast, chemoresistive gas sensors based on solid state semiconductor materials offer considerable advantage. They are inexpensive to produce, easy to miniaturize, rugged, reliable, and can be designed to operate over a range of temperature conditions including high temperatures as well. These semiconductor sensors can be produced in arrays to allow multi-sensing with advances in sensitivity. In some cases, detection limits approach part-per-billion (ppb) levels [14]. Tin oxide, zinc oxide, and titanium oxide are most widely used in gas sensing application.

Due to their attraction with respect to sensing behaviour and price, metal oxide gas sensors (MOG) have undergone extensive research. Since they were patented in 1962, they were established as the dominant choice for solid state gas detectors. Nowadays, MOG are well established sensors which are widely used in many applications like hazardous gas leakage monitoring [15], early fire detection in electrical installations [16], flue gas analysis in wood combustion [17], food quality control [18], environmental monitoring [19], industrial emission monitoring and control [20], and even in biomedical applications like breath analysis [21, 22].

Meanwhile, several million devices are applied worldwide per year [23] due to their high sensitivity to many oxidizable or reducible gas components [24, 25], their rather good long-term stability and their simple operation at relatively low costs.

Nevertheless, the lack of selectivity of pure metal oxides (MOs) [26] limits its practical applications. However, it is very well known that the selectivity of the MO as sensing materials can be tuned by varying the crystal structure and morphology using different synthesis techniques. Additionally, the sensitivity as well as the selectivity of the MOG can be further modified by addition of metals or other MOs in the range of several weight percent related to

the matrix MO sensing material, by varying the operation temperature over time (temperature modulation), and by varying the layer thickness. Intensive research in the last three decades were focused on the influence of the grain size of the matrix material (mostly SnO_2 or ZnO) on the gas sensitivity in general and how sensitivity to specific gas components of interest can be cultivated by additives in nanoscaled distribution.

However, despite of this high level of knowledge about the sensing effects, there are still enormous research activities running to gain a deeper understanding of the influence of the material morphologies on the surface processes which control the sensor behaviour [27]. Simultaneously, there has been continuous evolution of advanced sensor fabrication to make this type of sensor also available as microstructure systems integrated in microelectronic devices [28] following the idea to utilize further improved sensor chips for more sophisticated tasks in the field of gas analysis. Additionally, this latter aspect needs to initiate further research efforts particularly to improve the understanding of the role of additives on the sensitivity in general, and on specific sensitivities required for special applications as well as on the long-term stability.

Another important aspect concerning utilizing MOG for analytical purposes is, how to extract as much chemical information as possible from those devices. MOG are usually operated at fixed temperature in the range of $300°C<T<450°C$. Despite careful selection of additives to attain specific sensitivities, for many applications those isothermally operated MOG lack sufficient discrimination capability to interfering gas components and, as a fact, do not enable gas component identification. Therefore, a single sensor element is considered unsuitable for chemical analysis. In the past, different signal analysis approaches like principal component analysis (PCA) [29, 30], artificial neural networks [30–33], multi component analysis (MCA) [34] and pattern recognition methods [34, 35] have been developed to improve the gas identification capability of those isothermally operated MOG.

Another approach on the way to enable chemical analysis by utilizing MOG is to operate the sensor in the non-isothermal mode [36, 37], i.e. to vary the operation temperature thermo-cyclically. In addition to enhanced gas analysis capabilities, the periodic variation of the sensor temperature improves sensitivity [38, 39] and can reduce long-term drift [40]. All these investigations confirmed, that the gas analysis capability of a single sensor can be further enhanced by non-isothermal operation, but, of course, by thermo-cyclic operation of an array of well-selected gas sensitive materials the analytical capability can be further optimized [41].

This method enables individual design of those thermo-cyclically operated sensor arrays for chemical analysis of various complex gas mixtures. It is the general scientific aim of this work, to proof if volatile fatty acids (VFAs) dissolved in biogas fermentation liquids can be monitored by analysis of the signals of those thermo-cyclically operated sensor arrays.

With increasing demand for non-fossil, green energy, interest in biogas production by fermentation of organic materials from domestic and industrial organic wastes is rapidly increasing. This well-established biotechnological method has promised to enable utilizing wide range of organic wastes, such as livestock waste [42–45], municipal solid waste [42], agricultural waste [44, 46, 47], food waste [45], etc., for anaerobic co-digestion to produce green energy which in future may lead to an extensive organic waste management.

However, in biogas fermentation processes, it is well acknowledged that the key sensitive indicators representing the process status used for early warning of a possible inhibition, are some undesired, intermediate products like the VFAs [1–6], which are expected to develop, depending on several parameters like composition of the feed. Acetic acid and propionic acid are considered as main VFAs of concern. Therefore, continuous monitoring of these individual VFAs provides quick and important information about the actual status of the anaerobic digestion process [48]. Knowledge of these indicators allows to take preventative action to optimise the fermentation process and, in critical cases, provides early warning of upcoming breakdowns [49].

The other way round, biotechnological cultivation of VFAs does also drive interesting applications. In recent years, different studies have shown that VFAs produced during anaerobic digestion of organic wastes are promising substrates for several second-step refinements, such as sustainable biofuels like biodiesel [50, 51] and biopolymers like Polyhydroxyalkanoates [52]. In this context, in contrast to the biogas fermentation process, the anaerobic digestion process is tweaked to produce VFAs as the major product and, correspondingly, a sensor system for monitoring of the production of the VFAs is highly desirable.

In the current scenario, there are no reliable sensors available for the online analysis of those individual VFAs in anaerobic biogas fermentation processes. The well established, commonly used offline methods for the analysis of the VFAs are titration methods [6, 53], gas chromatography (GC) [54] or high-performance liquid chromatography (HPLC) [3]. Analysis

by titration is the simplest method which provides the total VFA concentration at relatively low costs but fails to identify the concentration of the individual VFA components. In addition, there are some methods reported about the online analysis of VFA in anaerobic biogas processes by introduction of in-situ filtration techniques of the fermentation sample using a rotating pre-filter with an ultra-membrane in combination with a GC [2]. However, the major concerns with the membrane and filters are frequent fouling issues requiring a high level of maintenance. This limitation was overcome by extraction of the gas from the headspace of the reactor for GC analysis [49]. GC and HPLC methods are considered highly accurate and reliable but require high service cost and high efforts to avoid any contamination of the columns which may lead to drift in the baseline avoiding accurate analysis which makes them economically unfeasible. Similarly, several other online methods for VFA monitoring in anaerobic digestions using light sources, such as UV spectroscopy [55–57], near IR spectroscopy [58, 59], mid IR spectroscopy [3], and spectrofluorimetric spectroscopy [60] are reported. These analysis methods are without doubt interesting, however, again all these methods have in common that they are limited by their high service efforts, e.g. to keep deposition of molecules on the windows of the excitation chamber at an acceptable level.

Quite recently, some innovative biosensors, such as a bio-electrolytic sensor [61] and hybrid biosensor arrays [62] were reported for the online measurement of VFAs during anaerobic digestion processes. The former one is based on a microbial electrolysis cell. The sensor signal represents the total VFA concentration, which could be linearly correlated with VFA concentrations in the range 0- 7000 ppm. However, it does not allow the analysis of the individual VFAs. Stable and maintenance free operation of those sensors in the lab over five months is reported. However, for applications in the full-scale reactors an online sampling and sensing system is reported to be still missing. The biosensor array [62] works according to the amperometric principle. It integrates several analyte-sensing Pt-electrodes loaded with different enzymes selective for different analytes such as acetate, propionate, formate, ethanol, L-lactate and D-lactate. But a common procedure for sample preparation, which would be suitable for different sensing electrodes and different analytes like VFAs (acetate and propionate) and other targets such as formate, ethanol-lactate and D-lactate is not yet available. Nevertheless, the biosensor system is reported to be applied for long-term monitoring of a lab-scale biogas reactor (0.01 m^3) for a period of two months in the concentration range of 0-2500 ppm of acetic acid and 0-1500 ppm of propionic acid, respectively. However, the information about the maximum concentration limit of measurement is not available.

In this respect, it is very much desired to have a reliable sensor system for detecting the real time change of the individual VFA concentrations prior to complete process failure and to combine use of this analytical information with feedback control methods for an advanced, automated process control to avoid too high concentrations of such VFA-developments to enable optimization at every time of the biogas fermentation process [4].

Another, well established method for analysis of dissolved volatile organic compounds (VOCs) was already introduced in [36, 63]. Dissolved VOCs are extracted from the aqueous liquid phase via a carrier gas probe covered by a gas permeable membrane. This method was proven to be quite robust and provides the advantage that all ionic components per se cannot percolate the gas permeable membrane and, therefore, do not contribute to cross-sensitivities. At constant operation conditions, in good approximation the VOC concentration in the carrier gas (synthetic air) depends linearly on the VOC concentration in the liquid. The carrier gas loaded with the analyte is transported to a gas sensor cell comprising the MOG outside the fermentation reactor for analysis.

In general, excellent candidates for VOCs detection including VFAs in the biogas fermentation processes are the MOG. However, this type of sensor suffers on cross-sensitivities to a big number of oxidizable gas components, such as CH_4, CO, H_2, etc., which are all components of biogas in individually high concentrations. Further, the challenge is to analyse small concentrations (several 100 ppm) of VFAs with MOG in presence of high concentrations (several 10000 ppm) of biogas components. These demands (i) the investigation of new highly sensitive MO gas sensing materials which are perhaps more selective to those VFAs, (ii) application of the thermo-cyclic operation method in order to improve the analysis capability and (iii) a special monitoring procedure to get rid of the cross-sensitivities with the high concentrated biogas components.

1.2. Outline

The major content of this doctoral thesis work is based on key research activities of the EBIPREP project (see Preface), i.e. the development of a sensor system for the quasi online in-situ analysis of VFAs developed in the biogas fermentation processes. In general, the scope of the investigation can be divided into two parts.

In the first part, the influence of SnO_2 morphology on overall sensing behaviour of thermo-cyclically operated MOG when exposed to the evaporated model VOCs (acetic acid, propionic acid, ethanol, and acetone) dissolved in DI water, is studied. A silicon rubber membrane-based carrier gas probe is deployed for the extraction of the dissolved analyte. Gas sensitive layers are prepared using SnO_2 powder produced by Flame Spray Pyrolysis (FSP) technique, and alternatively, sol-gel (SG) method to enable investigation of the following aspects as illustrated in Fig. 1:

- Optimization of the measurement conditions, such as carrier gas flow rate and rate of temperature change of MOG for thermo-cyclic operation.
- The role of SnO_2 morphology related to overall sensitivity as well as on specificity of the conductance over time profiles (CTPs) to target VOC (analysis capability), i.e. correlation between the sensing behavior and morphological aspects, such as grain size, grain network, porosity, and thickness of the sensing layer.
- The influence of the additives (additives: alumina, Yttria-stabilized zirconia (YSZ), NASICON) related to the pure SnO_2 on the individual shape of the CTPs with respect to the target VOC, which again is expected to be strongly related to the analysis capability to be achieved with these composites.

Two four-fold sensor arrays are prepared, each comprising a pure SnO_2-layer and three different SnO_2/additive-layers (additives: alumina, YSZ, NASICON) as sensing layers. But the sensor array differs by the SnO_2 powder (FSP or SG prepared). Due to the different preparation route, the morphological and structural properties of SnO_2-layer and SnO_2/additives-layers are very different and therefore, are studied by environmental scanning electron microscopy (ESEM) and X-ray diffraction analysis (XRD). The distribution of the additives around SnO_2 matrix is investigated by an energy dispersive spectroscopy (EDS/EDX). Based on these results the individual morphologies of different layers, the CTPs measured on exposure to different model VOCs at optimized operational conditions are interpreted and discussed.

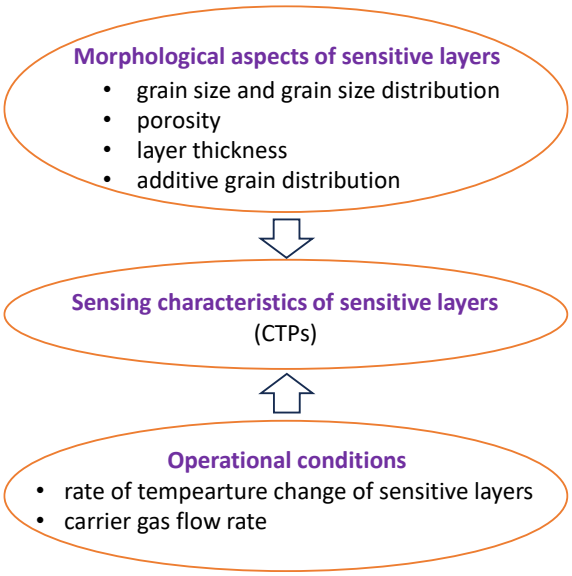

Fig. 1: Schematic illustration of the scope of investigation.

In the second part of the thesis, the same sensor arrays are applied for demonstration of a new, quasi-online analysis method of VFAs dissolved in a real biogas fermentation process. For this purpose, the fermentation sample is prepared in the lab using a biological substrate from a sewage plant and fed with dried beer marc and wood juice [12, 64]. Since MOG are well known to show cross-sensitivity to most biogas components (CH_4, CO, H_2) a pre-treatment routine of the fermentation sample had to be introduced before CTPs of different SnO_2/additive layers could be expected to represent VFAs. These experiments are done in context with in-situ CTP-measurements on fermentation sample with additional, manually dosed VFAs for studies of the CTP-shape changes with VFA-concentration. With these experiments, together with the different aspects as mentioned above in the first part of the study, the following aspects are discussed as well:

- method of fermentation sample pre-treatment,
- how the CTPs change with pH condition of the fermentation sample,
- how the CTPs change with changing VFA-concentration and VFA-type,
- similarity of the CTPs measured in fermentation sample with those measure with model VFAs dissolved in DI water.

The VFA concentration as developed in the fermentation process and further simulated by manual addition of well-defined volumes of the acetic and propionic acid are referenced by gas chromatography (GC) and are correlated with the corresponding changes of the CTPs.

2. BASIC THEORY

2.1. SnO_2 based semiconductor gas sensors

2.1.1. Bulk properties of SnO_2

SnO_2 is a wide-band gap n-type semiconductor [65] with a band gap of 3.6 eV [28]. It shows high chemical and mechanical stability [66]. Crystallographically, it grows in the rutile structure [67], in which each tin atom is surrounded by six oxygen atoms in an octahedral coordination and each oxygen atom is surrounded by three tin atoms in a planar coordination. Fig. 2 shows the rutile structure of tin oxide where green balls represent tin atoms and red balls represent the oxygen atom.

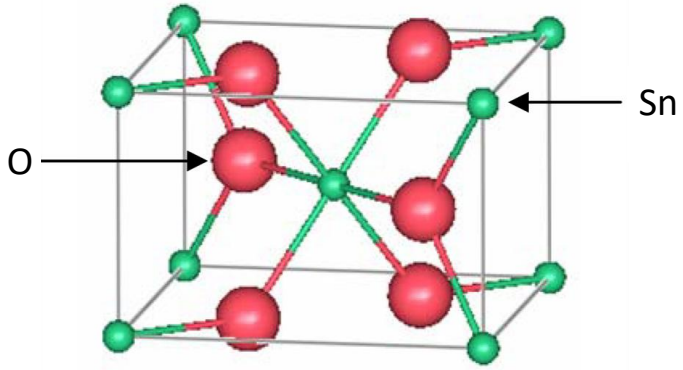

Fig. 2: Rutile tin oxide crystal structure. Adapted from [68].

The n type semiconductor property of SnO_2 is a consequence of volume oxygen defects. The oxygen vacancies, $V_{\ddot{O}}$, are known to be the dominant defects [69]. At higher temperature (T> approx. 500°C), the defect structure is in thermodynamic equilibrium with environmental oxygen partial pressure, $p(O_2)$. This oxygen exchange equilibrium of the non-stoichiometric tin oxide can be expressed using the Kröger-Vink notation as shown in eqs. (1)-(3) [70]:

$$O_O^x + 2Sn_{Sn}^x \Leftrightarrow {}^1/_2\, O_2 + V_{\ddot{O}} + 2\dot{Sn}_{Sn} \quad (1)$$

$$2\dot{Sn}_{Sn} \Leftrightarrow 2e + 2Sn_{Sn}^x \quad (2)$$

$$O_O^x \Leftrightarrow {}^1/_2\, O_2 + V_{\ddot{O}} + 2e \quad (3)$$

Where, a prime (') denotes one negative charge with respect to the lattice, a dot (·) denotes a positive charge and x denotes neutrality. Subscripts denote the atom which would normally occupy the site, V represents a vacancy and e denotes a conduction electron.

Thus, the electrical conductivity, σ, depends on oxygen partial pressure, $p(O_2)$, according to eq. (4) [69, 71].

$$\sigma \propto \left(p(O_2)\right)^{-1/m} \tag{4}$$

where, m = 6, and corresponds to a doubly ionized oxygen vacancy

2.1.2. Gas adsorption on the surface and band bending

From the view of thermodynamics, gas adsorption on a solid surface is a spontaneous process. This means, the change of the Gibbs free reaction energy, ΔrG, is negative (eq. (5)). Further, transition from the free gas to the adsorbed gas reduces the translational freedom of the adsorbate. Thus, the change in the entropy, ΔrS, is negative as well. Considering the thermodynamic relationship (eq. (5)), the reaction enthalpy of adsorption, ΔrH, must be negative as well. Thus, adsorption of gases on solid is an exothermic process. Therefore, in general, the extent of the gas adsorption under equilibrium conditions increases with decreasing temperature.

$$\Delta rG = \Delta rH - T\Delta rS \; < 0 \tag{5}$$

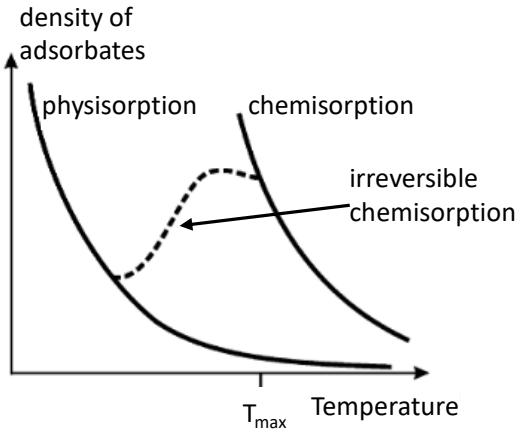

Fig. 3: Physisorption and chemisorption isobar as a function of temperature. A maximum coverage of chemisorbed molecules is at temperature Tmax. Adapted from [75].

Depending on the nature of the interaction and the forces involved, molecules can adsorb on the surface in two different ways and are distinguished as physisorption and chemisorption. As the gas molecule approaches a surface, gas molecule physically adsorbs (physisorption) on the surface and the interaction between the adsorbate and the substrate is caused by the van der Waals interaction which have a long range but are very weak. Physisorption takes place predominantly at low temperature and decreases with increasing temperature (Fig. 3). Since no activation energy is involved, the equilibrium condition is attained rapidly, and the process is readily reversible. The enthalpy of the physisorption is in the range of 20 kJ mol^{-1}.

As the physically adsorbed gas molecule comes closer to the surface, due to the charge transfer between adsorbate and adsorbent, a strong chemical bond between adsorbent and adsorbate is formed, which is called chemisorption, and is not readily reversible. The enthalpy of chemisorption is much bigger than that of physisorption and is in the range of 200 kJ mol^{-1}. Chemisorption may result in the dissociation of the adsorbate.

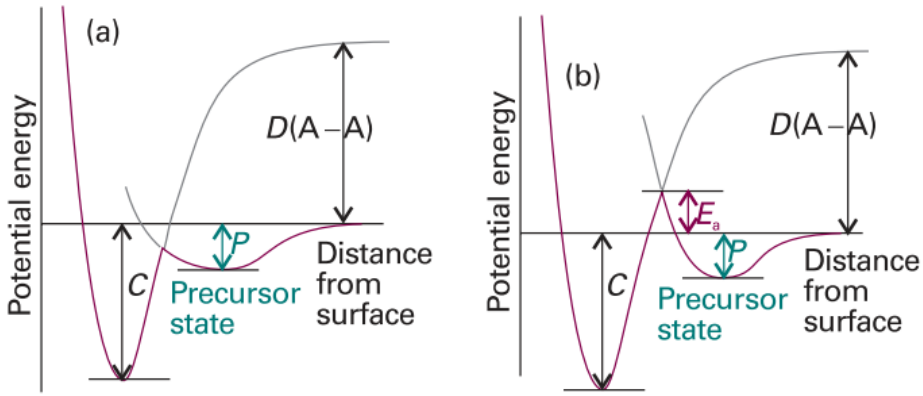

Fig. 4: Schematic potential energy curves for the (a) non activated and (b) activated dissociative chemisorption of an A_2 molecules. P: enthalpy of physisorption, C: enthalpy of chemisorption. In case of activated dissociative chemisorption, an energy of E_a must be overcome by the physisorbed molecule (precursor state) to reach the chemisorption well. Adapted from [72].

Fig. 4 shows the interaction of a diatomic gas molecule A_2 approaching on the surface D in the potential energy curve. As the gas molecule approaches the surface it becomes physisorbed on the surface as precursor state for chemisorption. There is a potential energy barrier separating the precursor and chemisorbed state. Depending on the barrier height, chemisorption can be activated (Fig. 4b) or not activated (Fig. 4a). Therefore, chemisorption can be fast if the activation energy is small, but it may be slow if the activation energy is large. Since,

chemisorption is an activated process, chemisorption increases with increasing temperature and there is a maximum coverage of chemisorbed molecules at temperature, Tmax (Fig. 3b).

As SnO_2 is an n-type semiconductor due to its non-stoichiometry, species like oxygen adsorbed easily on the tin oxide surface and tend to trap one or two electrons forming $O^-_{2\,ads}$, O^-_{ads}, and O^{2-}_{ads} depending on temperature [73], as illustrated in eqs. (6)-(9) [74].

$$O_{2\,gas} \rightarrow O_{2\,ads} \quad (6)$$

$$O_{2\,ads} + e^- \rightarrow O^-_{2\,ads} \ (T<150°C) \quad (7)$$

$$O^-_{2\,ads} + e^- \rightarrow 2O^-_{ads} \ (200°C < T < 400°C) \quad (8)$$

$$O^-_{ads} + e^- \rightarrow O^{2-}_{ads} \ (T>400°C) \quad (9)$$

The presence of different oxygen species ($O^-_{2\,ads}$, O^-_{ads}, and O^{2-}_{ads}) on the surface of tin oxide has been verified by IR (infrared), TPD (temperature programmed desorption), and EPR (electron paramagnetic resonance) analysis which are summarized in Fig. 5. At lower temperature (T <150°C, eqs. (6) and (7)), oxygen does not dissociate and adsorbs in a molecular form as either neutral $O_{2\,ads}$ or charged $O^-_{2\,\mathrm{ads}}$. At temperatures higher than 200°C, oxygen dissociates and adsorbs as O^-_{ads} ions (eq. (8)). In addition to O^-_{ads} ions, adsorbed O^{2-}_{ads} ions can also be formed at temperature above 400°C (eq.(9)).

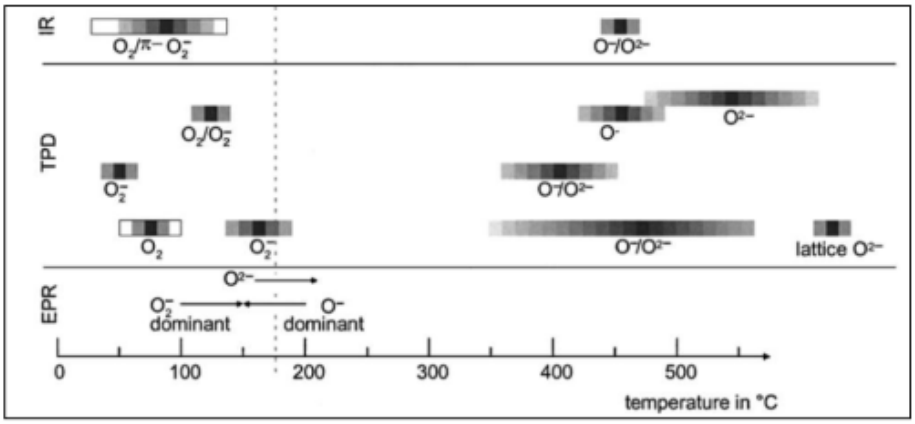

Fig. 5: Different adsorbed oxygen species on SnO_2 surfaces at different temperatures as verified by EPR, TPD and IR analysis. Adapted from [74].

The captured electrons trapped at the grain surface originate from the intrinsic oxygen vacancies and are extracted from the conduction band, E_c (Fig. 6). As the numerous oxygen adsorption

events occur solely on the surface of the SnO_2-grain, negative surface charge is generated. The presence of negative surface charge leads to the formation of an electron depleted region resulting in the band bending and produces a surface potential barrier, eV_s (Fig. 6). The width of the depletion layer, which is also called as Debye length, L_D, mainly depends on the temperature and the density of electron states of the bulk as given by eq. (10)[65]. In this depletion layer, the density of mobile electrons i.e. the electronic conductance is massively reduced and depends on the density of the charged oxygen surface states.

$$L_D = \sqrt{\frac{\varepsilon_r \varepsilon_0 \, k_B T}{e^2 \, N_s}} \tag{10}$$

where ε_r is relative permittivity of MO, ε_0 the absolute permittivity, k_B the Boltzmann constant, T the absolute temperature, e the electron charge, and N_s the charge carrier concentration.

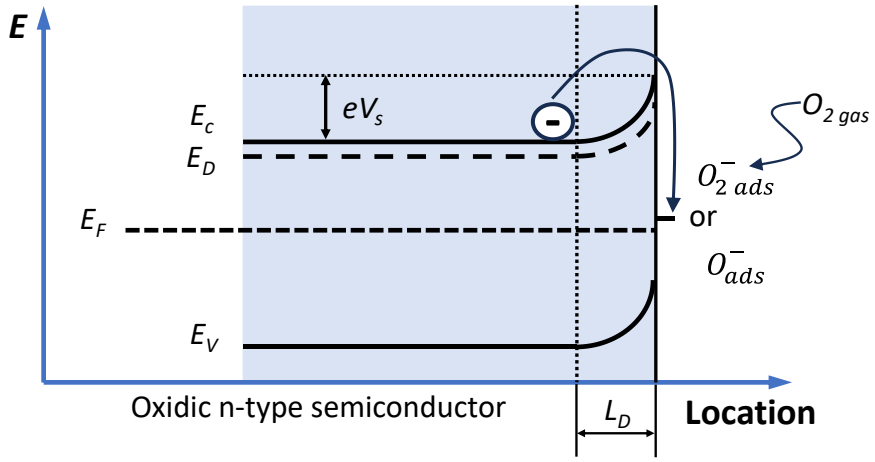

Fig. 6: Oxygen adsorption and band bending process on an n-type MO semiconductor. E_c is the lower edge of the conduction band; E_V is the upper edge of the valence band; E_D is the donor level of the semiconductor; and E_F is the fermi level.

In the case of porous, polycrystalline SnO_2 layers, the electrical conductance occurs by grain-to-grain contacts of adjacent particles (Fig. 7). The electrons travelling between adjacent grains must overcome the potential barrier formed by surface charging. This is called as Schottky barrier formed at the grain boundaries and the barrier height, eV_s, increases with the increase of the concentration of adsorbed oxygen states ($O^-_{2\,ads}$, O^-_{ads}, O^{2-}_{ads}) [76]. In accordance with this well accepted model, the conductance of a SnO_2 layer, G, can be expressed by eq. (11) [65].

$$G \approx exp\left(\frac{-eV_s}{k_B T}\right) \tag{11}$$

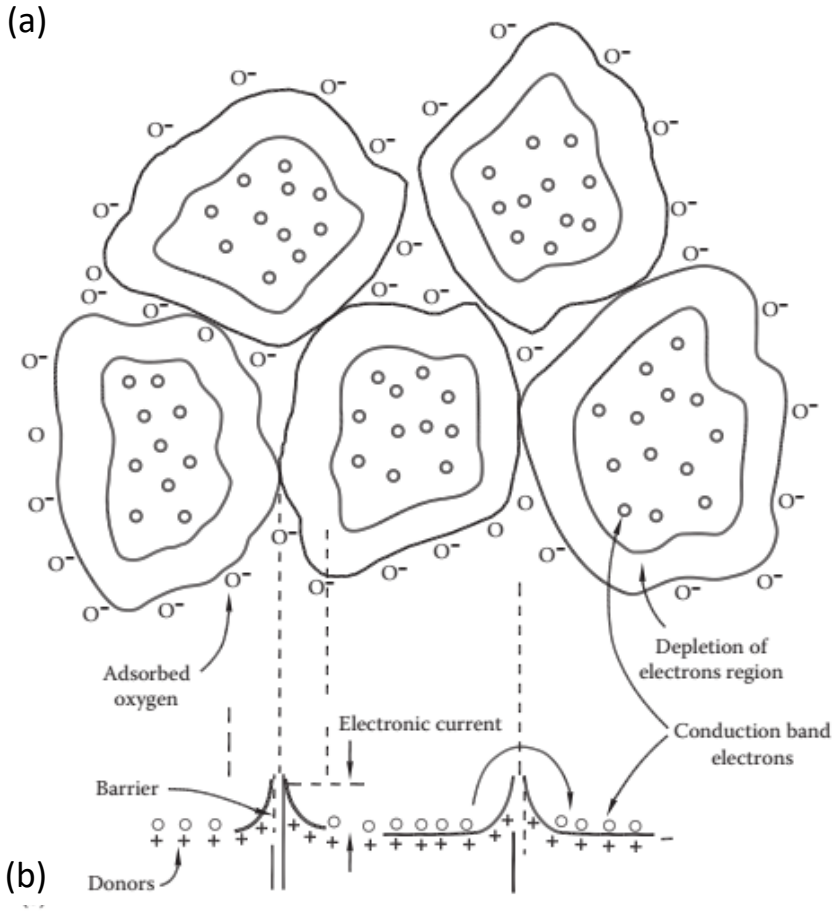

Fig. 7: Schematic representation of (a) oxygen species interaction with grains in the bulk, and (b) the corresponding energy band model. Adapted from [76].

2.2. Processes at solid surfaces

2.2.1. Adsorption isotherm

For gas detection, only those reactions that affect the surface coverage of the adsorbed oxygen states ($O_{2\,ads}^{-}$, O_{ads}^{-}, O_{ads}^{2-}) on the SnO_2 surface are crucial. The extent of surface coverage is expressed as a fractional coverage, θ, according to eq. (12) and the change of fractional coverage with time i.e. $\frac{d\theta}{dt}$ determines the rate of surface coverage or rate of adsorption.

$$\theta = \frac{Number\ of\ adsorption\ sites\ occupied}{Number\ of\ adsorption\ sites\ available} \tag{12}$$

For all the gas species involved in the surface reaction, there is a dynamic equilibrium between the adsorbed (e.g. $O_{2\,ads}$) and gaseous state (e.g. O_2). In general, the fractional coverage of the gas species *A* on the surface, θ_A, depends on its partial pressure, p_A, (Fig. 8) at a chosen temperature and can be described, for e.g. in the simplest model of Langmuir isotherm [77] according to eq. (13). However, it should be noted that Langmuir's models are based on the following assumptions.

- The surface is perfectly uniform.
- All the adsorption sites are equivalent,
- Adsorption of adsorbate occurs as monolayer on the surface.
- Ability of adsorbate to bind on the adsorption site is independent of whether the neighboring site is occupied or not i.e. there is negligible interactions between the adsorbed species.

$$\theta_A = \frac{K_A \cdot p_A}{1 + K_A \cdot p_A} \tag{13}$$

The fractional coverage is linearly dependent to the partial pressure, p_A, in the range $K_A.p_A << 1$ and tends to reach the maximum coverage at $K_A.p_A >> 1$ (Fig. 8). The gas-specific equilibrium constant, K_A, describes the ratio of adsorption rate, k_{ads} and desorption rate, k_{des} and in general, depends on the temperature, adsorption enthalpy, ΔE_{ads}, and desorption enthalpy, ΔE_{des} according to eq.(14).

$$K_A = \frac{k_{ads}}{k_{des}} = k_0 \cdot exp\left(\frac{-(\Delta E_{ads} - \Delta E_{des})}{kT}\right) \quad (14)$$

Where k_0 is the pre-exponential factor.

The dependency of θ_A on temperature can be expressed through gas-specific equilibrium constant, K_A. As the temperature increases, K_A reduces which means the θ_A reduces.

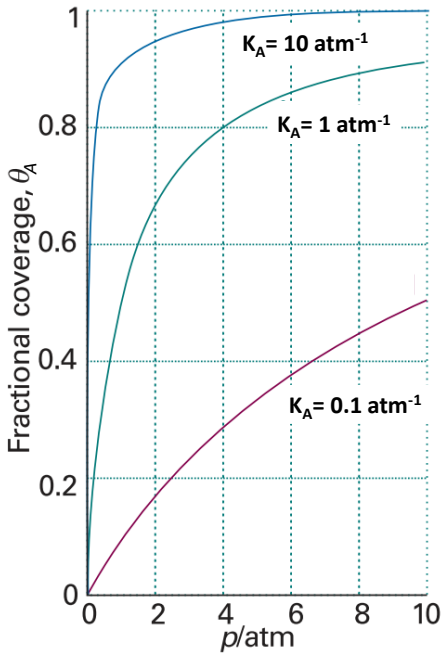

Fig. 8: Fractional coverage, θ_A, of gas species A on the solid surface over its partial pressure. Adapted from [72].

Before discussing the general gas sensing mechanism (Sec. 2.3) of SnO_2-layers, it is necessary to first introduce different relevant surface reaction mechanisms which are discussed in Sec. 2.2.2. These surface reaction processes are significantly influenced by heterogenous catalytic effects of MO. The basics of heterogeneous catalysis is shortly introduced in Sec. 2.2.3.

2.2.2. Chemical reaction at solid surfaces

The chemical reaction on solid surfaces under isothermal conditions is generally described in different sub steps consisting of adsorption, diffusion reaction and desorption. A distinction is made between different reaction mechanisms.

i. Langmuir-Hinshelwood mechanism

In this reaction mechanism (Fig. 9a), both reactant molecules (A and B) must be adsorbed on the surface before reaction is possible. The surface facilitates diffusion of the molecules and reaction forming the product C. The product C desorbs, and the surface can be reoccupied. The reaction rate for LH-mechanism is given by eq.(15).

$$r_{LH} = k_{diff} \cdot \theta_A \cdot \theta_B \tag{15}$$

For example, if A and B both follow the Langmuir isotherm (eq. (13)), the reaction rate is given by eq.(16).

$$r_{LH} = \frac{k_{diff} \cdot K_A \cdot K_B \cdot p_A \cdot p_B}{(K_A \cdot p_A + 1)(K_B \cdot p_B + 1)} \tag{16}$$

The parameters K_A and K_B as well as the rate constant k_{diff} are all temperature dependent. The reaction rate is maximum when $K_A \cdot p_A = K_B \cdot p_B$ and $\theta_A = \theta_B = 0.5$.

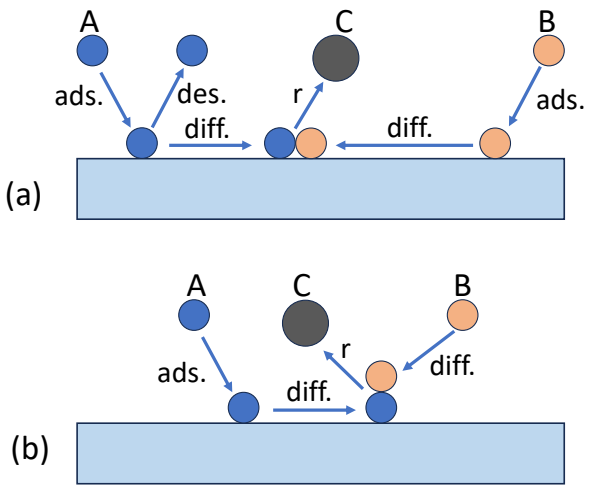

Fig. 9: Surface reaction according to (a) LH and (b) ER mechanism.

ii. Eley-Rideal mechanism

In Eley-Rideal (ER) reaction mechanism (Fig. 9b), a gas phase molecule (component B) reacts with another molecule already adsorbed on the surface (component A) forming the product C, subsequently followed by the desorption of the product. The effective reaction rate is proportional to the fractional coverage of A, θ_A, and partial pressure of B, p_B, according to eq.(17). In contrast to LH, ER mechanism does not have a maximum reaction rate.

$$r_{ER} = k_{diff} \cdot \theta_A \cdot p_B \tag{17}$$

For example, if A follows the Langmuir isotherm (eq. (13)), the reaction rate is given by eq.(18).

$$r_{ER} = \frac{k_{diff} \cdot K_A \cdot p_A \cdot p_B}{(K_A \cdot p_A + 1)} \tag{18}$$

iii. Mars van Krevelen mechanism

Mars van Krevelen (MvK) mechanism is used for modelling catalytic oxidation reaction of hydrocarbons on transition MO catalyst surface [78] based on the following assumptions.

- All the reaction sites are equivalent i.e. available lattice oxygen ions are equivalent.
- There is no interaction between occupied and vacant lattice site.
- Reduction and oxidation of the MO are the rate determining steps.

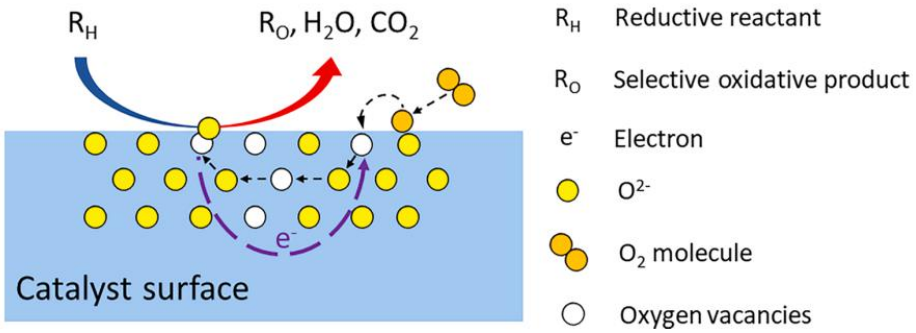

Fig. 10: MvK mechanism reaction scheme. Adapted from [79].

In MvK mechanism, the surface itself take part in the reaction (Fig. 10) and the reaction steps are as following [79]:

a) The reductive hydrocarbon reactant, R_H, can adsorb on the oxide surface and be oxidized by the lattice oxygen, O^{2-}, to form selective oxidation product, R_O, or complete oxidation products H_2O and CO_2.

b) Reoxidation of the reduced MO or replenishment of oxygen vacancy sites by the surface adsorption and dissociation of ambient oxygen molecule, O_2, followed by the lattice O^{2-} diffusion.

c) Reduction and reoxidation of the MO are the rate determining steps of the reaction.

2.2.3. Aspect of heterogenous catalysis

The gas reaction processes at SnO_2-surfaces are well known to be influenced by its catalytic properties [80, 81]. In general, a catalyst is a substance that increases the rate at which a chemical reaction approaches equilibrium, without itself becoming permanently affected by the reaction. The catalyst enhances the rate of product formation by providing a reaction path with a lower activation energy, E_a, than the uncatalysed mechanism (Fig. 11).

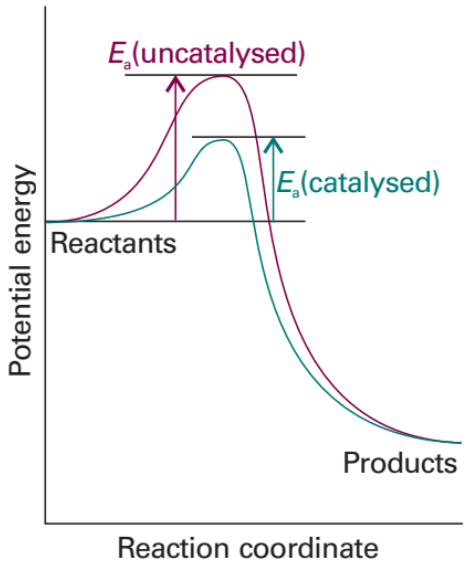

Fig. 11: Reaction path of uncatalysed and catalysed reactions. Adapted from [72].

Heterogenous catalysts are phase distinct from the reactants and products. In case of SnO_2, its catalytic properties (specifically reactive surface molecular orbitals) take individual influence on different surface processes, such as adsorption/desorption processes (Sec. 2.2.1) as well as on the surface reaction of combustible gases with adsorbed oxygen species ($O_{2\,ads}^-$, O_{ads}^-, O_{ads}^{2-}),

as modelled by different reaction mechanisms, such as LH or ER mechanism as discussed in Sec. 2.2.2.

As different crystallographic planes of SnO_2, such as (110), (111), (200), (011), (112), and (210) possess different catalytic properties [67], the rate of surface processes may differ from one crystal orientation to another. As a consequence, different crystallographic planes of SnO_2 show individual sensitivity to different target gases as reported in different studies [82, 83] and, therefore, different sensing properties from differently prepared SnO_2 morphologies can be expected.

Moreover, the catalytic properties of porous SnO_2 as well as their surface processes can be influenced by the addition of catalytically active nanoparticles forming a two-phase porous composite [76, 84–86]. This means, by choice of the additive, the reactivity of the surface to specific gas components can be influenced. The mechanisms how the additives can affect the intergranular contact region of the SnO_2 grains and consequently influence the gas sensing is discussed in more detail in Sec. 2.3.2.

2.3. Gas sensing Mechanism

Oxidizable (combustible) gas molecules can react with the adsorbed, highly reactive and charged oxygen species ($O^-_{2\,ads}$, O^-_{ads}, O^{2-}_{ads}) but with individual grade of oxidation reaction and consequently release the formerly captured electron back to the conduction band. This means, after reaction with oxidizable gases, freed electrons are now mobile and contribute to the electron concentration, N_s, in the conduction band. This reduces the L_D and the barrier height, eV_s (Fig. 12), and consequently results in the increase of the conductance, G (eq. (11)), before the freed electrons are localized again by following surface oxygen adsorption processes (conductance decrease).

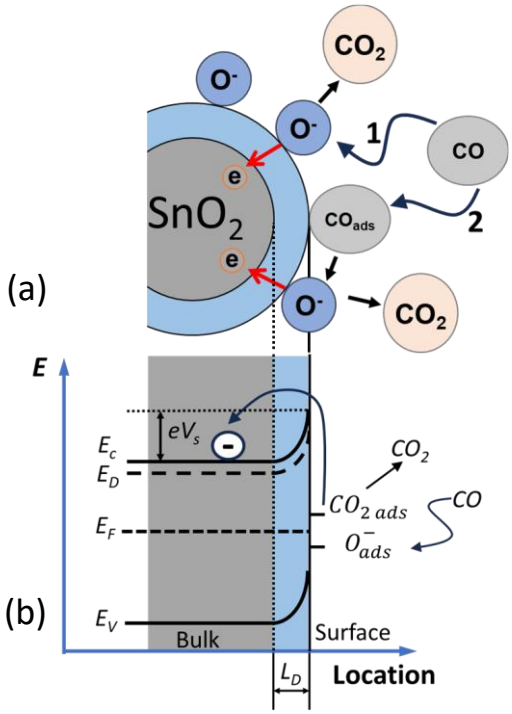

Fig. 12: Different mechanism of surface reaction of CO with chemisorbed oxygen. (a) ER mechanism (Path 1) and LH mechanism (Path 2). Grey: SnO_2 bulk region, blue: SnO_2 electron depletion layer. (b) In both cases, the localised electron is released back to the conduction band.

This process is exemplarily shown in a simplified form using the model reaction of CO according to eq. (19) and is fundamentally similar for other oxidizable gases.

$$CO(g) + O^-_{ads} \rightarrow CO_2(g) + e^- \qquad (19)$$

The oxidation reaction of oxidizable gas can take place either directly from the gas phase i.e. via ER mechanism (Fig. 12a, path 1) or be preceded by an adsorption or diffusion process via LH mechanism (Fig. 12a, path 2) , as introduced in Sec. 2.2.2.

This general model of surface reactions with adsorbed oxygen states was already introduced more than three decades ago for e.g. by McAleer et al. [70]. In fact, the individual surface processes of the charged oxygen states with gas molecules as just introduced above are highly influenced by heterogeneous catalysis effects (Sec. 2.2.3) and the expansion of the surface reaction model in case of the presence of additives is illustrated in more detail in Sec. 2.3.2 (Fig. 17).

Another important factor influencing the conductance of the tin oxide is the humidity. Water molecules can be adsorbed by physisorption or hydrogen bonding [74]. At temperatures above 200°C, molecular water is no more present on the surface but exists in the form of hydroxyl groups [74] by molecular dissociation of water, which act as an electron donor [71, 87]. This causes direct increase of the conductance (eq.(20)).

$$H_2O + O^-_{ads} \rightarrow 2OH_{ads} + e^- \qquad (20)$$

2.3.1. Influence of layer morphology and grain size

The gas sensing reaction itself can occur at different reaction sites of the SnO_2 depending on the layer morphology and simple distinction in layers can be made between compact layers and porous layers [88, 89]. In the compact layers, the gas interaction takes place only at the geometrical surface and the bulk is not accessible to gases. However, in the porous layers, the gas can penetrate into the entire layer and even the volume of the sensing layer is accessible to the gases [88, 89]. In this case, the active surface is much higher than the geometric surface (Fig. 13).

For the compact layers, there are at least two possibilities: completely or partly depleted layers, depending on the ratio between the layer thickness and Debye length, L_D. In case of partly depleted layers, surface reactions do not influence the conduction in the entire layer and the (major) conduction process takes place through the bulk region. Thus, the relative conductance change is very low resulting in limited sensitivity [88, 89].

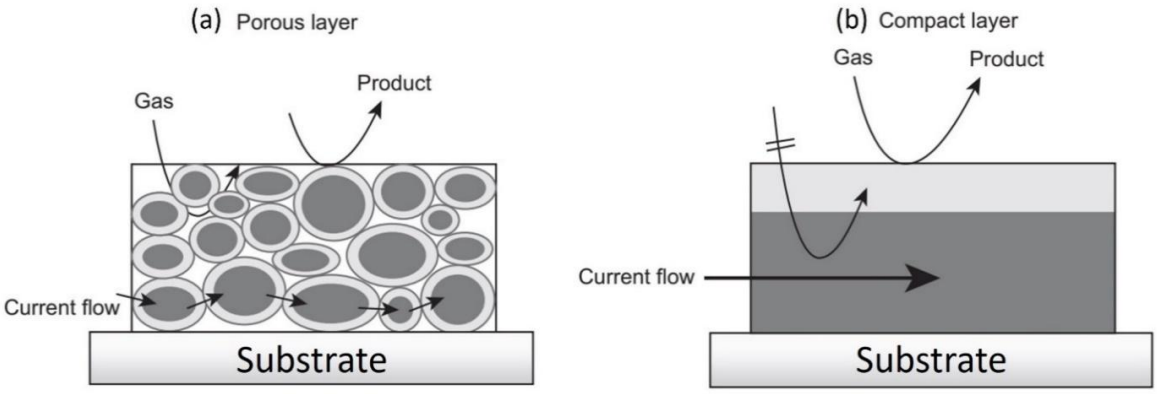

Fig. 13: Schematic layout illustrating difference between (a) porous layer and (b) compact layer. Adapted from [88].

For the porous layers, the presence of necks between the grains makes the overall situation much more complicated. The interconnected grains may form larger aggregates as well. In a simple model, three different cases can be distinguished according to the relationship between the grain diameter, D, and the Debye length, L_D, [67, 90] as shown in Fig. 14.

For the grain size $D >> 2L_D$ (Fig. 14a), the conductance of the film is limited by Schottky barriers at the grain boundaries and the gas sensing mechanism is controlled by grain boundaries [90]. In this case, the sensitivity is practically independent of D.

As grain size decreases, depletion region extends deeper into the grain and when the grain size is comparable to $2L_D$ (i.e. $D \geq 2L_D$) (Fig. 14b), every conducting channel forming the neck between grains becomes big enough (in relation to the grain size) to influence the bulk conductance, and therefore the sensitivity is enhanced with respect to the former case (Fig. 14a) [90]. Furthermore, the sensitivity to gases becomes more grain size dependent.

When $D < 2L_D$ (Fig. 14c), the depletion region extends throughout the whole grain and the grains are fully depleted [90]. As a result, there is sharp reduction of bulk conductance since the conduction channels between the grains are now vanished and conductivity is essentially grain controlled. Various studies have confirmed that the sensitivity is dramatically increased with the grain size smaller than double the Debye length [74, 86, 91]. This grain size of maximum sensitivity is in the range of several nanometers [86]. On the other hand, those porous nanomaterials were speculated to be quite unstable under conditions of high operation temperature due to their high surface energy, which promotes post-sintering effects [92].

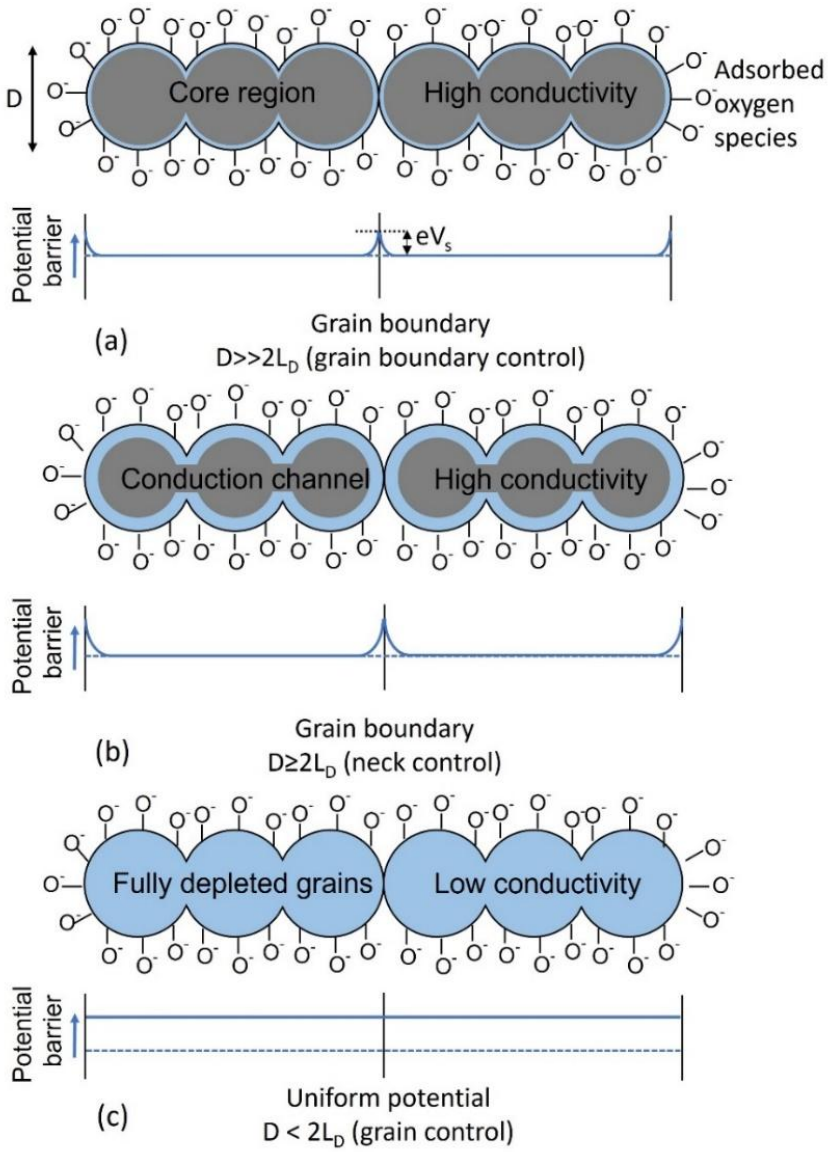

Fig. 14: Schematic model of the effect of the grain size on the sensitivity of the n-type MOG: (a) $D>>2L_D$ (grain boundary controlled), (b) $D \geq 2L_D$ (neck controlled), and (c) $D < 2L_D$ (grain controlled).

In addition to the particle size and porosity, the influence of the film thickness should be considered as well. Maximum sensitivity is achievable when all percolation paths and active surfaces contribute to the gas sensing without diffusion limitation. However, as the analyte gas is diffusing through the porous layer, a concentration gradient is formed [67, 89], which depends on the diffusion rate of the analyte and the rate of reaction of the analyte with adsorbed oxygen. Additionally, catalytic effects associated with admixed additives (Sec. 2.3.2) as well as with electrode and possible reaction at the electrode/MO interface [41] has to be considered.

Contributions to the overall impedance of the porous gas sensitive layer from electrode/MO-interface, intergranular contacts, bulk, and surface are schematically illustrated in Fig. 15 together with their R-C equivalent circuits. The grain boundary can be represented by a resistor and a capacitor in parallel. The resistor represents the highly resistive depletion layers at the intergranular contacts and the capacitor is formed in parallel due to the sandwiching of highly resistive depletion layers between two highly conductive bulk areas of interconnected grains. The interface between MO and the metal electrode forms a Schottky contact and is represented by a resistor and a capacitor in parallel [41]. For the partly depleted grains, when surface reaction do not influence the conduction of whole grain (e.g. Fig. 14a and Fig. 14b), the bulk and surface of the grain is represented by two resistors (one for each) and a capacitor in parallel (Fig. 15). Only resistor representing surface is influenced by the surface reaction.

As a consequence of the above discussion, the thinner layer is expected to assure better sensitivity and faster response but less conductivity. Correspondingly, there are some constrains to be considered related to measurability of the layers as well as to technical difficulties and limitations associated with layer deposition techniques (both thin and thick film technologies) for lowering the film thickness beyond certain value with acceptable layer-homogeneity.[67].

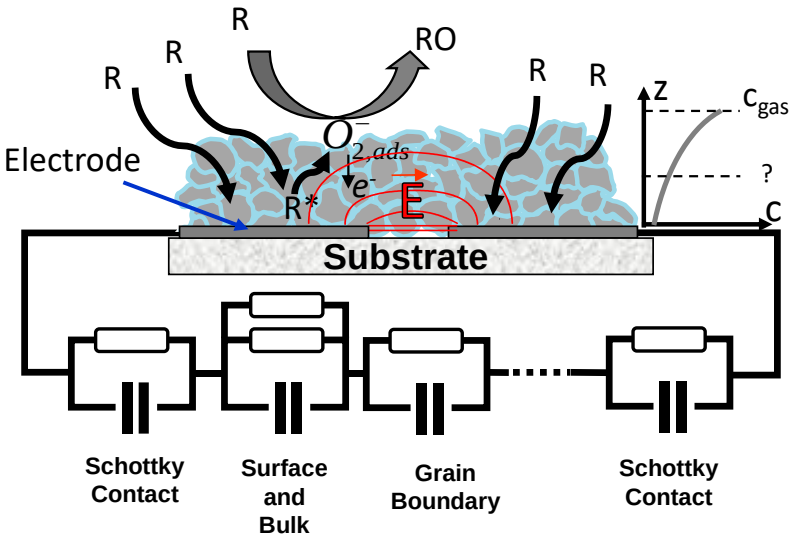

Fig. 15: Schematic overview over the possible processes proceeding in porous gas sensitive layers indicating different contributions from surface, bulk, electrodes as well as from grain boundaries and the gas concentration gradient formed over the layer thickness. R: analyte gas, RO: reaction product, R*: active radical. Different contributions to the overall impedance are represented by an equivalent circuit with R-C units. E is the electric field induced between two electrodes during impedance measurement Adapted from [41].

2.3.2. Influence of additives on gas sensing properties

As introduced by Morrison [76], the gas specific surface reactions can be influenced by means of catalytically active nanoparticles used as additives, which takes influence on the gas reaction and on the surface electron transfer process as well [41, 84, 85, 93, 94]. The influence of nanoscaled platinum, silver or palladium additives distributed finely on SnO_2-grains (Fig. 16) on the sensing behaviour at exposure to various gas components in the temperature range of approx. 200-500°C has been already investigated by Yamazoe [94] in 1983. Two types of interaction (Fig. 17) between the additives and MO were described, the chemical interaction and electronic interaction [94].

In the chemical interaction (Fig. 17a) additives assist the redox process of MO. At appropriate temperatures, reactant first adsorbs on the surface of the additive, dissociates, and then migrates to the MO surface by a so-called spill-over effect (Fig. 17a) to react with the adsorbed oxygen species resulting in an increase in surface conductivity of MO.

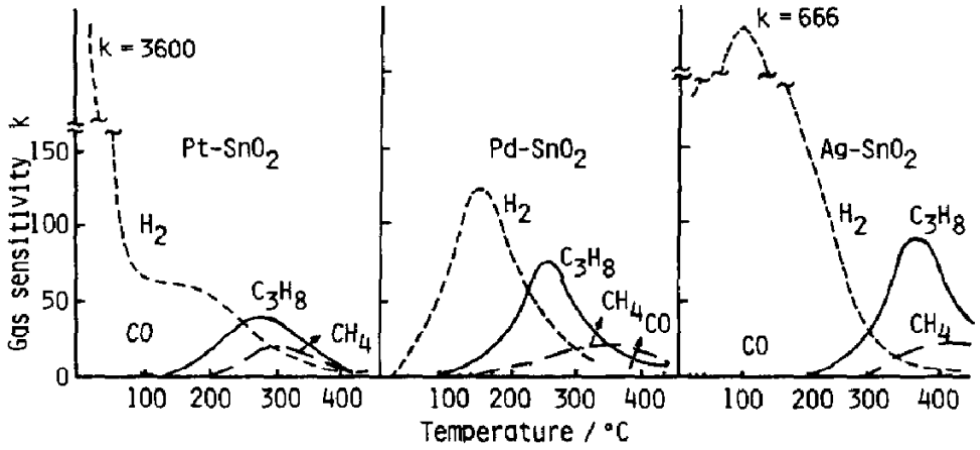

Fig. 16: Relative sensor response (G/Go) of SnO_2/additive-layers (additives: 0.5 wt. % Pt, Pd and Ag) on exposure to 8000 ppm H_2, 5000 ppm CH_4, 2000 ppm C_3H_8, and 20 ppm CO. Adapted from [94].

The second type of interaction is an electronic (Fig. 17b) one in which the additive interacts electronically with the MO as an electron donor or acceptor. In such an electronic interaction, when the oxidation state of the additive changes with the surrounding gas condition, the electronic state of the semiconductor changes accordingly. This type of additives, for e.g. Ag and Pd, is known to form stable oxides in air, while it is easily reduced to its metal form in presence of reducing gases releasing electrons back to the semiconductor [65].

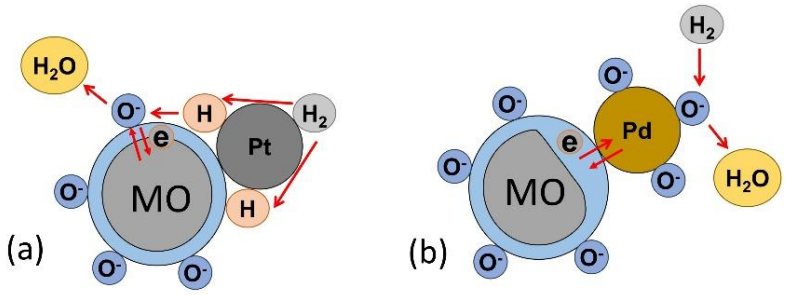

Fig. 17: (a) Chemical, and (b) electronic sensitization mechanism in the noble metal additives admixed MO sensors.

However, to have desired influence on the conductance/sensitivity, good dispersion of the additives is important so that additives are located near all intergranular contacts. Only then can the additives affect the intergranular contact resistance. For instance, Fig. 18a schematically shows the effect of poor dispersion and similarly, a well dispersed additive situation in Fig. 18b. In the latter case, the depleted regions at the surface of the MO overlap and the influence of the additive extends to the whole inter granular percolation contacts [76].

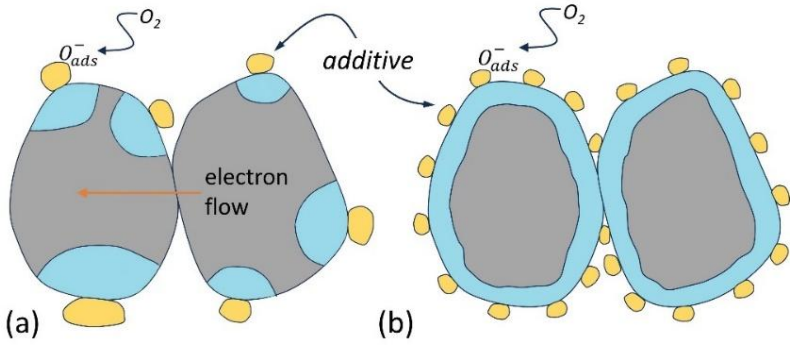

Fig. 18: Effect of (a) poor additive dispersion, and (b) adequate additive dispersion.

2.3.3. Mode of sensor operation

i. Isothermal operation

As discussed in Sec. 2.1.2, the conductance change of the SnO_2-layers is based on gas surface reactions which could be roughly described by the combination of different processes like surface adsorption of the gas molecules, surface chemical reactions with already adsorbed oxygen states followed by the electron delocalization and desorption of the reaction products. The gas adsorption equilibria and the rates of all these surface processes depend specifically on the reaction process with the individual target molecule, which in turn is catalytically influenced

by the presence of additives and are all specifically and most strongly dependent on the temperature (see Sec. 2.1).

Thus, isothermally operated MOG simultaneously show various but individual gas-specific sensitivities to different gas components due to their general interaction with all oxidizable or reducible gas components. This means, at isothermal operation, in the very most cases, these individual sensitivities are not strong enough to enable discrimination of competing reactions with other gas components (cross-sensitivity). The dependency of the conductance G on the gas concentration c can be expressed by a power law equation as expressed by eq. (21) [95, 96]. The pre-exponential factor, A, and the power law exponent, β, are primarily molecular specific constants [95] and are related to the individual surface reaction mechanism at a given temperature [97] as well as on the morphology of the sensing layer [98].

$$G = A \cdot c^{\beta} \tag{21}$$

Consequently, in case of isothermally operated MOG, the user is faced to the problem that there is never a clear criterion for gas component identification due to ambiguity of the measurement signal at different concentrations of the target gases i, j and k (Fig. 19). This is due to the lack of adequate correlation between conductance-change (sensitivity) and the gas component which generates this change. However, since different gases show a characteristic optimum surface reaction temperature [39] and correspondingly a characteristic sensitivity with temperature as demonstrated in Fig. 16, it is possible to make the sensor more sensitive to certain gas components by use of the most suitable operating temperature.

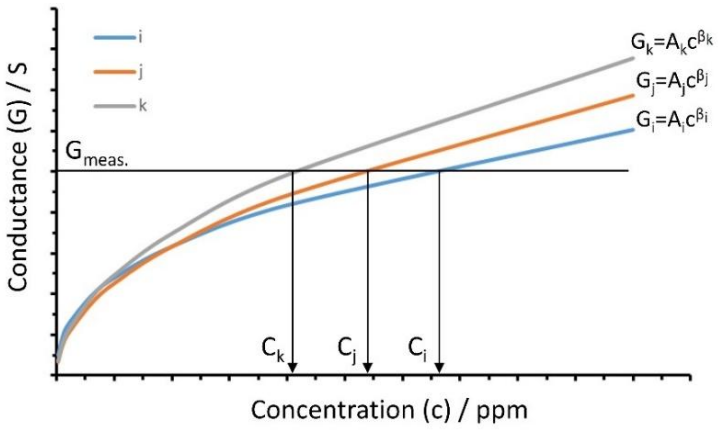

Fig. 19: Schematic dependence of conductance G on the gas components i, j and k. The measured conductance $G_{meas.}$ directs to three different concentrations of the possible gas components.

ii. Thermo-cyclic operation

Based on the previous discussion, better chemical analysis capability by use of MOG can be expected by periodic variation of the operation temperature of the gas sensitive layers to measure the layer conductance. The resulting Conductance over time Profile (CTP) represents the conductance features over one temperature cycle period, which are characteristically affected by the individual surface chemical reactions of the specific gas molecules. At this novel operation procedure, the different rates of temperature-dependent physico-chemical processes are exploited. This means, non-steady state reaction conditions must be considered. According to the Langmuir isotherm model (Sec. 2.2.1, eq. (13) and eq. (14)), the fractional coverage of the reaction sites by adsorbed oxygen states as well as by target gas molecules depends considerably on temperature of the gas sensitive layer and, of course, the reaction kinetics including the electron delocalization process (Fig. 6) also depends on the local temperature. according to the Arrhenius equation (eq. (22)) [72].

$$k = A \cdot e^{-E_a/RT} \tag{22}$$

Where k is the reaction rate constant of the reaction; A is the pre-exponential factor or frequency factor and is considered to be a temperature independent constant for each chemical; E_a is the activation energy of the reaction; R is the gas constant (8.314 J·mol^{-1}·K^{-1}) and T is the absolute temperature.

All these reaction processes are further affected by transport processes on top and inside the porous layer. Inside the pores Knudsen diffusion is assumed to happen, as the mean free path of diffusing gas molecules is assumed to be larger (about 70 nm at standard pressure) than the pore diameter. Again, the Knudsen diffusion coefficient, D_K, is influenced by the local temperature according to eq.(23) [99].

$$D_K = \frac{d_p}{3}\sqrt{\frac{8RT}{\pi M}} \tag{23}$$

Where, d_p is the pore diameter; R is the gas constant (8.314 J·mol^{-1}·K^{-1}); T is the absolute temperature and M is the molar mass of the gas molecule.

All these parameters directly relate to the electron delocalization processes and, therefore, to the electronic conductance of the surface near region (electron depletion layer) [70]. They are now scanned during thermo-cyclic variation of the temperature and therefore are variables of time.

The concept of dynamic sensor operation method is not new. In 1989, Sears et.al [100] already reported that the conductance over time signal measured during sinusoidal modulation of the heating voltage is molecular specific and represents the specific target molecule interaction with the individual gas sensitive material and adsorbed oxygen species ($O^-_{2\,ads}$, O^-_{ads}, O^{2-}_{ads}) vs. temperature. However, only if the rate of temperature variation of the sensor is slow enough compared to the kinetics of chemical response (this includes diffusion rates in the porous layer as well as adsorption/desorption and reaction rates; all depend on temperature), the target gas specific CTP represents a quasi-steady state chemical response [101]. Frank et al. [101] showed experimentally on self-prepared thick film tin oxide layers that the relaxation of the CTP-changes with time is not finished even at a cycle time of one hour. In general, the target gas specific chemical conductance response occurs due to different processes happening at the sensor surface: (1) type of adsorbed oxygen states ($O^-_{2\,ads}$, O^-_{ads}, O^{2-}_{ads}) [74] which varies over the temperature range. (2) individual activation temperature needed for reaction with the analyte, (3) temperature variation rate [100], (4) layer thickness, (5) grain size and morphology [65]. All these parameters define the reaction kinetics and diffusion rate of gas species at the surface and in the pores of the layer. In addition, (6) specific reactions at the electrode/MO interfaces [74, 102], and (7) specific reactions at the additive/MO interface [36] must be considered.

Various ways of temperature modulation of MOG have been investigated and could be distinguished as (1) continuous temperature modulation , for example, by use of sinusoidal [89, 100, 103–105] and triangular heating voltage [36, 41, 106, 107], and (2) discrete temperature modulation, for example, by use of heating voltage in the form of pulses [108–111], steps or stairs [22, 112], pseudo random [113], rectangular [114] and series of heating pulses with different pulse height [115]. All these temperature modulation methods have shown potential of both qualitative and quantitative gas analysis by extracting gas specific characteristic information from the measured conductance over time signals using various analysis techniques, such as Fast Fourier Transform (FFT) analysis [89, 104, 105, 116], artificial neural network [110], and linear discriminant analysis [112].

In this work, sensors are thermo-cyclically operated based on triangular temperature change over time (Fig. 20a) and simultaneously CTPs are measured (Fig. 20b and Fig. 20c), which are characteristic in shape for different target gases and their concentrations.

Correspondingly, numerical analysis of the resulting target gas-specific CTPs based on their shape and characteristic profile features allows not only the molecular identification, even of binary gas mixtures, by analysis of the profile shape but even a full analysis by quantitative determination of the gas component concentrations is possible [118, 119] but, as a prerequisite, needs a set of calibration data [36]. This aspect of chemical analysis, however, was not the focus of this work and must be further investigated in future.

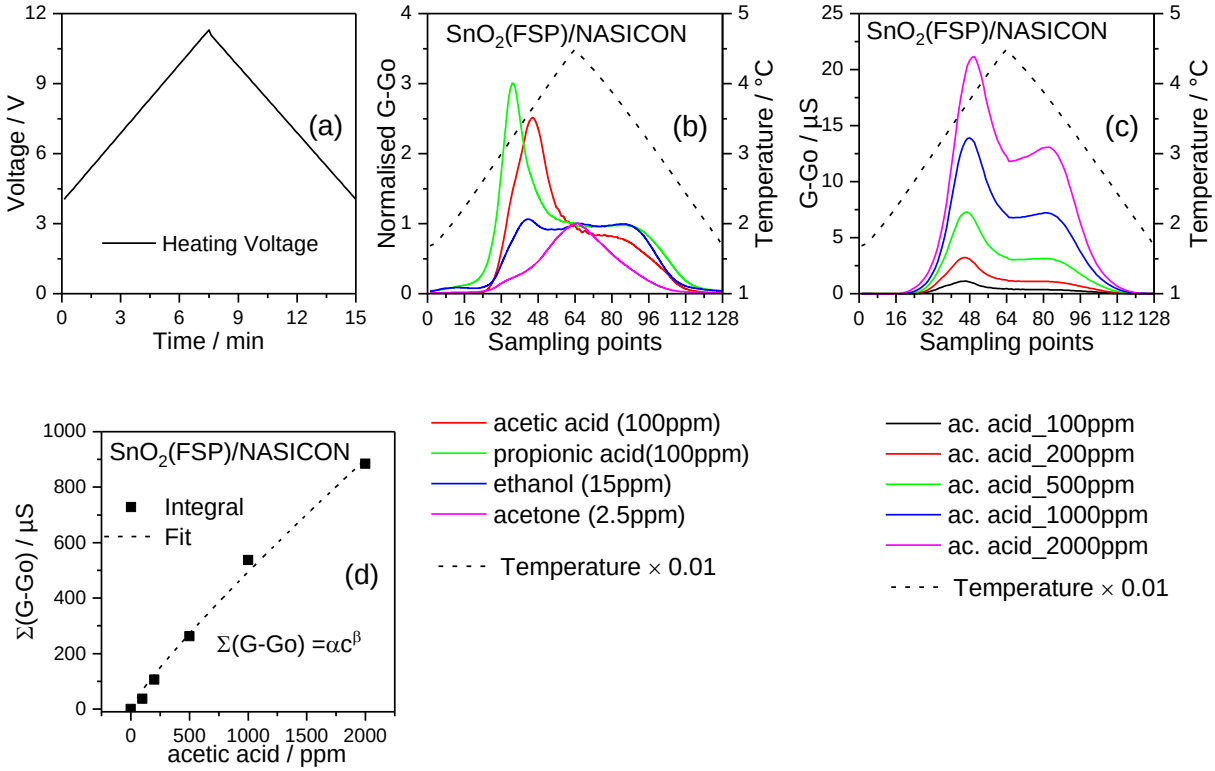

Fig. 20: Example of CTPs sampled by thermo-cyclically operated SnO_2(FSP)/NASICON-layer: (a) triangular heating voltage with cycle time of 15 min, (b) corresponding sensor temperature and normalised CTPs given as (G-Go) values measured for different VOCs. Normalisation is made by the (G-Go) value at the maximum temperature of temperature cycle. Go is the CTP measured for DI water at pH 7. G is the CTP response measured for VOC-analyte dissolved in DI water at pH 3 (c) CTPs for different concentrations of acetic acid. In every temperature cycle, CTPs were recorded with 128 sampling points. (d) CTP integrals vs. acetic acid concentration.

Moreover, the CTPs can be described as the absolute sensor response (R) i.e. the integral sum of the CTP of a cycle. The resulting integral (Fig. 20d) is a direct function of the gas concentration and the power law equation (eq.(21)) is still valid but now it has to be expressed as formulated in eq. (24) [63, 100, 101, 106], where $G_x(c)$ is the conductance at a certain sampling point x while gas exposure at concentration c, $Go_x(air)$ is the conductance at the same x, i.e. the same temperature and time but on exposure to air and n is the number of sampling points measured in a single temperature cycle.

$$R = \sum_{x=1}^{n} G_x(c) - Go_x(air) = \alpha \cdot c^{\beta} \tag{24}$$

Similar to eq. (21), the pre-exponential factor, α, and the power law exponent, β, are primarily molecular specific constants and, as discussed before, are related to the individual surface reaction mechanism as well as on the morphology of the sensing layer [98].

Similarly, the relative sensor response *S* of thermo-cyclically operated sensor could be defined according to eq. (25) [101].

$$S = \frac{1}{n}\sum_{x=1}^{n} \frac{G_x(c) - Go_x(air)}{Go_x(air)} \tag{25}$$

2.4. Methodology of dissolved VOCs analysis using MOG in combination with a carrier gas probe

The analysis of dissolved VOCs in aqueous liquids using thermos-cyclically operated MOG needs a special analysis setup which has been already proven in earlier works [36, 63]. The general concept is to combine a carrier gas probe (CGP) with a MOG array as illustrated in a sketchy drawing in Fig. 21. A constant carrier gas stream is led to CGP made up of stainless steel which provides small gas permeation channels covered by a gas permeable membrane (silicone rubber). This membrane separates the carrier gas from the aqueous analyte. Non-dissociatively dissolved VOCs permeate through the gas permeable membrane from the liquid phase to the gas phase and are transported with the carrier gas to the measurement cell, complemented with the MOG-array (Fig. 21).

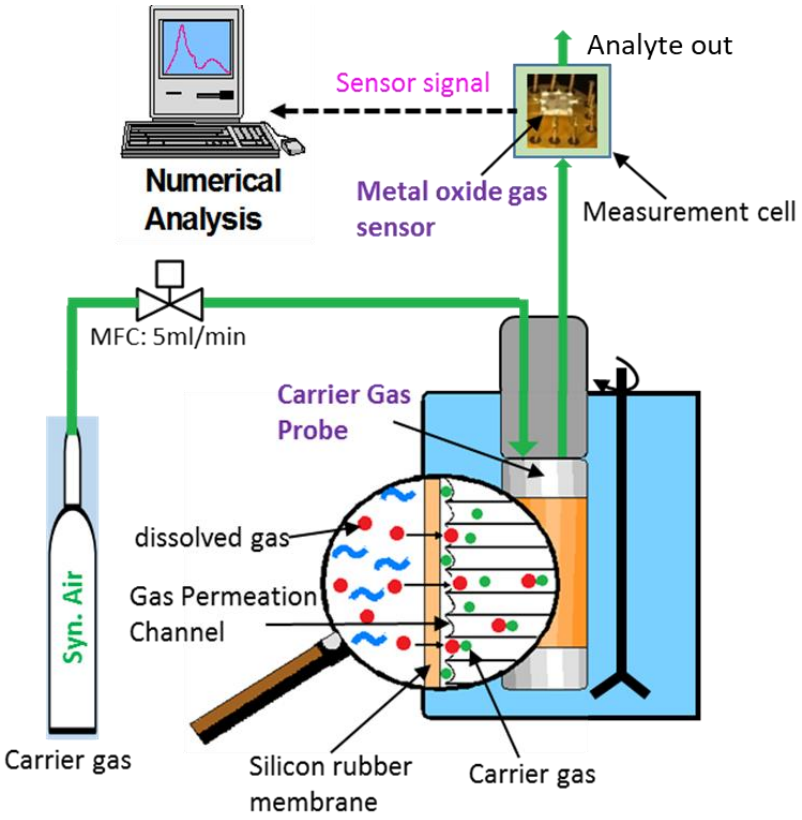

Fig. 21: Schematic representation of the concept for in-situ analysis of dissolved gas by combination of a CGP with an MOG array. Adapted from [63].

Regarding the functional dependency of the analyte concentration in the carrier gas, two aspects must be taken into consideration. First, the partial pressure, p, in the gas phase of physically, i.e. non-dissociatively dissolved VOC for low concentrations is proportional to its liquid phase concentration, c, according to Henry's law (eq. (26)),

$$p = K_H \cdot c \tag{26}$$

K_H is the analyte specific Henry's law constant. Indeed, p in the carrier gas is very low. It depends on the gas permeability of the membrane, on the contact time of the carrier gas with the membrane (carrier gas flow rate), and on the temperature.

Second, at a given construction of the CGP, the main physical parameter that dictates the relative concentration of the analyte in the carrier gas transported to the sensor is the carrier gas flow rate [63]. As lower the flow rate is, the longer is the contact time between the carrier gas and the analyte taking up by the carrier gas permeating across the silicon rubber membrane. Thus, relative concentration of the analyte would reach its maximum at thermodynamic equilibrium, i.e. when the carrier gas flow rate is zero. However, this is impracticable because there would be no gas transported to the sensor chip. Thus, to maximize the sensitivity, a compromise has to be found between a high analyte concentration in the carrier gas (low flow rate) to produce high gas sensitivity, and enough analyte transported to the sensor chip, having in mind, that there is some considerable consumption of the analyte at the surface of the MOG by the reaction with adsorbed oxygen states (Sec. 2.1.2). This aspect is discussed in detail with experimental data in Sec. 3.4.2 and Sec. 4.3.1.

2.5. Biogas fermentation process by anaerobic digestion

2.5.1. Basics of anaerobic digestion

In anaerobic digestion, different organic substrates, such as municipal solid waste, agricultural waste [47], food waste [5, 53], fruits and vegetable waste [46], livestock manure [45, 53], etc. are transformed into biogas which is mainly constituted by methane (CH_4), carbon dioxide (CO_2) and hydrogen (H_2) with other trace gases like carbon monoxide (CO) [120], hydrogen sulphide (H_2S), Ammonia (NH_4), alcohols and some other aromatic compounds. The overall process is composed of four different phases: hydrolysis, acidogenesis, acetogenesis, and methanogenesis as schematically illustrated in Fig. 22 [3, 9, 121].

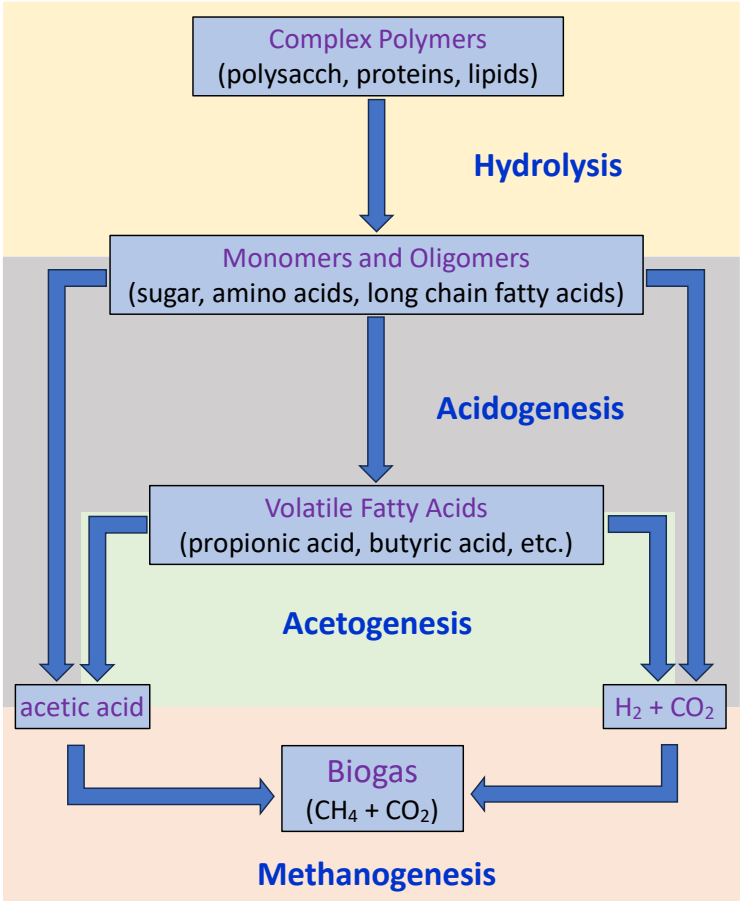

Fig. 22: Subsequent steps of the biogas fermentation process.

In the hydrolysis process, the complex organic compounds, such as carbohydrates, proteins, and fats are broken down into the soluble oligomers and monomers, such as amino acids, sugars, and fatty acids by means of enzymes released by the hydrolytic bacteria [9, 122]. The hydrolysis

process itself involves several other processes in steps including enzyme production, diffusion, adsorption, reaction, and enzyme deactivation steps.

The intermediate products from the hydrolysis process are further broken down in the acidogenesis phase by the fermentative or acid-forming bacteria to form different VFAs (acetic, propionic and butyric acid) along with CO_2, H_2 and small quantities of lactic acid and alcohols [123]. The optimum pH for hydrolysing and acid-forming bacteria is in the range from pH 5.2 to 6.3. These bacteria are not totally reliant on this pH value but are even capable to convert substrates at a slightly higher pH value.

In the acetogenesis phase, the intermediate products from acidogenesis phase i.e. VFAs and alcohols are converted into acetic acid by the acetogenic bacteria. In this way, the precursors of biogas i.e. acetic acid, H_2 and CO_2 are formed [123]. The hydrogen partial pressure is particularly important, and an excessive hydrogen content prevents the conversion of intermediate products of acidogenesis to acetic acid [1]. As a consequence, the VFAs like acetic and propionic acid accumulate and may cause decrease of the pH to a low value such that the hydrolysis/acetogenesis can be inhibited [123] which can completely stop the formation of methane in the following methanogenesis phase.

During the final phase of biogas formation, i.e. methanogenesis phase, all the acetic acid as well as hydrogen and carbon dioxide formed during previous phases are converted into methane by strictly anaerobic methanogenic archaea. Commonly, acetotrophic methanogenic microorganisms decompose the acetate to form CH_4 and CO_2 whereas, hydrogenotrophic methanogens consumes H_2 and CO_2 to produce CH_4. [123, 124]. The pH value in the neutral range from 6.1 to 8 [125] is absolutely essential for acetic acid forming bacteria (acetogenesis) and methane forming methanogens (methanogenesis). Consequently, if the fermentation process takes place in single digester systems, this pH range must be maintained.

Based on the optimal working temperature of different microorganism, the microorganisms could be categorized as psychrophilic (< 20°C), mesophilic (35°C-42°C) [9] and thermophilic microorganism (45°C-60°C) [9]. Since the individual phases of anaerobic digestion and the involved microorganisms have different requirements, for example pH value and temperature, different stages must be coordinated with each other in best possible way to ensure that the overall process runs smoothly.

2.5.2. Monitoring parameters for biogas fermentation process

As discussed in Sec. 2.5.1, the biogas fermentation process is a combination of different complex sub-processes involving different microorganisms which are very sensitive to different operational conditions for e.g. pH and temperature. Thus, it is necessary to monitor the key indicators that represent any process imbalances already in the early stage so that appropriate action can be started to avoid any process failure. Use of different indicators for monitoring the stability of the fermentation process are reported in the literature and some of the process indicators are as following:

i. Methane and carbon dioxide ratio

The main constituents of the biogas are CH_4 and CO_2. Their ratio is normally stable. Thus, any change of the ratio could indicate process imbalances. However, this ratio can fluctuate with changes of different other parameters like temperature and pH. Especially dissolution of CO_2 is strongly pH dependent and any fluctuations in pH can change the gas composition.

ii. pH

pH is one of the parameters that is measured easily and very reliably online in the biogas fermentation process for e.g. by use of a pH-glass electrode. As discussed earlier, since the microorganisms are effective only in some specific pH range, change in the pH is a good indicator of process imbalance. In reactors with low buffering capacity, VFA accumulation can cause quick decrease of pH. In such cases, pH is considered as an effective process indicator. However, in well buffered reactors due to the high buffering capacity the change of pH from the VFA accumulation is rather slow and too small. In such cases, pH cannot represent the actual VFAs situation of the biogas fermentation process and cannot be a reliable indicator of process imbalance. In this case, pH measurement combined with VFA measurement is suggested to be more effective for monitoring of the actual process situation [1].

iii. Hydrogen

H_2 is an important intermediate product and is a precursor to the CH_4 formation. However, high H_2 concentration can inhibit acetogenesis and activity of methanogens, resulting in VFA accumulation which may lead to overall process failure [124]. Additionally, high H_2 concentration may negatively affect the hydrolysis process [126]. Thus, hydrogen accumulation

has been suggested as early indicator of process imbalance and has been reported to be used as an indicator [127].

iv. Carbon monoxide

CO as a process indicator has not been commonly used. However, CO has been reported to evolve during the methanogenesis phase from acetate [128] and was found in significant concentrations during toxic inhibition by heavy metals. The concentration of CO has been reported to be directly related to acetate concentration and inversely related to CH_4 concentration [129]. CO along with H_2 are reported to provide information regarding the metabolic status of some of the key bacteria groups [127].

v. Volatile fatty acids

As discussed earlier, VFAs are one of the most important intermediates [123] in the fermentation process. However, accumulation of these VFAs beyond certain limits can be toxic to the microorganisms, especially to methanogens [123]. Different reactor systems have their own normal levels of VFAs which are determined by the operating conditions [130]. VFAs accumulation during process directly reflects a kinetic uncoupling between the acid producers and consumers. Hence, the VFA concentration is an important indicator which provides fast and reliable information of the process status [3, 49, 58] and has been highly recommended for monitoring and accurate control of the fermentation processes [7]. Particularly in highly buffered systems, only the VFA-concentration is a direct and reliable indicator of process imbalance. In several studies, it was concluded that the information about the individual VFAs concentrations provide more reliable information about the actual process status [3, 7, 122]. Additionally, it has been reported that the development of propionic acid is affected earlier than other VFAs in case of increased H_2 partial pressure resulting in its accumulation. Thus, propionic acid concentration is suggested to be the better indicator to provide early warning of process imbalance [1, 11]. Some studies have suggested to use the variation of propionic to acetic acid ratio as the indicator of process failure [8, 48].

Hence, monitoring of the individual VFAs to detect any imbalance in the process prior to the complete process failure would be an important step for proper control and optimization of the biogas fermentation processes in general. In addition, the use of other indicators, such as alkalinity ratio [10], VFA/TA [131], and gas composition [1, 7] is also reported in different studies.

2.6. In-situ monitoring of dissolved VFAs in biogas processes using MOG

2.6.1. Concept for in-situ analysis of VFAs dissolved in fermentation liquids

The concept of in-situ analysis of VOCs dissolved in DI water by the operation of a CGP with a thermo-cyclically operated MOG array is already introduced in Sec. 2.3.3. However, in-situ analysis of dissolved VFAs in anaerobic digestion requires a special pre-conditioning treatment of the fermentation sample due to the well-known cross-sensitivity of MOG to biogas components like CH_4, CO, H_2, etc. and to other intermediate VOCs developing at these process conditions. This pre-conditioning treatment is well introduced in [117] and is described below in a more general manner:

In a first step, a well-defined volume of the biogas fermentation liquid is extracted from the main reactor and transferred to another reactor (here, this is the reactor used for the analysis experiments), which could be referred as the analysis-reactor. The required volume of the extracted sample depends on the volume of the analysis-reactor with a criterion that the silicon rubber membrane of the CGP in the analysis-reactor is completely immersed in the fermentation sample. This is absolute necessary for proper functioning of the CGP. In the analysis reactor, pH of the sample is first shifted to an alkaline value (pH 8) by dosage of potassium hydroxide. This allows complete transformation of the dissolved organic acids to the dissociated state and, afterwards, enables purging out of the biogas (CO_2, CH_4, CO, H_2, etc.) and all other non-dissociated, physically dissolved gas components which may contribute to the sensor signal, by a high flow of inert gas, e.g. N_2, without losing dissolved VFAs.

After this purging procedure, a first CTP, referred as CTP-ref, is sampled for reference and same operation condition (i.e. constant carrier gas flow, 5 ml/min) of CGP is used for the later measurement. This CTP-ref may be characterized by all residual gas components (water vapor, residual biogas, etc.) at this pH-condition, but per se is formed without the VFAs, because their pKa is about 4.8 (Fig. 23), which is well below the actual pH value of 8. The CGP enables the uptake of undissociated molecular dissolved organic acids from the liquid state into the constant flow of synthetic air (carrier gas: 5 ml/min) by permeation through the gas permeable silicon rubber membrane. Via the carrier gas, the permeated gas molecules are transported to the MOG arrays for analysis at a condition of high and constant oxygen concentration determined by the kind of carrier gas (synthetic air). The latter aspect is important for reliable gas analysis with MOG in general.

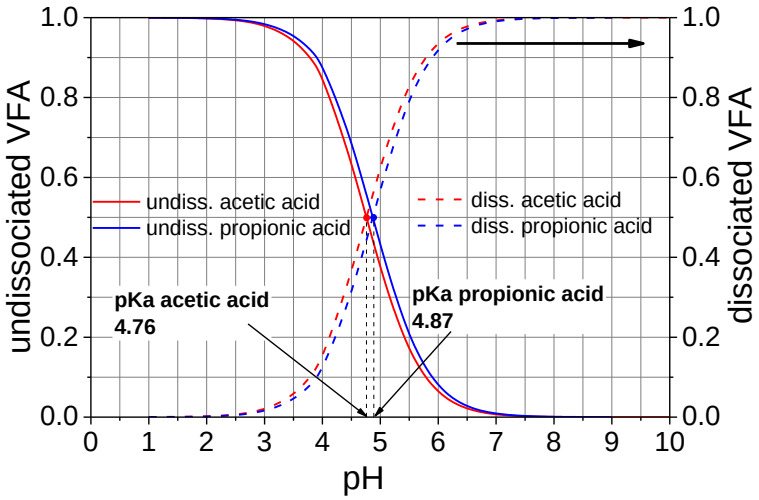

Fig. 23: Relation of dissociated and undissociated state of acetic and propionic acids at different pH-values. Adapted from [117].

In the second step, the pH is shifted in steps up to pH 3, which is clearly lower than the pKa value of the organic acid dissociation equilibria under investigation. This is achieved by dosage of phosphoric acid. Now the organic acids are shifted to the non-dissociated state (Fig. 23) and correspondingly, the partial pressure of these molecules is now high in the liquid state depending on their concentration. This induces diffusion across the gas permeable membrane and is reflected in a gas component specific change in the CTP-features in relation to the CTP-ref sampled at pH 8 condition. There is an individual but good approximation between the concentration of the organic acid in the liquid phase and the integral of the CTPs observed in the concentration range under investigation using a power law [63].

3. EXPERIMENTAL

3.1. Sensitive material synthesis

Pure SnO_2 powders of nanoscaled grain size were produced following two different synthesis routes (Sec. 3.1.1), (i) the sol-gel (SG) method and, (ii) the Flame-Spray-Pyrolysis (FSP) method. Each type of powder i.e. SnO_2(SG), and SnO_2(FSP) was admixed with different additive powders. The choice of these additives is based on an extensive literature survey and an extended screening procedure in which different SnO_2/additive and ZnO/additive composites were investigated. An overview about these composites is listed in Appendix 1. Finally, three additive candidates were selected, which promised the highest sensitivities and most characteristic CTPs to acetic acid. These are alumina (MZS-1 (Martinswerk GmbH, Bergheim, Germany)), Yttria-stabilized zirconia (YSZ) (TZ-8YS (Tosoh Corporation LTD, Amsterdam, Netherland)) and sodium super ion conductor (NASICON) (self-prepared at Institute of Sensor and Information Systems (ISIS), Karlsruhe University of Applied Sciences (KUAS)) by ball milling.

Finally, all powders were transformed to printable pastes and deposited on pre-prepared chips (Sec. 3.2) with a heater on the reverse side and four Interdigital Electrodes (IDEs) on the top side to fabricate single-chip four-fold sensor-arrays. Thus, four-fold sensor chips of two different kinds were achieved, one with SnO_2(SG)/additive-layers and others with SnO_2(FSP)/additive layers. This means, both kinds of chips provide the same SnO_2/additive-combinations but differ by the kind of SnO_2-powder preparation route, by the layer thickness and by limited reproducibility of the layer geometry achieved by micro-dispensing of the pastes.

3.1.1. Synthesis of SnO_2 powder

The SG prepared SnO_2 powder, SnO_2(SG), was prepared at ISIS, KUAS. The synthesis route of SnO_2(SG) is described in detail in [38, 63, 132]. Pure $SnCl_4$ (Sigma-Aldrich) was slowly dropped in deionized water. The obtained sol was transformed into a gel by addition of ammonia solution. After aging the gel for 3 weeks, it was washed for several times with deionized water and ethanol to get it almost free of the chloride ions. The gel was then stirred, dried at 80 °C and ground for 6 h at 200 rpm in zirconia vessels by ball milling. A fine pale yellow SnO_2 powder was obtained after pre-sintering at 450 °C for 5 h.

A very promising alternative route for preparation of extremely fine SnO_2 nanoparticles is the FSP method, which is described in detail in [133]. In a recent review [134], the exceptional properties of FSP prepared nanopowders are illustrated and the different methods of deposition on sensor element substrates by either drop coating and annealing of flame-made nanoparticles or by direct combustion chemical vapor or aerosol deposition are discussed as well as the sensing properties are compared. In short, very fine SnO_2 nanoparticles and agglomerates are formed by the combustion of the liquid precursor (tin(II)-ethylhexanote) in the flame. The size of the nanoparticles is well controlled and depends on the Sn concentration in the precursor and the flame operation conditions. Further, very narrow particle size distributions can be achieved by this novel preparation route. In this work, the SnO_2(FSP)-powder was provided by our cooperation partner (Prof. Dr. Andreas Güntner, Dept. of Mechanical and Process Engineering, ETH Zürich (CH)). The "drop coating route" was applied, i.e. in analogy to the SG-prepared materials the FSP-prepared nanopowders were admixed with additives and then transferred to a paste (Sec. 3.1.3), which was then deposited on pre-prepared chips with four IDEs by a micro-dispensing technique.

3.1.2. Choice of additives and preparation of NASICON

As already mentioned above, two sensor array chips were prepared for comparison of the sensing performance of SnO_2(SG)/additive-layers with SnO_2(FSP)/additive-layers. This means, both chips consist of the same SnO_2/additive-combinations (pure SnO_2, SnO_2/Alumina, SnO_2/YSZ, SnO_2/NASICON) but differ by the SnO_2 preparation routes. Alumina and YSZ are commercially available fine powders. However, ($Na_{1+x}Zr_2Si_xP_{3-x}O_{12}$, $0 \leq x \leq 3$), one of the most famous sodium solid electrolytes with high sodium ionic conductivity [135] was prepared at ISIS, KUAS.

The sodium content of the NASICON-framework structure [136, 137] can be widely varied and the ionic conductivity achieves its maximum at about x=2 [138]. Due to its rather good chemical stability, NASICON gained rising importance in the last four decades as separator or even as cathode material for high temperature solid state rechargeable batteries [139, 140] and was discussed as a good candidate for development of all solid-state gas sensor elements [141]. NASICON ($Na_3Zr_2Si_2PO_{12}$, x=2) was prepared following a well-known SG-route [63, 142]. $ZrO(NO_3)_2 \cdot 8H_2O$ (Sigma-Aldrich), Na_3PO_4 (Sigma-Aldrich), $Si(C_2H_5O)_4$ (Sigma-Aldrich), and $C_6H_8O_7 \cdot H_2O$ (Carl Roth GmbH, Karlsruhe, Germany) were weighed accurately in a molar ratio of 2:1:2:2 and dissolved individually in DI water. First, the silica sol was prepared by

continuous admixing of $Si(C_2H_5O)_4$ and DI water at volume ratio of 1:100 by continuous magnetic stirring for 2 h at ambient conditions.

$ZrO(NO_3)_2 \cdot 8H_2O$, Na_3PO_4, and $C_6H_8O_7 \cdot H_2O$ solutions were added to the silica sol one after the other. The resulting mixture was continuously stirred for 1 h at 50°C under sealed conditions. The resulting sol was aged for 3 h at 20°C and was calcinated at 80°C resulting in a white powder. The powder was ground at 200 rpm for 1 h in zirconia vessels using a planetary ball mill. Afterwards, the powder was sintered at 800°C for 2 h, at 900°C for 3 h and at 1000°C for 4 h successively and all samples were characterized by XRD (Sec. 4.1).

3.1.3. Paste preparation for microdispensing

By admixing pure SnO_2 powder with organic binder (DSSP 80820-MD, Ferro GmbH, Frankfurt am Main, Germany) and terpineol (Carl-Roth GmbH, Karlsruhe, Germany) by ball milling (planetary ball mill (Fritsch GmbH, Idar-Oberstein, Germany) with vessels and balls, both made of Zirconia-ceramics) for 2 h at 120 rpm, two different set of pastes were prepared using SG and FSP synthesized SnO_2 as starting powders. The resulting pastes were denoted as SnO_2(SG) and SnO_2(FSP).

For preparation of the SnO_2/additive pastes, the SnO_2(SG) as well as the SnO_2(FSP) powder were first admixed with alumina, YSZ and NASICON(x = 2) powders in a volume ratio of 4:1, respectively by ball milling. Then, these mixed powders were transferred into pastes by admixing with an organic binder and terpineol in the ball mill in a similar procedure as described above for making pure SnO_2 pastes. The pastes were denoted as SnO_2(SG), SnO_2(SG)/Alumina, SnO_2(SG)/YSZ, SnO_2(SG)/NASICON, SnO_2(FSP), SnO_2(FSP)/Alumina, SnO_2(FSP)/YSZ, and SnO_2(FSP)/NASICON.

3.2. Fabrication of 4-fold sensor array chips

The four-fold MOG array chips (size: 4 × 4 mm^2) comprise four IDEs as well as a resistive Pt-temperature sensor at the top side and a Pt-heater at the reverse side (Fig. 24a). They were prepared using DC sputtering, photolithography and plasma etching techniques at ISIS, KUAS following the process steps as shown in Fig. 25. Each Pt-IDE thin film structure consists of ten fingers with 50 μm in width and 50 μm distance to the neighbouring fingers. The thin-film Pt-layer thickness is about 1 μm.

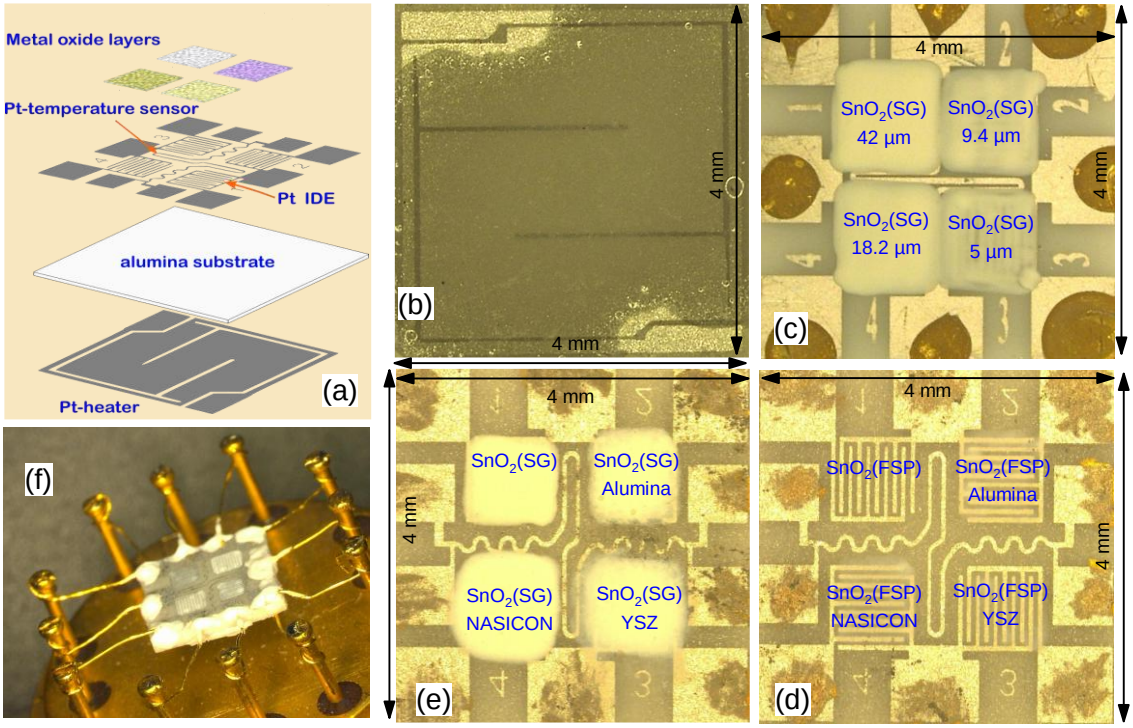

Fig. 24: Sensor chip preparation and housing. (a) Schematic illustration of different components of a 4-fold sensor chip in exploded view. (b) Glass passivated Pt-heater structure with contact pads on the reverse side of the sensor chip. (c) Sensor array SA#3 with four different SnO_2(SG)-layers with different thickness. (d) Sensor array SA#1 with different SnO_2(FSP)/additive-layers. (e) Sensor array SA#2 with different SnO_2(SG)/additive-layers. (f) 4-fold sensor array chip mounted on a TO-8 header. Adapted from [63].

On the four Pt-IDEs of the sensor array chips, namely SA#1 and SA#2, four different FSP-prepared and SG-prepared pastes were deposited employing a microdispensing technique ((DOTLINER 06, Martin GmbH, Wessling, Germany), as shown in Table 1. Similarly, on the four Pt-IDEs of third sensor chip (SA#3), four SnO_2(SG)-layers of different thickness were deposited. With these SnO_2(SG)-layers of different thickness, the influence of the layer thickness on the sensing behaviour was investigated (Sec. 3.4.3). Generally, the thickness of

the micro-dispensed layers is determined by the pressure applied on the paste in the syringe, the viscosity of the paste, the inner diameter of the needle (110 μm) and the needle velocity across the area to be covered. Layer thickness beyond the thickness of a monolayer was achieved by repetitive dispensing on previously dispensed and dried layers at ambient conditions before sintering.

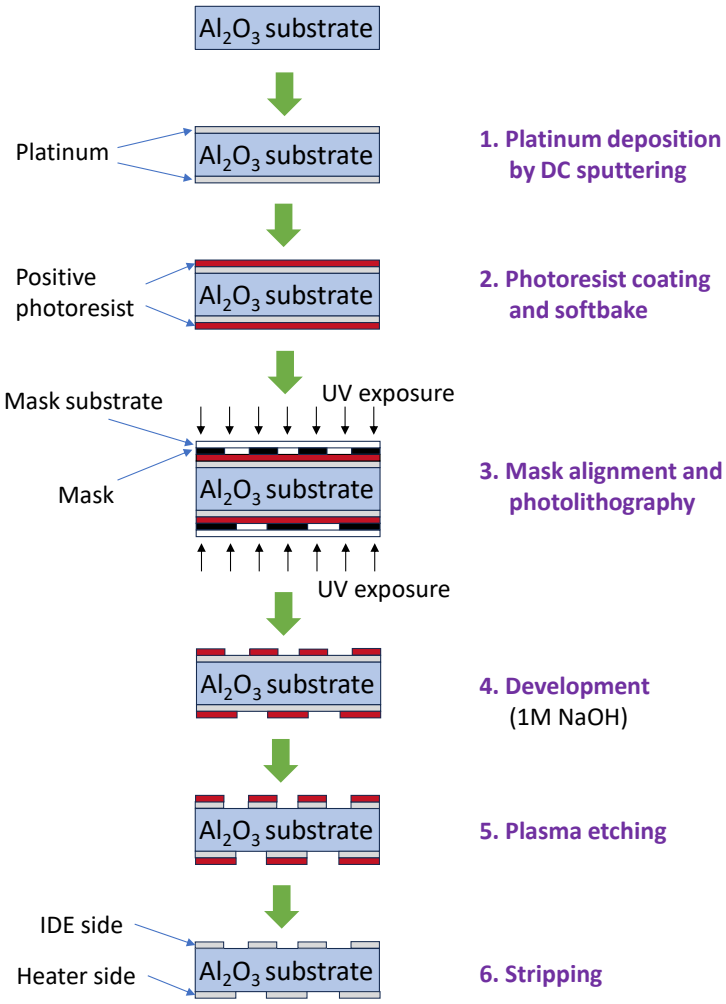

Fig. 25: 4-fold sensor array chip fabrication process steps using thin film technology. The process details are summarized in Appendix 2.

After dispensing, the layers were subsequently dried at ambient conditions overnight and then sintered according to a well-defined sintering profile (Fig. 26) [143]. During the sintering process, the dried layers were exposed to different temperatures for different time duration. At 350°C (15 min) the residual organic solvents in the sensitive layers are removed. Sintering at 500°C (300 min) allows to adjust the layer properties (oxygen vacancy defects) to the maximum operating temperature and finally, sintering at 700°C (20 min) allows to further increase the

mechanical stability of the layers by the formation of intergranular necks at the grain boundaries and sintering contacts with the alumina-substrate.

Table 1: Overview of microdispensed SnO_2/additive-pastes on SA#1 and SA#2.

	Sensitive layers deposited	
	SA#1	SA#2
IDE1	SnO_2(FSP)	SnO_2(SG)
IDE2	SnO_2(FSP)/Alumina	SnO_2(SG)/Alumina
IDE3	SnO_2(FSP)/YSZ	SnO_2(SG)/YSZ
IDE4	SnO_2(FSP)/NASICON	SnO_2(SG)/NASICON

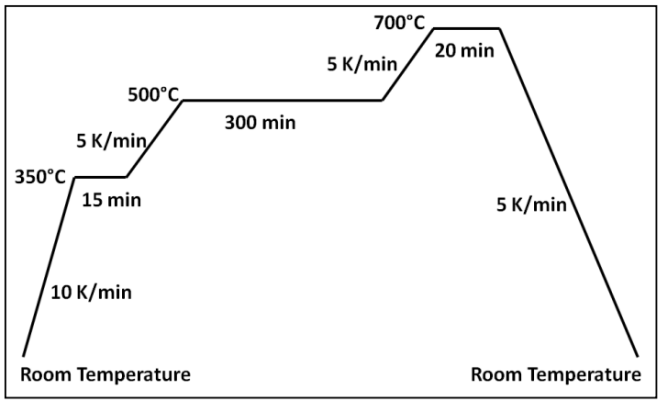

Fig. 26: Sintering profile of the SnO_2 and SnO_2/additive-composites.

The sintered FSP-layers (Fig. 24d) and SG-layers (Fig. 24e) look clearly different. FSP-layers are highly transparent in comparison to SG-layers. There is also clear difference in the layer thickness between FSP-layers and SG-layers (Sec. 4.2, Fig. 41). Additionally, as will be discussed in Sec. 4.2, the ESEM analysis (Fig. 37 and Fig. 39) disclosed that the SG-layers have clearly bigger average particle size and are more densely packed in comparison to the highly porous FSP-layers which have extremely small average particle size. Both aspects are assumed to result in much smaller light scattering intensities of the FSP-layers which in turn may explain the differences in transparency. Afterwards, both chips were mounted on TO-8 headers using a Unitek Modell “Unibond II” (Weld-Equip Deutschland GmbH, Germany) micro-gap welding setup. Both four-fold sensor array chips consist of the same SnO_2-additive combinations but differ by the SnO_2 preparation routes (SG and FSP) and this means, differ by the morphology (grain size and distribution) of the SnO_2 as well as by the mean layer thickness and overall thickness profile.

3.3. Characterization of tin oxide/additive- composites

Rigaku Miniflex 600, Cu K-alpha X-ray diffractometer (Rigaku Inc., Tokyo) at ISIS, KUAS was used for the XRD analysis of the SnO_2(SG) powder (Sec. 3.1.1) and NASICON powder (Sec. 3.1.2). Similarly, AXS D8 Advance Diffractometer (Bruker, www.bruker.com) was used by our cooperation partner (Prof. Dr. Andreas Güntner, Dept. of Mechanical and Process Engineering, ETH Zürich (CH)). for XRD analysis of SnO_2(FSP) powder [133].

Further, an environmental scanning electron microscope (ESEM) type Quattro (Thermo Fisher Scientific) equipped with a field emission gun (FEG) was used in cooperation with the Institute of Functional Interfaces (IFG) at Karlsruhe Institute of Technology (KIT) to study the surface morphological structures of different SnO_2/additives-layers listed in Table 1.

In addition, grain compositional analysis of the different SnO_2/additives-layers (Table 1) was performed using an Octane Elite Super energy dispersive spectroscopy (EDS/EDX) system at IFG.

Finally, the layer thickness and homogeneity of different SnO_2/additives-layer was studied using a μsurf explorer confocal microscope (NanoFocus AG, Germany) at ISIS, KUAS.

3.4. Gas sensing tests with model VOCs

3.4.1. Measurement setup for analysis of dissolved model VOCs in DI water

The scheme of the experimental setup for analysis of physically, this means, non-dissociatively dissolved VOCs in the aqueous liquid (at 18°C) of a thermostated bioreactor, here referred as analysis reactor, complemented by a CGP (Fig. 27d) is illustrated in Fig. 27a. The corresponding experimental setup in laboratory is shown in Fig. 27b.

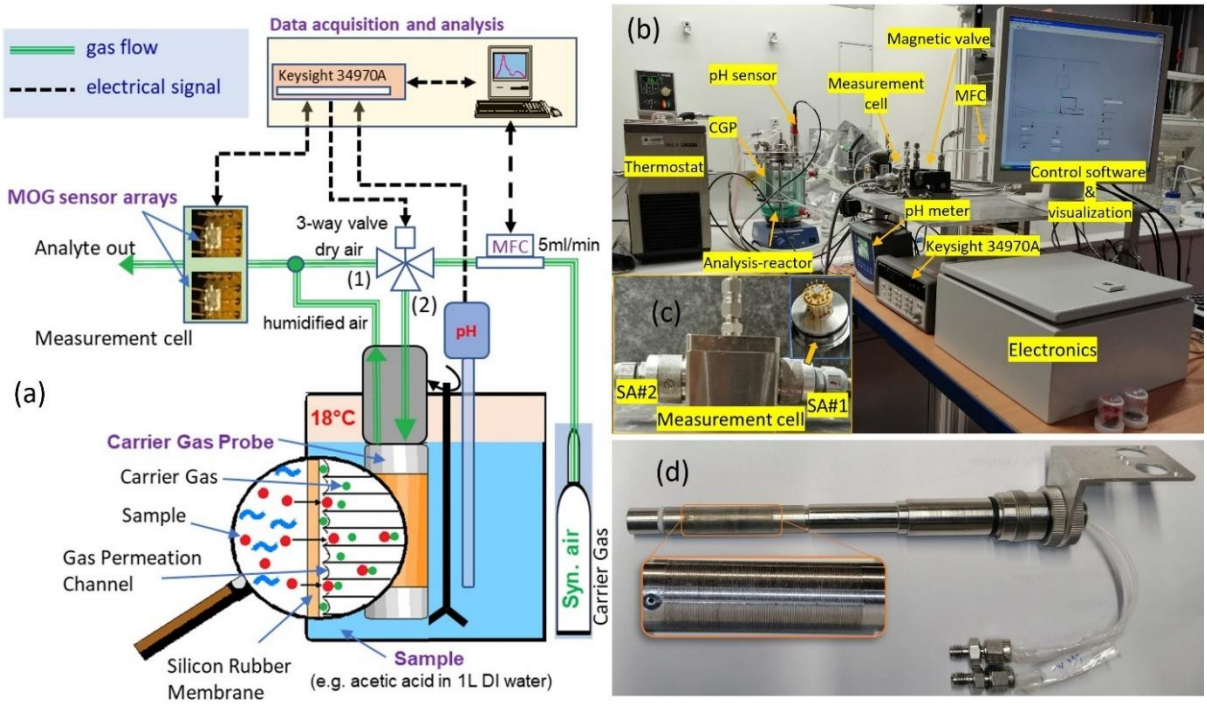

Fig. 27: (a) Schematic representation of the setup for analysis of dissolved model-VOC by a combination of a CGP with two MOG array-chips. (b) Experimental setup in laboratory, (c) measurement cell with two sensor arrays; a senor chip is shown as mounted in a holder (inset). (d) CGP showing the fine permeation channels (magnification as an inset) covered with silicone rubber membrane. (a) adapted from [63].

The methodology of analysis of dissolved gases using CGP was already discussed in Sec. 2.4. A carrier gas flow (5 ml/min) is kept constant by a commercial mass flow controller (MFC). The pH of the analyte is checked by a pH-sensor and homogeneity of the analyte is achieved by continuous stirring. The gaseous analyte as extracted from the liquid sample via the CGP is led to the measurement cell (Fig. 27c), consisting of two thermo-cyclically operated sensor arrays (SA#1 and SA#2), by setting the magnetic valve in position (2). Alternatively, if the sensor arrays must be exposed to dry synthetic air as per requirement, the 3-way magnetic valve

is set to position (1). This setting is typically used during aging of the sensors and during the cleaning of the reactor after the experiments with individual VOCs.

A Keysight 34970A data acquisition unit was used for operating the 3-way valve and for simultaneous measurement of the 128 conductance sampling points per temperature cycle of each gas sensitive layers together with the resistance of the Pt-temperature sensor (Fig. 24a) microstructured on the top side of each sensor array chips (SA#1 and SA#2) as well as for recording the pH value. The Pt-temperature sensor resistance (Fig. 28b) was transformed to the actual surface temperature (Fig. 28b) using the calibration data experimentally determined in a temperature controlled tubular furnace in advance. The corresponding triangular heating voltage (Fig. 28a) for continuous temperature cycling of the sensor array chips (SA#1 and SA#2) between 150(±5)°C and 450(±5)°C was generated by the Digital to Analog Converters (DACs) of the same data acquisition unit. The control program (Sec. 3.5.3) could communicate with the Keysight 34970A and the MFC directly via serial communication.

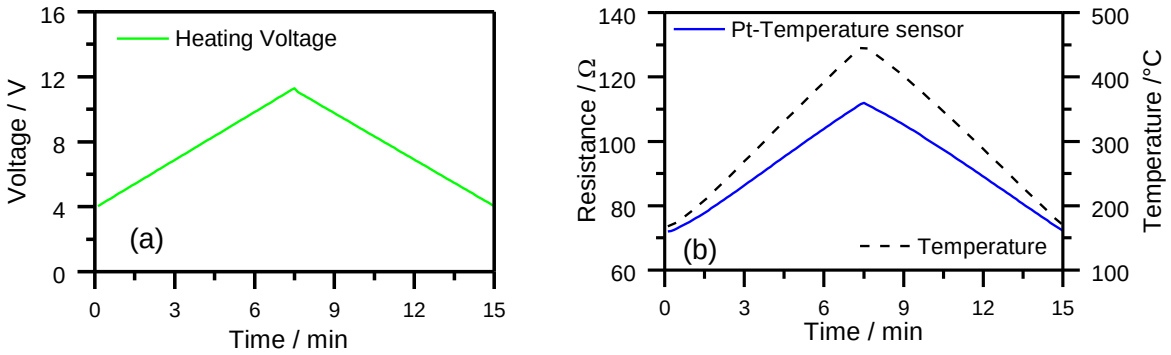

Fig. 28: Sensor operation methodology. (a) Applied heating voltage (b) corresponding temperature sensor resistance and estimated sensor temperature over one temperature cycle for SA#1.

3.4.2. Optimization of measurement conditions

As already stated in Sec. 2.4, the measurement conditions with respect to the carrier gas flow rate and the temperature cycling period had to be experimentally estimated to optimize the response of such sensor chips. To make this optimization at representative conditions related to the upcoming experiments, two sensor array chips with four sensitive layers each were operated in the measurement cell simultaneously and CTPs of one of the layers, SnO_2(FSP)/1%Pd-layer [133], at exposure to 4% acetic acid dissolved in DI water at pH 3, were analysed at a cycle-time of 3 min at different carrier gas flow rates (2.5, 5, 10 and 20 ml/min). In the next step, at constant carrier gas flow rate (5 ml/min), the dependency of the CTP on the temperature cycling

period was investigated with the same sensitive layer but at cycling periods of 3 min, 15 min and 30 min. In this case, 2000 ppm acetic acid dissolved in DI water was used as the analyte.

3.4.3. Influence of the layer thickness on CTPs

The sensor array chip SA#3 with different thickness of the SnO_2(SG)-layers (5 µm, 9.4 µm, and 18.2 µm) was exposed to different concentrations of acetic acid (500 ppm, 1000 ppm, and 2000 ppm) dissolved in DI water at pH 3 by use of the setup as described in Sec. 3.4.1. The measurements were performed at the optimal carrier gas flow rate of 5 ml/min and at the temperature cycling period of 15 min (Sec. 4.3.1). The influence of the layer thickness on the CTP-shape and the dependency of the CTP integrals on layer thickness is discussed in a representative manner in Sec. 4.3.2 by illustration of the CTPs measured at 2000 ppm of acetic acid dissolved in DI water at pH 3 as an example.

3.4.4. Influence of morphology and of additives on the sensing properties and CTPs

Two sensor arrays SA#1 and SA#2 consisting of SnO_2(FSP)/additive-layers and SnO_2(SG)/additive-layers respectively (Fig. 24d and Fig. 24e) were aged simultaneously in the same measurement cell as introduced in Sec. 3.4.1 at a constant flow rate (5 ml/min) of synthetic air (about 2 ppm humidity) as provided in the gas bottle by the supplier (Linde GmbH, Germany) and at the optimal temperature cycling period of 15 min (Sec. 4.3.1). The aging of MO gas sensitive layers is necessary [89] to adjust the oxygen defect concentration, to stabilize the morphology (post sintering effects) and to allow the gaseous impurities to desorb before the measurements are started. After the conductance values of the sensitive layers did not further change significantly in terms of a day (about 120 h of continuous thermo-cyclic operation), the last CTP (synth. air) was taken as the Go(dry air)-curve.

Table 2: Henry law constants (T=25°C) of the VOCs used in sensitivity measurement tests.

VOC	K_H / atm.kg.mol^{-1}	Reference
acetic acid	1.852×10^{-4}	[144]
propionic acid	1.785×10^{-4}	[144]
ethanol	5.263×10^{-3}	[145]
acetone	38.46×10^{-3}	[145]

After this aging procedure applied to both SA#1 and SA#2, all the following conductance measurements were performed at the optimal carrier gas flow rate of 5 ml/min using the temperature cycling period of 15 min. The sensor responses were studied for different liquid phase concentrations of acetic acid, propionic acid, ethanol, and acetone dissolved in DI water at 18°C (Sec. 4.3.3), which are relevant for later studies of those compounds in biogas fermentation samples (Secs. 3.5.4 and 4.4). Liquid phase concentrations as used for the measurements and corresponding gas phase concentrations at 25°C as calculated using eq. (26) and K_H (Table 2) are given in Table 3. According to the Van't Hoff approximation in systems near ambient temperature [146] the values of K_H generally decrease exponentially with decreasing temperature. For example, calculated K_H(18°C) for acetic acid is lower than K_H(25°C) by a factor of 0.985. Thus, the real gas phase concentrations adjusted in the sensitivity measurement tests are expected to be slightly lower than the values presented in Table 3. At each concentration step, at least 12 CTPs were recorded, and the last CTP was used for data illustration.

Table 3: VOCs liquid phase concentration used for the sensitivity measurement tests and corresponding gas phase concentrations as calculated using eq. (26) at T=25°C.

acetic acid / ppm		propionic acid / ppm		ethanol / ppm		acetone / ppm	
liquid phase	gas phase	liquid phase	gas phase	liquid phase	gas phase	liquid phase	gas phase
100	0.3	100	0.24	-	-	-	-
200	0.6	200	0.48	-	-	-	-
500	1.5	500	1.2	15	1.7	2.5	1.6
1000	3	1000	2.4	30	3.4	5	3.2
2000	6	2000	4.8	60	6.8	15	9.5

3.5. Analysis of dissolved VFAs in fermentation samples

3.5.1. Preparation of the fermentation samples

The fermentation samples were prepared using biological substrate from a sewage plant in two glass reactors (1 l volume each) with a stainless-steel top cover providing outlet for biogas collection (Fig. 29c). Over several months at room temperature condition, it was fed with beer marc (Fig. 29a), dried at 60°C for several days, and wood juice (Fig. 29b) [64, 147]. The latter material was mechanically dewatered from wood chips using a wood chip squeezer. 50 ml of wood juice and 10 mg of beer marc were fed in intervals of 3 to 4 days. The pH of the sample was frequently monitored and was typically in the range of 6.5-6.8. Once the fermentation sample volume reached 1 l in each reactor, 500 ml of the fermentation liquid from each glass reactor was transferred to the analysis reactor (1 l volume) and well admixed by continuous stirring. This sample in the analysis reactor was then used for the sensitivity test measurements of the MOG-chips. In preparation of the next experiment, the remaining fermentation broths (500 ml) of both glass reactors were again fed with wood juice and beer marc in a procedure as mentioned above until the volume of the fermentation sample in each reactor again reached 1 l.

In this way, about 6 sensitivity test measurements of different MOG arrays using different batches of fermentation samples were conducted. Test results of some of the experiments are presented in Appendix 5-7. In this work, the sensitivity test measurements of the sensor arrays SA#1 and SA#2 (see Sec. 3.2), which are the most representative ones and therefore are extensively discussed.

Fig. 29: (a) Dried beer marc (b) wood juice (c) fermentation sample in a 1 l glass reactor with gas bag for biogas collection

3.5.2. Test setup and measurement sequence for evaluation of the VFA analysis concept

The experimental setup in Fig. 27a was expanded for the analysis of VFA dissolved in biogas fermentation liquids as illustrated in Fig. 30a. As already mentioned in the Sec. 3.4.1, constant carrier gas flow (5 ml/min of synthetic air) is set by the MFC1 and the gaseous analyte is extracted from the fermentation sample in the analysis reactor when the 3-way magnetic valve is set in position (2). The gaseous analyte is led to the measurement cell consisting of two thermo-cyclically operated sensor arrays SA#1 and SA#2 (see Sec. 3.2). Alternatively, as per requirement the sensor arrays must be exposed by synthetic air, the 3-way magnetic valve is set to position (1). This is typically necessary during refilling of the reactor with new bio fermentation liquid and during purging of the fermentation sample (Sec. 2.6.1) by a continuous flow of N_2 (500 ml/min) as adjusted with MFC2 (Fig. 30b). During this procedure of purging, the 3-way hand valve must be adjusted to enable "gas out". Alternatively, the 3-way hand valve is adjusted to "Gas bag", which is used for collecting the gas developing during the experiment. Collected gas is used for offline Fourier Transform Infrared Spectroscopy (FTIR) analysis (Sec. 3.5.5) if enough gas can be collected.

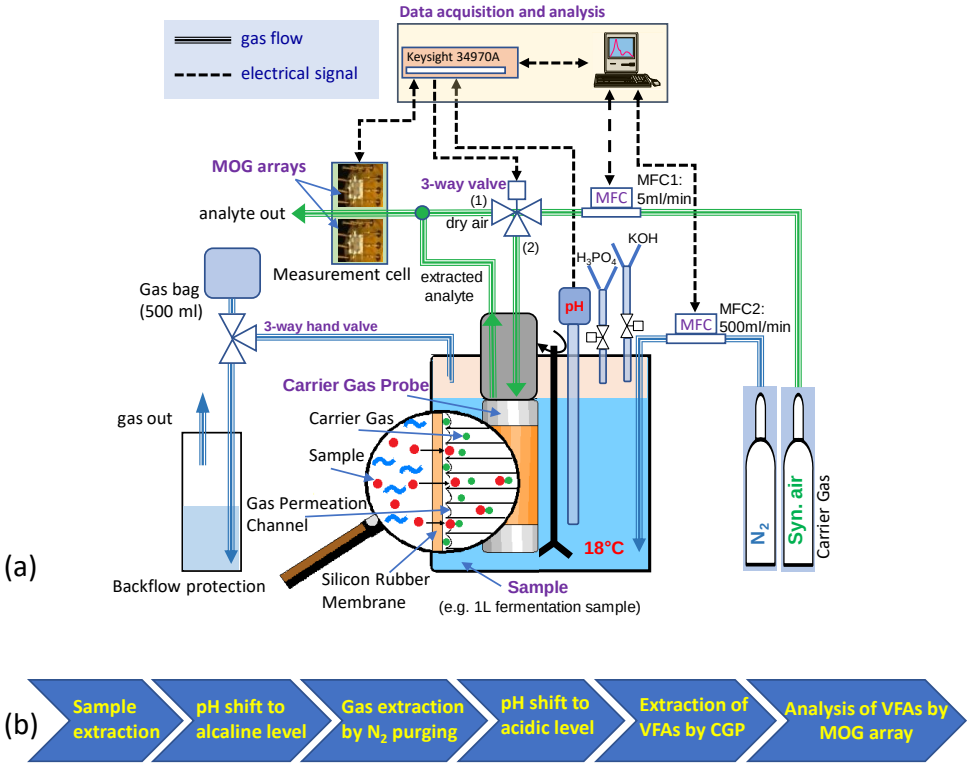

Fig. 30: Concept for analysis of VFA dissolved in biogas fermentation liquid. (a) Experimental setup, (b) scheme of the sequence of operation. Adapted from [117].

Like the setup described in the Sec 3.4.1, Keysight 34970A data acquisition unit operates the 3-way magnetic valve, measures conductance of each sensitive layers and the resistance of Pt-temperature sensor of both SA#1 and SA#2 as well as records the pH value. The corresponding triangular heating voltage for SA#1 and SA#2is generated by the DACs of the same data acquisition unit for temperature cycling of both the MOG arrays.

3.5.3. Measurement software development

The measurement setup as represented schematically in Fig. 27a and Fig. 30a were operated by a control software developed using a LabView-software from National Instruments. This software was developed for interfacing and controlling the measurement instruments, for online visualisation and monitoring of the measurement data, and for logging of the measurement data in a text file for further analysis.

The control program directly communicates with a Keysight 34970A data acquisition unit and MFCs via serial communication. Keysight 34970A was complemented by a 34901A, 20 channel multiplexer module and a 34907A multifunction module (DIO/Totalize/DAC). Former is used for multiplexing the resistance measurements of the four MO-layers and of the temperature sensor of both sensor arrays (SA#1 and SA#2) and of pH, whereas latter one is used for generating two heating voltages from two DAC output terminals and for switching the magnetic valve using DIO terminal.

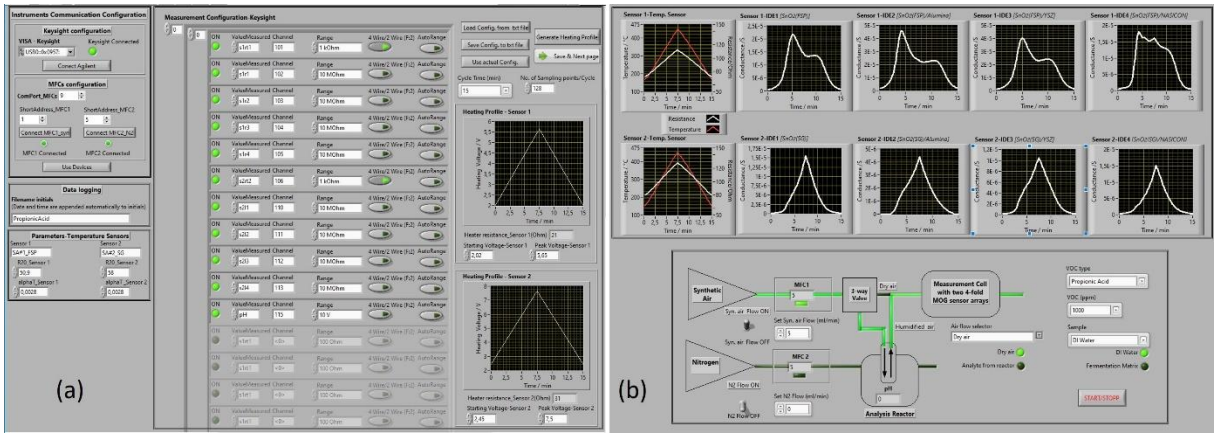

Fig. 31: Front panel display of the self-developed control program showing (a) the configuration panel, and (b) the measurement panel.

Features are incorporated in the front panel (Fig. 31) to enhance the user-friendliness. As the program starts the following settings and parameters are defined in the configuration panel (Fig. 31a).

- Communication channels for Keysight multimeter and MFCs
- Measurement configurations of individual channels in Keysight 34901A multiplexer for sensor signal measurement.
- Starting and peak voltage of triangular heating profile for each sensor array
- Duration of a temperature cycle
- Number of sampling points per temperature cycle for sensor signal measurement
- Parameters for temperature calculation from actual resistance value of on-chip temperature sensor
- Filename for data logging

Once the parameters and configurations are defined, the program switches to the measurement panel (Fig. 31b) which consists of the following element:

- Setting the flow rates of synthetic air and N_2.
- Control element for operating 3-way magnetic valve which allows selection of dry air or humidified air (Fig. 27 and Fig. 30).
- Selectors for defining and logging the actual measurement conditions, such as VOC-type, VOC-concentration, and sample-type.
- Automated graph visualising the actual CTP of all the eight MO-layers (four MO-layers from each sensor array) and temperature profile of both the sensor arrays in actual measurement cycle.
- Control button for starting and terminating the measurement.

3.5.4. Gas sensing tests with fermentation sample

Motivated by substantial changes of the fermentation sample behaviour with pH, which had been observed by different CTPs dependent on pH and even by a considerable gas development with pH-change as already observed in preliminary experiments (Appendix 5-7), a detailed investigation/correlation with the CTPs was started. The measurement sequence over time is given in Fig. 32. The whole experimental sequence can be divided into three different phases. The first phase is sample pre-conditioning (0-1.75 h) in which 1 l of the fermentation sample (now called analysis sample, Sec. 3.5.1) was transferred to the analysis-reactor. The initial pH of the sample (about 6.7) was shifted to an alkaline value (pH 8) by dosage of potassium hydroxide (5.34M KOH) and, subsequently, all gaseous components dissolved were purged out by a N_2-flow (500 ml/ min) for 45 min. During the whole sample pre-conditioning phase, the sensor arrays were exposed to dry synthetic air (5 ml/min).

In the second phase (1.75-25 h) gaseous analyte is continuously extracted from the analysis sample using the CGP with constant carrier gas flow (5 ml/min). In this situation, the 3-way magnetic valve (Fig. 30) was adjusted at position 2 and the analyte is led to the sensor arrays for analysis. As illustrated in Fig. 32b, in this phase of experiment, the sensor signals were recorded chronologically at different pH values of the analysis sample (pH 8 → pH 5 → pH 3.85 → pH 3). Decrease of the pH in steps was achieved by dosage of phosphoric acid (8.67M H_3PO_4) and checked by a pH-sensor (Sec. 3.4.1).

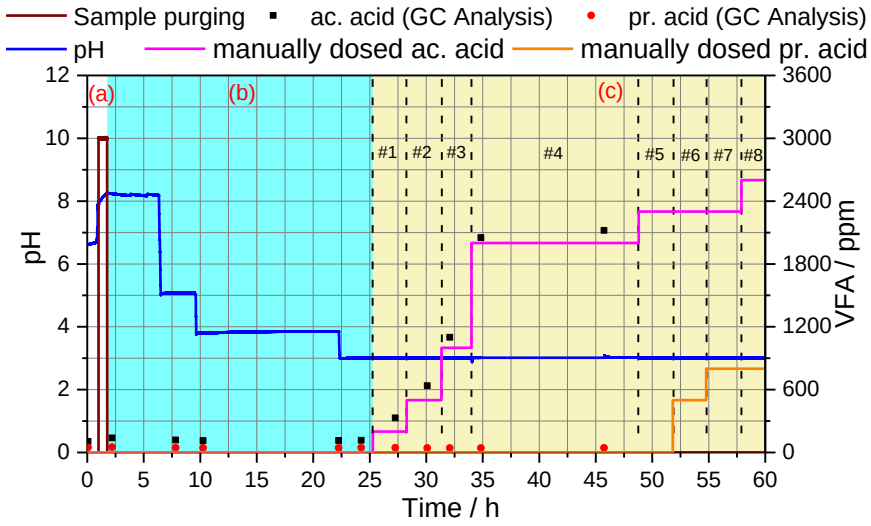

#1	200 ppm acetic acid
#2	500 ppm acetic acid
#3	1000 ppm acetic acid
#4	2000ppm acetic acid
#5	2300ppm acetic acid
#6	2300ppm acetic acid + 500ppm propionic acid
#7	2300ppm acetic acid + 800ppm propionic acid
#8	2600ppm acetic acid + 800ppm propionic acid

Fig. 32: Measurement sequence over time. (a) Sample pre-conditioning, (b) course of pH-change in steps. (c) Steps of acetic/propionic acid dosage over time at pH 3.

Similarly, in the third phase (25-34h, Fig. 32c), sensor signals were recorded at pH 3 condition after manual dosage of different volumes of acetic and propionic acids, which correspond to concentrations as indicated, all related to the original state (composition) of the fermentation sample at pH 3 condition.

3.5.5. Method of gas analysis referencing

For correlation of the CTP signals as recorded from the two sensors arrays SA#1 and SA#2 when exposed to different gas conditions in general and the CTP changes measured with change of pH of the analyte in particular, reliable classical gas analysis methods were necessary for referencing purposes. Simultaneous FTIR analysis of the analyte was preferred for this purpose by use of a flow through setup because it allows continuous gas analysis simultaneous to the CTPs of the different sensitive layers recorded. In addition to FTIR analysis, batch-wise analysis of individual samples extracted at every pH-state, was made by GC analysis.

i. FTIR-analysis

For the analysis of the analyte extracted via the CGP, a TENSOR II FTIR Spectrometer (Brucker Optik GmbH, Germany) was operated simultaneously to CTPs measurements (Sec. 3.5.2). To optimize sensitivity of the FTIR spectra a, special optical flow-through measurement cell with length and open diameter optimized with respect to the optical conditions of the instrument was constructed and installed in the setup as visualized in Fig. 33a. This measurement cell, complemented by two KBr windows on either side, ensured that the analyte flow through the measurement cell in a maximum optical path-length given by the spacing of the measurement chamber and helped to adapt the cell volume to the low flow rate (5 ml/min) of the analyte extracted by CGP.

With this setup, two FTIR gas analysis procedures were investigated. (i) For simultaneous CTP sampling and FTIR-analysis, the analyte gas from the CGP was first led into the sensor cell and then to the optical flow-through cell of the FTIR (Fig. 33b). This method provides direct, i.e. simultaneous correlation of the CTPs recorded with the FTIR-spectra. However, the sensitivity achieved, suffers on non-negligible gas consumption by the two MOG array.

In order to achieve some further correlations of the CTP-changes observed with respect to the composition of the gas released especially at pH-transition from 8 to 5 (Sec.4.4.1), separate experiments were conducted with the remaining fermentation sample (1 l) (Sec. 3.5.1) by

repetition of the same experimental protocol for sample treatment (Fig. 32). However, these experiments were done without GC analysis and without exposure of the MOG arrays to these gases released by the fermentation process.

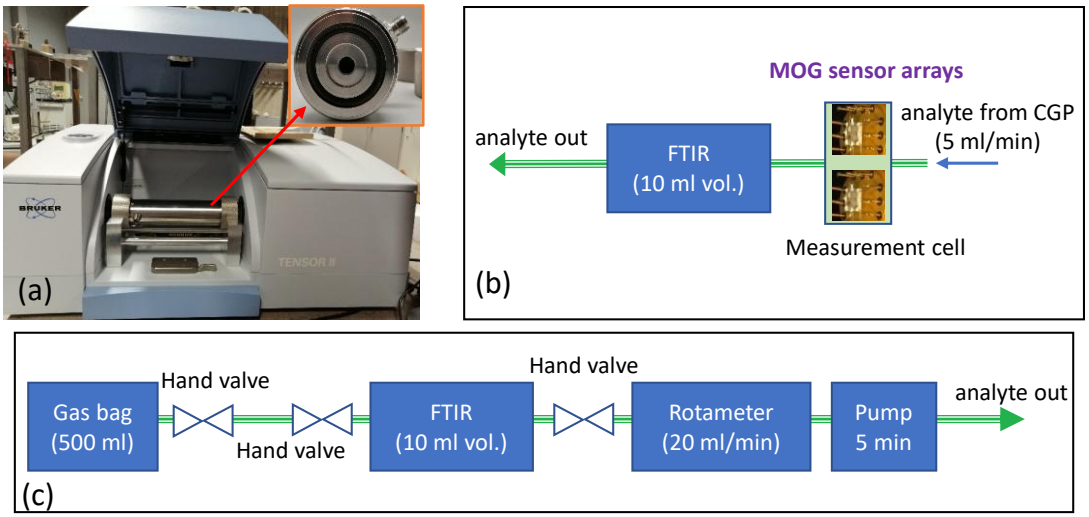

Fig. 33: Alternative FTIR analysis setup: (a)Tensor II FTIR Spectrometer with modified measurement cell (length: 200 mm, diameter: 10 mm and volume: 10 ml). (b) Scheme of the arrangement for online FTIR analysis. (c) Arrangement of offline FTIR analysis of gaseous samples collected in a gas bag. Adapted from [117].

In this experiment, clearly better analysis results with respect to the sensitivity of the FTIR-absorption bands were achieved by (ii) collection of the analyte gas from the headspace (Fig. 30a) in a gas bag with the help of a 3-way hand valve (Fig. 30a) and offline FTIR analysis afterwards (Fig. 33c). The gas collected in the gas bag was guided to the FTIR measurement cell (volume: 10 ml, Fig. 33a) at constant flow rate of 20 ml/min with the help of a pump and a rotameter. After complete purging of the residual gas component in the measurement cell over 5 min, the hand valves at either side of the measurement cell (Fig. 33c) were simultaneously closed for subsequent FTIR offline analysis.

ii. GC-Analysis

For additional offline analytical referencing at different sample condition as indicated in Fig. 32, 20 ml of the fermentation samples were extracted, centrifuged at 3000 rpm for 5 min and then stored in a freezer. The concentration of acetic acid, propionic acid, byutric acid and isobyutric acid of these samples was analyzed using a gas chromatograph (GC-456 Scion Instruments). Prior to the GC analysis the samples were centrifuged at 10400 rpm at 8°C to get particle free analytes.

4. RESULTS AND DISCUSSION

4.1. Characterization of SnO_2 and NASICON powder

The XRD diffractograms of SG prepared pure SnO_2 powder i.e. SnO_2(SG) powder, calcinated at 80 °C and 450 °C are shown in Fig. 34. The diffraction peaks are indicated in accordance with the rutile structure of SnO_2 as reported in different literature [41, 143]. Similarly, Fig. 35 shows the XRD diffractogram of SnO_2(FSP) powder.

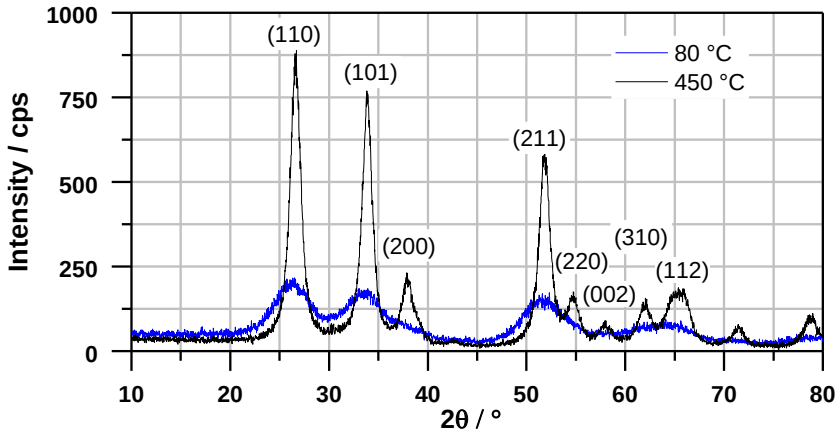

Fig. 34: XRD diffractograms of SnO_2(SG) powder calcinated at 80°C and 450°C. Data pre-published in [63].

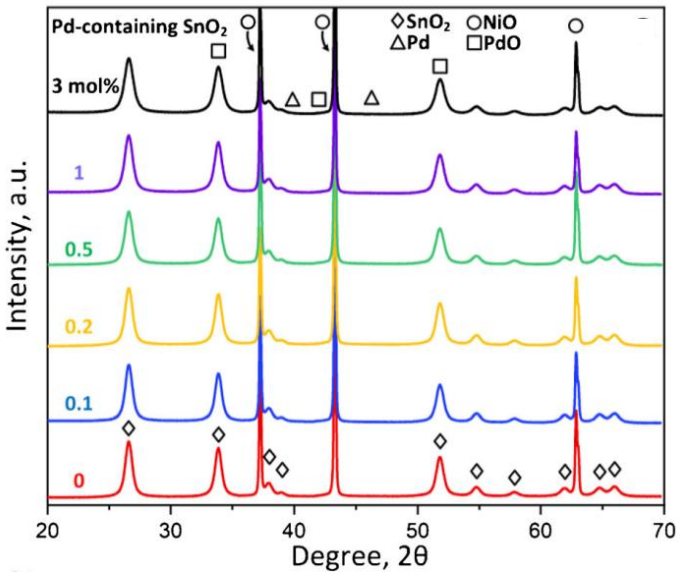

Fig. 35: XRD diffractograms of pure SnO_2 powder and Pd-containing SnO_2 powders prepared using FSP technique. Note that NiO (circles) was admixed as internal standard for pattern alignment. Here, the red pattern represents the XRD diffractogram of SnO_2(FSP) powder used in this work. Whereas blue, yellow, green, violet, and black pattern represent the XRD diffractogram of 0.1, 0.2, 0.5, 1 and 3 mol % Pd-containing SnO_2(FSP), respectively. Adapted from [133].

The XRD diffractograms of NASICON powder sintered at 800°C for 2 h, at 900°C for 3 h and at 1000°C for 4 h successively are shown in Fig. 36. The NASICON-structure was clearly indicated [148]. With increasing sintering temperature, the reflections became sharper, i.e. crystallization proceeded, but all XRD diffractograms reveal some ZrO_2 impurity phase as also observed in several studies in the past [136, 149].

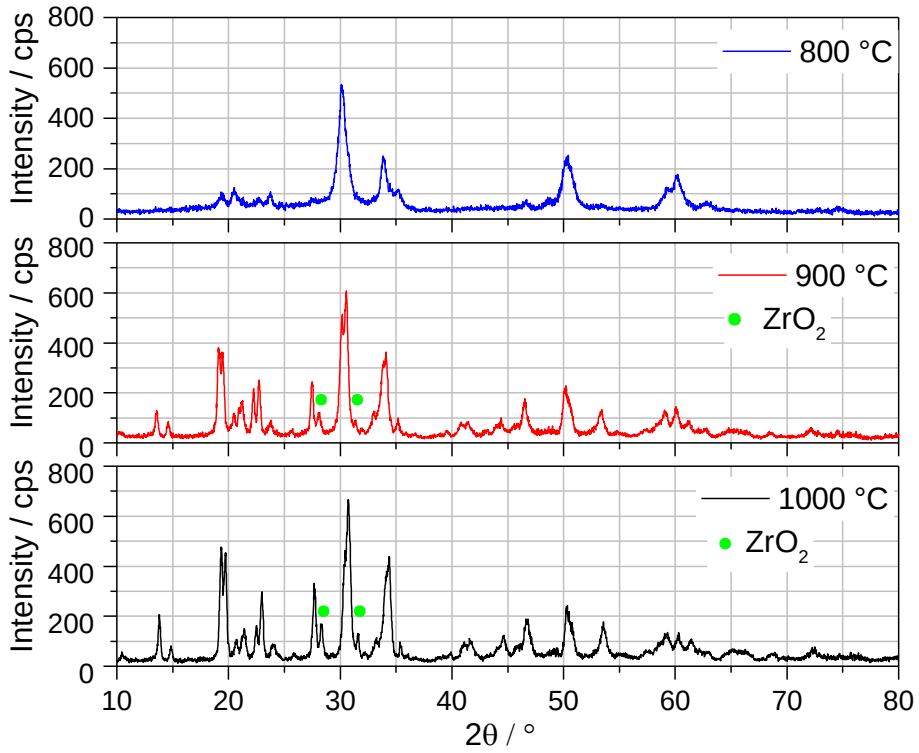

Fig. 36: XRD diffractograms of NASICON (x=2) powder sintered at different temperatures (800°C, 900°C and 1000°C). The small reflections marked by green dots indicate a small amount of ZrO_2 as a second phase. Data pre-published in [63].

.

4.2. Morphological properties of different SnO_2/additive-composites

Using ESEM and EDS analysis techniques, the morphological properties, and the distribution of the individual additive grains around the SnO_2 matrix of sintered SnO_2/additive-layers were studied.

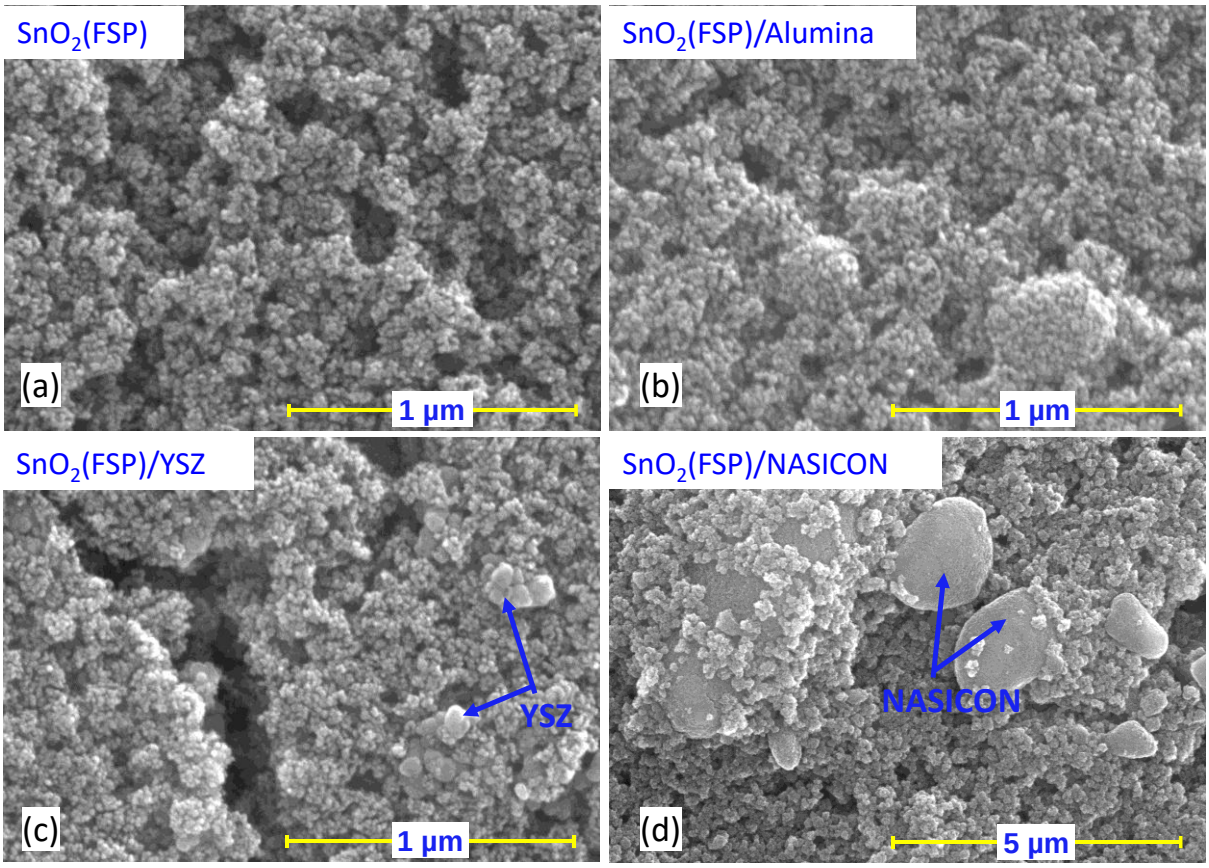

Fig. 37: ESEM images of different SnO_2(FSP)/additive gas sensitive layers. (a) SnO_2(FSP) (b) SnO_2(FSP)/Alumina (c) SnO_2(FSP)/YSZ and (d) SnO_2(FSP)/NASICON. Adapted from [63].

Prior to the ESEM and EDS analysis, the sample-layers were coated with a 3 nm thick gold layer. The ESEM-images of different SnO_2(FSP)-layers are displayed in Fig. 37. The grain size of the SnO_2(FSP)-layer seems to be very homogeneous and the grain diameter is estimated to about 15 nm. Clear influence of the additives on the SnO_2 grain size is not evident. From the ESEM images and the EDS analyses (Fig. 38a-38c), it is obvious that the additive grains are not homogenously distributed in the SnO_2(FSP) matrix. This was investigated by EDS point analysis at different areas of the samples. By the EDS-spectra, the additive-grains could be rather well localized. They exhibit a wide distribution of grain size (up to about 3 µm) and are clearly larger compared to the SnO_2(FSP) grains. This is especially evident for the

SnO_2(FSP)/NASICON-layer. The NASICON-grains were confirmed by EDS analysis in Area-1 and Area-2 (Fig. 38c), which revealed strong peaks of Na, Si and Zr elements. In the SnO_2(FSP)/Alumina-layer, presence of alumina was confirmed in Area-1 and Area-2 (Fig. 38a) by high peaks of aluminium in the EDS analysis spectra. Similarly, in the SnO_2(FSP)/YSZ-layer (Fig. 38b), YSZ was localized in Area-2 and Area-3 as indicated clearly by additional peaks of Zr, Y close to the Au-peak of the EDS spectra. However, the analysis of Area-1 is different. No significant YSZ-signal (Zr and Y peak) was found.

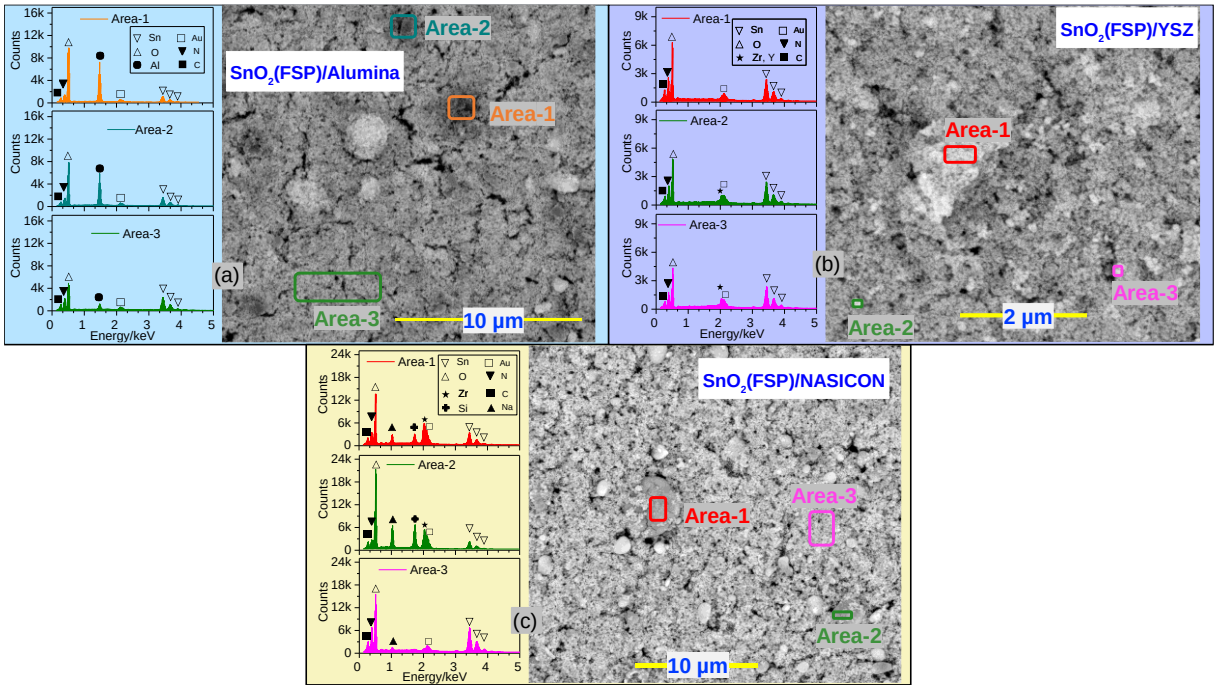

Fig. 38: ESEM images recorded using backward scattered electron analysis and corresponding spectra of EDS point analysis taken at different areas as indicated in the photographs, respectively. (a) SnO_2(FSP)/Alumina (b) SnO_2(FSP)/YSZ and (c) SnO_2(FSP)/NASICON. Adapted from [63].

Similarly, in Fig. 39, the morphology of SnO_2(SG)-layer and different SnO_2(SG)/additive-layers is illustrated. The SnO_2(SG) matrix consists of crystalline grains with a wide distribution of block sizes and homogenously distributed fine grains. At higher magnification (inset) the big SnO_2-blocks show a sub-structure of compactly packed nanosized particles with diameters smaller than 20 nm. This means, the size of the sub-grains is in the same range than that of the grains obtained by the FSP-route (Fig. 37). However, on the SG-route, the nano-grains seem preferably to crystallize to bigger crystalline blocks. This effect seems to be mostly pronounced in the pure SnO_2(SG)-layers but generally hindered by the FSP preparation technique. In contrast to the SnO_2(FSP)/additive-layers, in SnO_2(SG)/additive-layers, there are SnO_2 grain

blocks with size comparable to the grain size of the additives (Fig. 40). This is especially the case for the SnO_2(SG)/NASICON-layer. Again, NASICON could be clearly localized by EDS analysis (Fig. 40c) as indicated by the strong peaks of Na, Si as well as by Zr peaks observed for Area-1 (darker grain). Other brighter regions, such as Area-2 and Area-3 clearly represent the SnO_2. In case of SnO_2(SG)/Alumina layers (Fig. 40a), average grain size of tin oxide is obviously bigger than alumina as localized in Area-1 (SnO_2-grain) whereas, Area-2 and Area-3 clearly confirm the presence of alumina by strong Al peaks in the EDS spectra. Similarly, YSZ also seems to have smaller average grain size compared to SnO_2(SG) but appears to be more homogenously distributed in SnO_2(SG) matrix compared to other additives, which is confirmed by the presence of the Zr, Y- peak in EDS analysis of all three areas analysed (Fig. 40b). The difference in morphology may change the electronic interaction scenario of the additives with the SnO_2-grains and may take different influence on the gas sensing properties [38] which must be considered while interpreting the CTPs measured at exposure to different analytes.

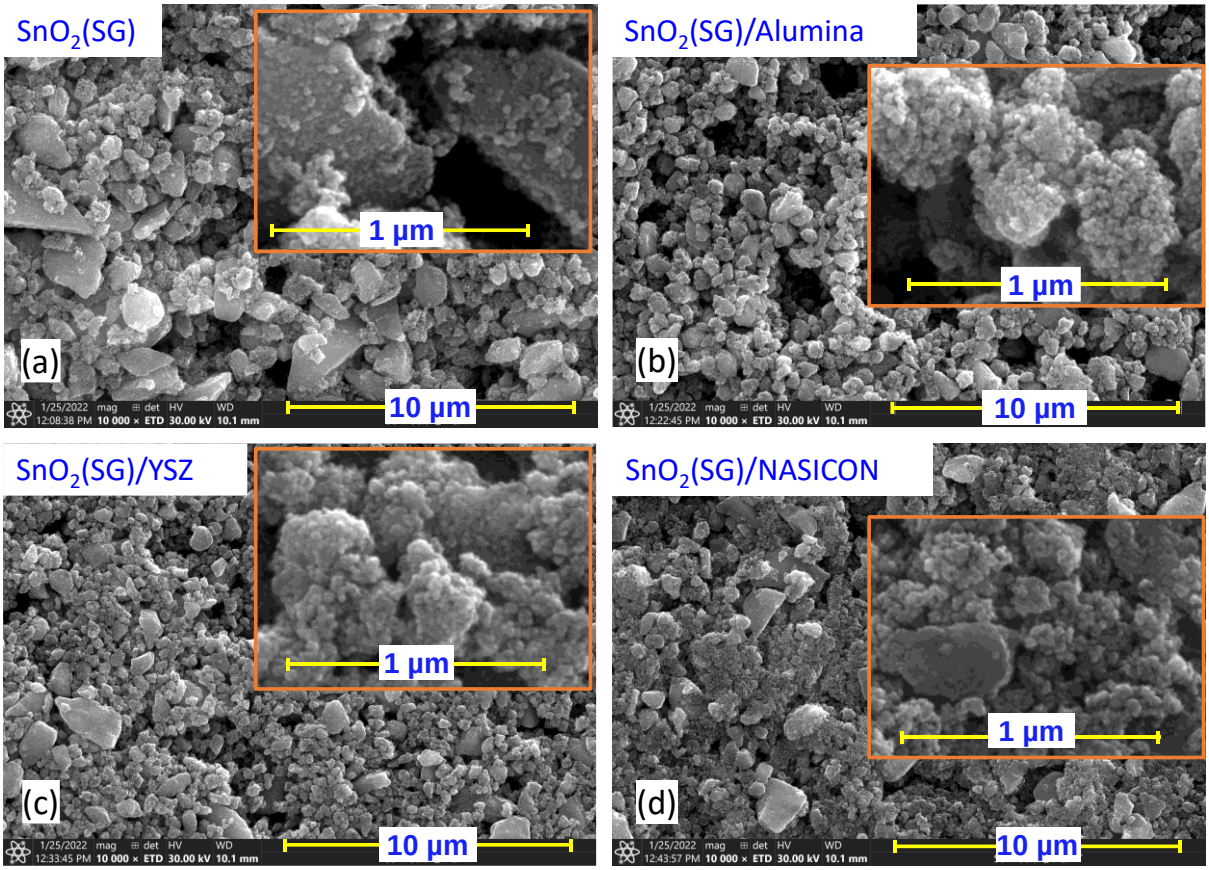

Fig. 39: ESEM images of different SnO_2(SG)/additive gas sensitive layers. (a) SnO_2(SG) (b) SnO_2(SG)/Alumina (c) SnO_2(SG)/YSZ and (d) SnO_2(SG)/NASICON. Adapted from [63].

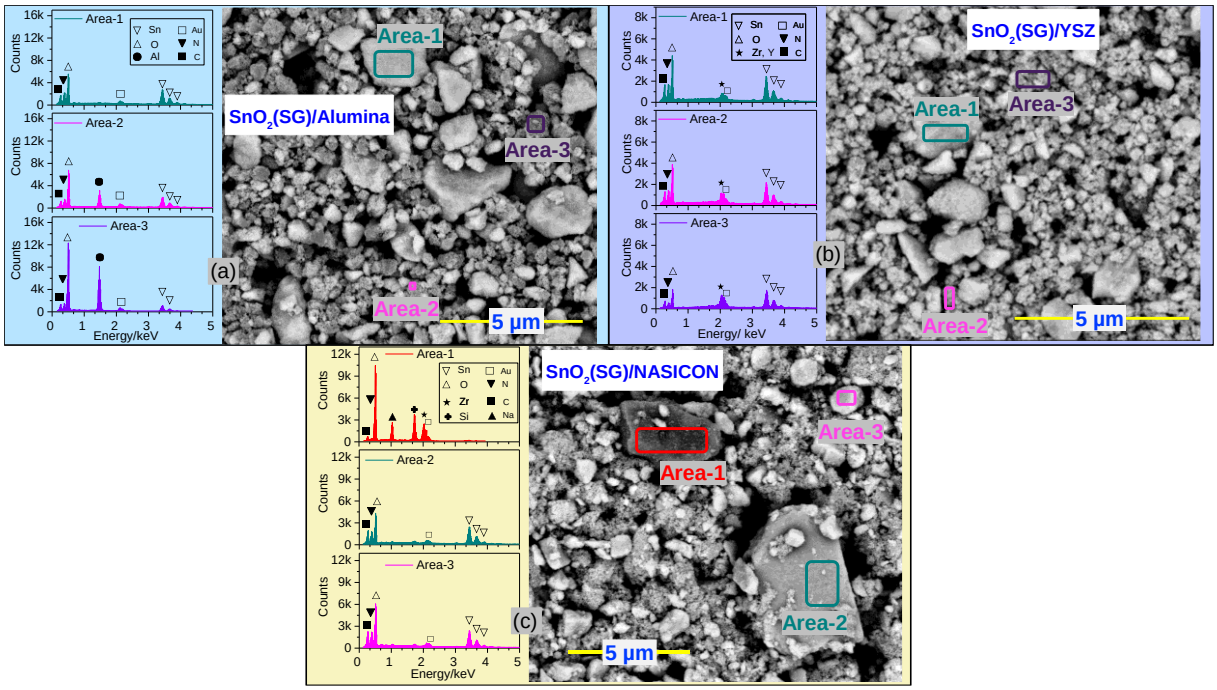

Fig. 40: ESEM images recorded using backward scattered electron analysis technique and corresponding spectra of EDS point analysis taken at different areas as indicated in the photographs, respectively. (a) SnO_2(SG)/Alumina (b) SnO_2(SG)/YSZ and (c) SnO_2(SG)/NASICON. Adapted from [63].

The topographic image and the average thickness profiles of individual sensitive layers sampled with a confocal microscope are illustrated in Fig. 41. The thickness of the layers is not measured homogeneous. Moreover, each layer shows a laterally different thickness profile and, as desired in case of SA#3 (Fig. 41a), varies in absolute thickness. Furthermore, the SnO_2(FSP)/additive-layers (SA#1, Fig. 41b) are typically prepared clearly thinner than the SnO_2(SG)/additive-layers (SA#2, Fig. 41c). This must be considered when comparing the CTPs and response behaviours of FSP and SG prepared layers.

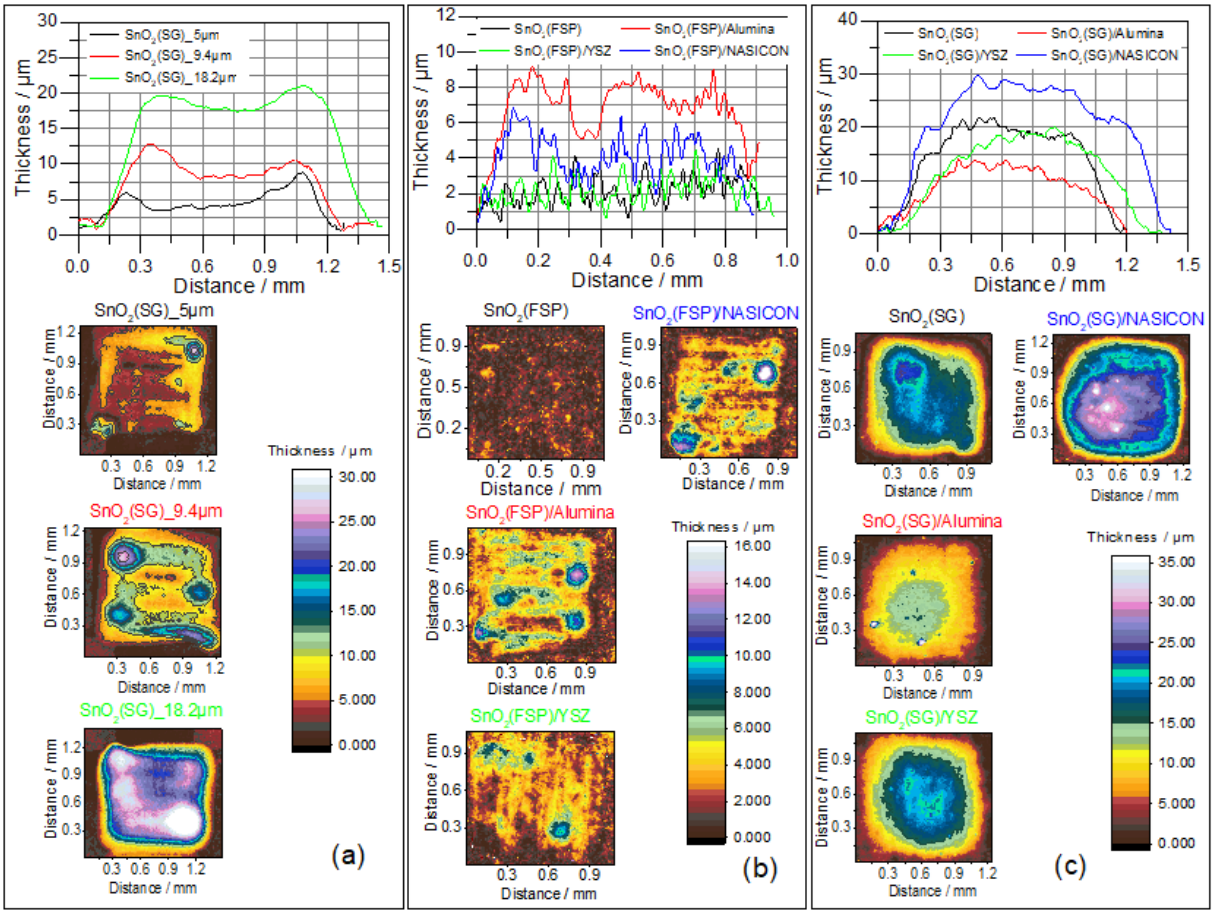

Fig. 41: Topographic images and average line thickness profiles of (a) SnO_2(SG)-layers with different thickness (SA#3) (b) SnO_2(FSP)/additive-layers (SA#1) and (c) SnO_2(SG)/additive-layers (SA#2). Data pre-published in [63].

4.3. Gas sensing tests with model VOCs

4.3.1. Studies to optimize measurement conditions

First the sensing conditions with respect to carrier gas flow and the temperature cycling period had to be optimized before the performance of the analysis system could be investigated. As an example, Fig. 42a shows the CTP profiles of a SnO_2(FSP)/1%Pd-layer operated at a cycling period of 3 min at different carrier gas flow rates when 4% acetic acid was dissolved in DI water at pH 3.

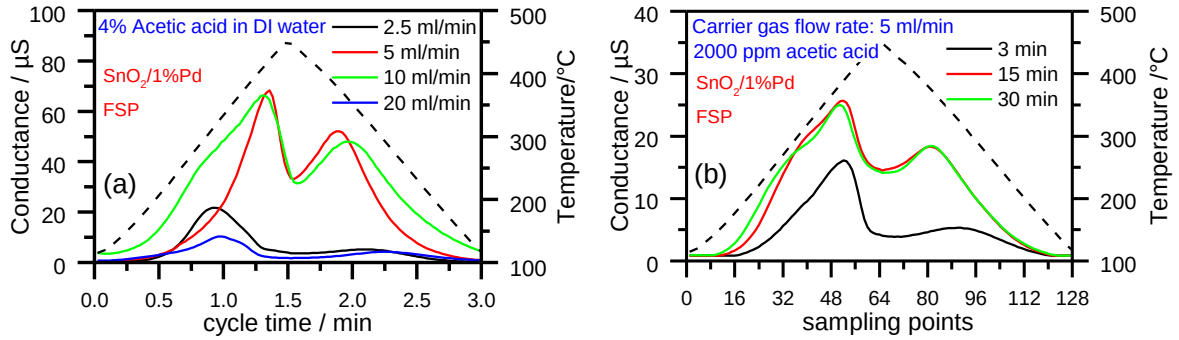

Fig. 42: CTPs of SnO_2(FSP)/1%Pd-layer when exposed to (a) 4% acetic acid at different carrier gas flow rate and (b) 2000 ppm acetic acid (both dissolved in DI water) at different cycle time. Data pre-published in [63].

The absolute conductance of the CTPs is lowest for 20 ml/min flow with a characteristic peak at around 335°C (at 1 min). At a flow rate of 10 ml/min, the CTP shows clearly higher absolute conductance and a different CTP-shape. A shoulder is observed at around 290°C (0.8 min) and clear peaks at around 410°C (1.3 min) during heating phase and at around 360°C (1.97 min) during cooling phase. Further reduction of the flow rate to 5 ml/min resulted in further small increase of the absolute conductance maximum and the shoulder at heating phase is no more visible. Overall, the CTP-shape is sharper in structure and the peaks are observed at around 410°C (1.35 min) and at around 380°C (at 1.88 min). Further decrease of the flow rate to 2.5 ml/min resulted in a clearly lower absolute conductance with reduced CTP-features. This phenomenon can be explained as following based on the theoretical description given in Sec. 2.4: The relative concentration of analyte in the carrier gas reaching the MOG arrays is dependent on the contact time of the carrier gas with the gas permeable membrane. Longer the contact time between the carrier gas and the gas permeable membrane, the higher is the relative concentration of analyte in the carrier gas transported to the MOG arrays for analysis. Thus, the relative concentration of analyte would reach a maximum at thermodynamic equilibrium, i.e.

when the carrier gas flow rate is zero. However, this would mean that no analyte is transported to the MOG arrays. Additionally, the lower carrier gas flow rate ensures a longer contact time between the carrier gas loaded with analyte and the gas-sensitive layers as it flows through the measurement cell.

On the other hand, the porous SnO_2 layer can be considered as a collection of stacked chemical reactors in which incoming analyte diffuses sequentially through each reactor. Throughout the process, every reactor consumes a fraction of incoming analyte for the gas sensing reaction, i.e. the reaction with adsorbed oxygen states (eq. (27)). When the carrier gas flow rate is low (in this case, 2.5 ml/min), the transported analyte may get totally consumed in the preceding reactors, potentially limiting the participation of all reactors in the gas sensing process. Consequently, this may lead to lower absolute conductance and less pronounced CTP-features. Thus, to maximise the sensitivity of the gas-sensitive layers, an optimal carrier gas flow rate must be set. This is of general importance for detection of low analyte concentrations dissolved in the aqueous phase. From these results, it was clear that the flow rate between 10 ml/min and 5 ml/min flow rate had to be chosen. However, these measurements were made for 4% acetic acid dissolved in DI water which is much higher than practical requirements considering the measurements of dissolved organic acids in fermentation processes. In all the upcoming experiments, the CGP was operated at a flow rate of 5 ml/min to enable elongated contact of the carrier gas with the gas-sensitive layers.

At 5 ml/min carrier gas flow rate, the influence of the temperature cycling period on the CTP-integral and shape had to be further investigated. In Fig. 42b, CTP profiles of SnO_2(FSP)/1%Pd-layer operated at different cycle times while exposed to 2000 ppm acetic acid dissolved in DI water are given vs. the sampling points, Sp (total sampling points in a cycle =128). This allows the comparison of the resulting CTP-features on a common time-base. The CTPs show clearly different absolute conductance and CTP-features depending on the temperature rate. For 3 min temperature cycle, the absolute conductance is the lowest with characteristic peak at around 388°C (Sp=51) and at around 325°C (Sp=90). With increased temperature cycling period to 15 min and 30 min, an additional shoulder is observed while heating and the peak while cooling becomes sharper and is shifted to around 380°C (Sp=80). Comparing CTPs for 15 min and 30 min temperature cycle, there is no difference in absolute conductance as well as in CTP-features while cooling. However, while heating, CTP-shape is broader, and the profile shoulder is a little bit better visible for the 30 min temperature cycle compared to the profile for 15 min

temperature cycle. But the differences are not substantial, therefore the 15 min temperature cycle is used in all forthcoming measurements.

4.3.2. Influence of the layer thickness on the CTP-shape

The CTPs of SnO_2(SG)-layers of SA#3 with average thickness of 5 µm, 9.4 µm and 18.2 µm, respectively (Fig. 41a) at exposure to 2000 ppm acetic acid are visualized in Fig. 43a. Despite of the differences in the absolute thickness and conductance change, mainly in the heating phase of the cycle, the specific conductance peaks occurring with temperature are well reproducible (no peak shift) in all the layers, while the relative peak height is different for different layers. This result indicates that the reactions of the target gas with the adsorbed oxygen states (Sec. 2.1.2) are the same in all the layers, but with different rates and measured at different geometries.

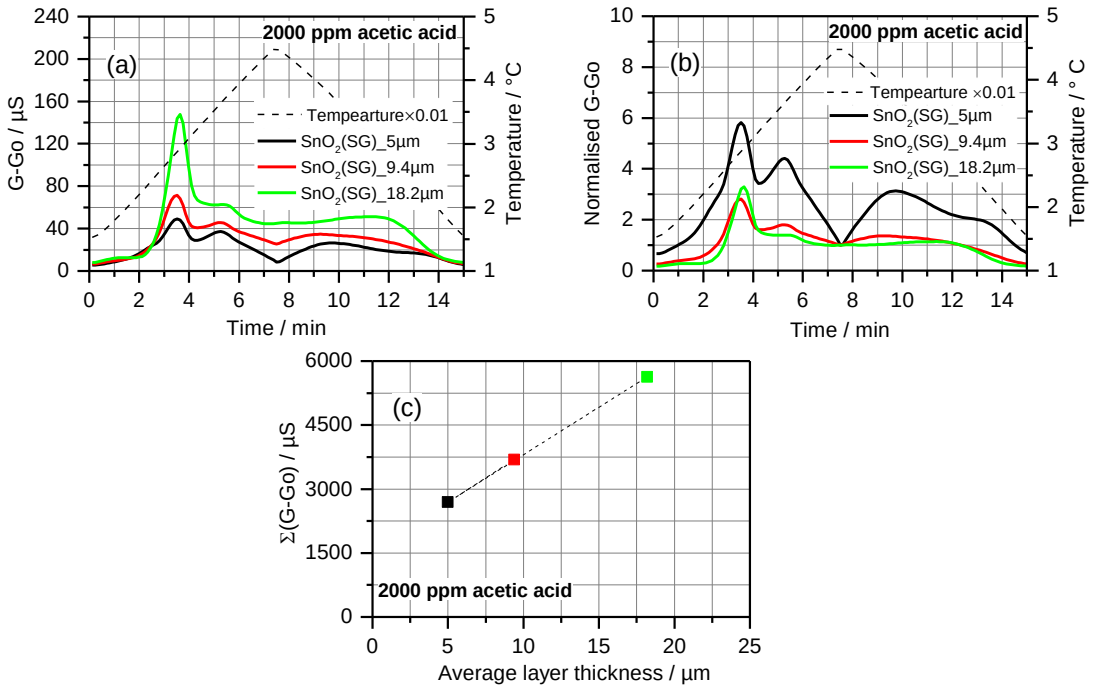

Fig. 43: Response of SnO_2(SG)-layers (SA#3) with different thickness (5 µm, 9.4 µm, and 18.2 µm). (a) CTPs given as (G-Go) values. Go is Go(hum. air) i.e. the CTP measured in DI water at pH 7. G is the CTP response measured in presence of the 2000 ppm acetic acid dissolved in DI water at pH 3. (b) Normalised (G-Go) response. Normalisation is made by the (G-Go) value at the maximum temperature of temperature cycle. (c) CTP-integrals vs. layer thickness. Data pre-published in [63].

As discussed in Sec. 2.3.1, a porous thick film tin oxide layer covering the (underlying) Pt-IDE has to be considered as a chemical reactor with different reaction zones from the top to the

metal electrode microstructured on the substrate (outer geometrical surface, inner pore surface and electrode-MO interface, see illustration in Fig. 15), which all provide different (catalytical) reaction conditions. Thus, different (electric) contributions to the overall sensing behaviour must be considered, measured as a change of resistance between the IDE-fingers. Recalling the discussion from Sec. 2.3.1, as the gas diffuses through the tin oxide layer, a fraction of incident gas is consumed by each of the reaction zones and therefore the fraction of the target gas molecules reaching the lowest zone (electrode-MO interface) depends on the diffusion and reaction conditions (kind of additive, layer porosity and temperature). In other words, depending on the temperature of the sensitive layer, the layer thickness and its morphology, an effective concentration profile of the reactive gas components in the layer may be formed by which the distribution of sensitivity contributions over the layer thickness is given, which determines the overall sensitivity measured. Of course, this is only an idealized model of the real situation. As shown in Fig. 41, the thickness over a layer is not constant and the edge-effects are also not considered in this crude description. In addition, as discussed in Sec. 2.3.3, in case of thermo-cyclically operated tin oxide sensors, if the temperature change (typically) is not slow enough to reach steady state reaction situations, non-steady state situations in the different chemical reaction zones must be considered. This means, each reaction zone is exposed to a different target gas concentration at a time and, probably, different adsorbed oxygen surface state concentration resulting in different individual responses of the reaction zone.

Despite these rather complicated reaction conditions, the CTP-integral vs. layer thickness seems to be roughly linear (Fig. 43c) and increases with layer thickness. The normalised CTPs (Fig. 43b) clearly illustrate that in opposite to the absolute response, the normalised response is measured highest on the thinnest layer (5µm). These results are in good agreement with the results reported in [101], where the response of thermo-cyclically operated SnO_2 sensors to CO were found to be linearly dependent to layer thickness. In case of isothermally operated SnO_2 sensors, the increase of the sensor response with layer thickness has been explained [150] by Becker et al using a simple diffusion-reaction model. The authors argued that due to diffusional warming caused by the collisions with walls of the pores, fraction of incident gas diffusing further in the thicker, porous layers reaches electrode-MO interface in vibrationally excited state. Consequently, in this excited state the activation energies for the sensing reaction are easily overcome compared to reaction in thinner layers where such heating effects are less pronounced.

However, increasing the layer thickness does not always result in the increased response. For isothermally operated thick film SnO_2 sensors, sensor response would reach maximum at certain thickness and then decreases with further increase of the layer thickness [151]. This may be also the consequence of the limited spreading of the electric field lines as illustrated crudely in Fig. 15. From these results, it may be concluded that the sensitivity of the FSP-layers of SA#1 (Fig. 41b), which are clearly thinner compared to corresponding layers in SA#2, would be even higher than measured (Sec. 4.3) if the layers could have been fabricated thicker.

4.3.3. CTPs of SnO_2(FSP)/additives (SA#1) and SnO_2(SG)/additives (SA#2)

i. Influence of humidity on CTPs

As mentioned in Sec. 3.4.4, both sensor arrays SA#1 and SA#2 (Fig. 24d and Fig. 24e) were first aged in dry synthetic air (5 ml/min) before making measurements with dissolved VOCs in DI water.

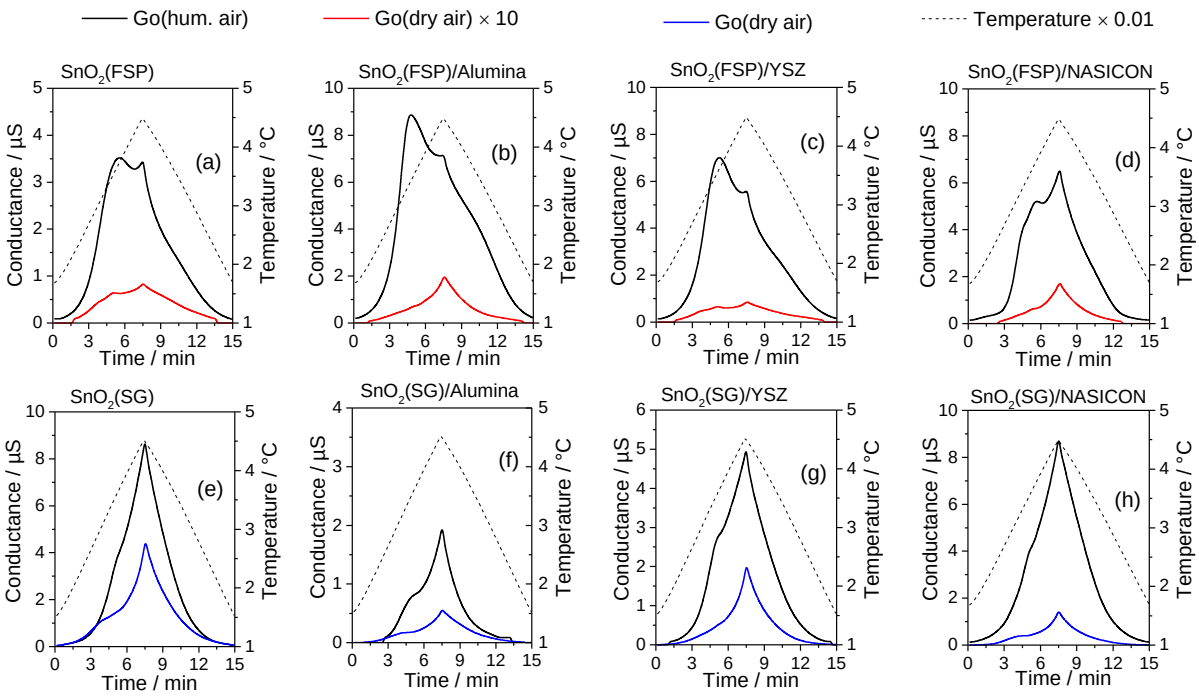

Fig. 44: CTPs of different (a)-(d) SnO_2(FSP)/additive-layers in SA#1 and (e)-(h) SnO_2(SG)/additive-layers in SA#2 measured for dry synthetic air, Go(dry air), and for humidified air, Go(hum. air), as extracted by the CGP in DI water at pH 7 prior to the exposure to model VOCs.

As an example, in Fig. 44, the CTPs measured for dry synthetic air, Go(dry air), at the end of the aging process are illustrated together with the CTPs measured for DI water at pH 7, Go(hum.

air), as sampled with the CGP prior to the exposure to the model VOCs. The CTP-features (shoulder) observed in Go(dry air), in some layers mainly represent the residual humidity (about 2 ppm) in synthetic air. The clear differences observed in the CTPs measured in humidified air, Go(hum. air), related to those measured in dry air, Go(dry air), demonstrate the considerable influence of humidity on the CTPs by donation of electrons to the conductance band according to eq. (20) as introduced in Sec.2.3. In general, the FSP-layers show clearly higher sensitivity to humidity in comparison to SG-layers (Fig. 44).

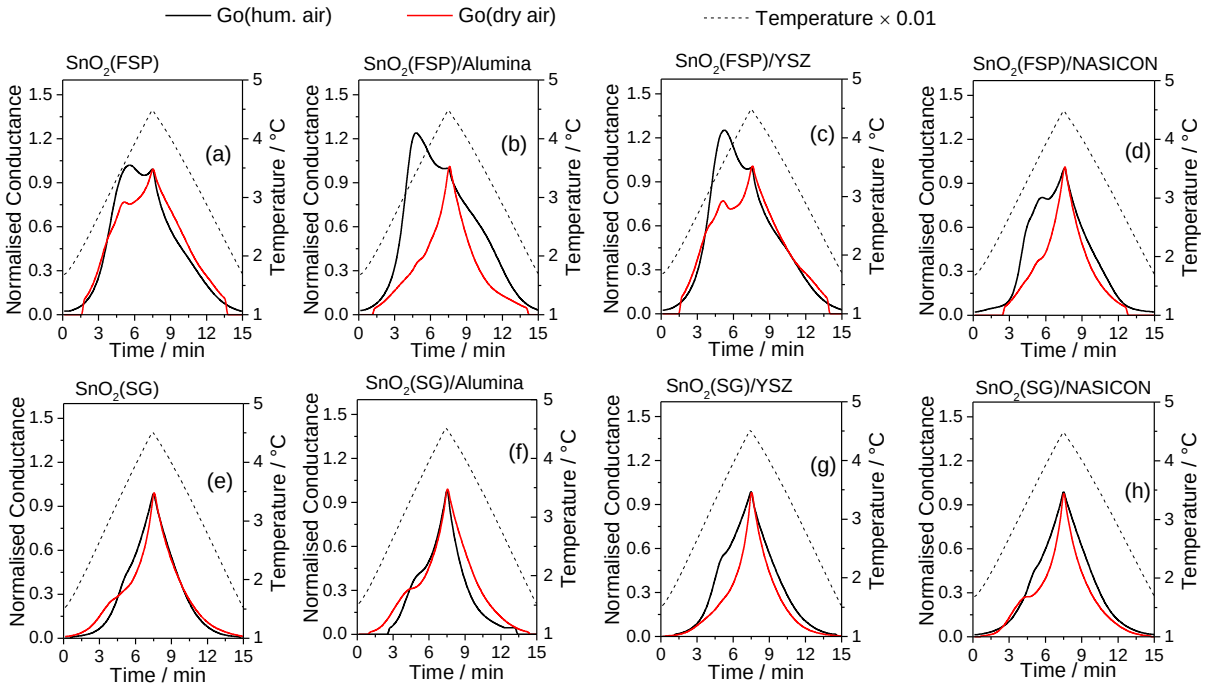

Fig. 45: Normalised CTPs) of different (a)-(d) SnO_2(FSP)/additive-layers in SA#1 and (e)-(h) SnO_2(SG)/additive-layers in SA#2 measured for dry synthetic air, Go(dry air), and for humidified air, Go(hum. air), as extracted by the CGP in DI water at pH 7 prior to the exposure to model VOCs. Normalisation is made by the conductance value at the maximum temperature of temperature cycle.

With regard to the CTP-shapes measured for humidified air, Go(hum. air), it is clearly illustrated by the normalised representation (Fig. 45) that the features representing the humidity, for example, peaks are much more pronounced in the CTP of FSP-layers related to those of the SG-layers. In latter, typically only small deviations from the Go(dry air)-plot (shoulders) are observed.

ii. CTPs of four different VOCs dissolved in DI water

As already introduced in Sec. 3.4.4, the concentration ranges of the VOCs chosen for investigation of the sensor responses for each analyte had to be individually set due to their specific Henry constants to enable comparable concentrations in the gas phase. The resulting CTPs as recorded for eight different sensitive layers (columns) when exposed to various concentrations of different VOCs (given in ppm by volume in DI water) like acetic acid, propionic acid, ethanol, and acetone (rows) are visualized as (G-Go) values in Fig. 46. Obviously, the SnO_2 morphology, the additives, and, of course, the analyte gas species take clear influence on the CTP-shapes. The concentration of the analyte is well reflected in the CTP-integral, which could be used for quantitative chemical analysis [107, 119], as already reported in former investigations [41]. This means, the individual surface reactions of the gas components on different sensitive layers are observed as VOC specific CTP-features, which are further illustrated in a normalised representation as shown in Fig. 47.

The overview in Fig. 46 illustrates a clear trend. The FSP-layers show specific and well pronounced CTP-shapes with the individual gas component but dependent on the kind of additive. The SG-layers also show those individual characteristic features, but they are comparatively less pronounced. This can be, for instance, very well demonstrated, if the CTPs of SnO_2(FSP)/Al_2O_3-layer are compared with those of SnO_2(SG)/Al_2O_3-layer for all four analytes investigated. The individuality of the CTPs dependent on the target gas, in case of the SnO_2(FSP)/Alumina-layer, is clearly illustrated for all four components (Fig. 46). The CTP-shapes of acetic and propionic acid are more similar, however, this is not surprising, because these are molecules with the same functional reaction groups.

In contradiction, the CTPs of the SnO_2(SG)/Alumina-layer sampled at exposure to propionic acid, ethanol, or acetone, i.e. of molecules with different functional reaction groups, are rather similar in shape and not very different from the shape of a CTP of a pure semiconductor vs. temperature, which is expected to be simply exponential. This means that those profiles do only to some limited extent represent individual surface reactions of the target gas with the adsorbed oxygen states at specific reaction temperatures. In addition, it is a remarkable fact that nearly all FSP-prepared layers show a clearly higher dependency to G-Go on the target gas concentrations compared to the SG-prepared layers (Fig. 46). An exception is the pure SnO_2-layer where this difference in sensitivity was only observed at propionic acid exposure.

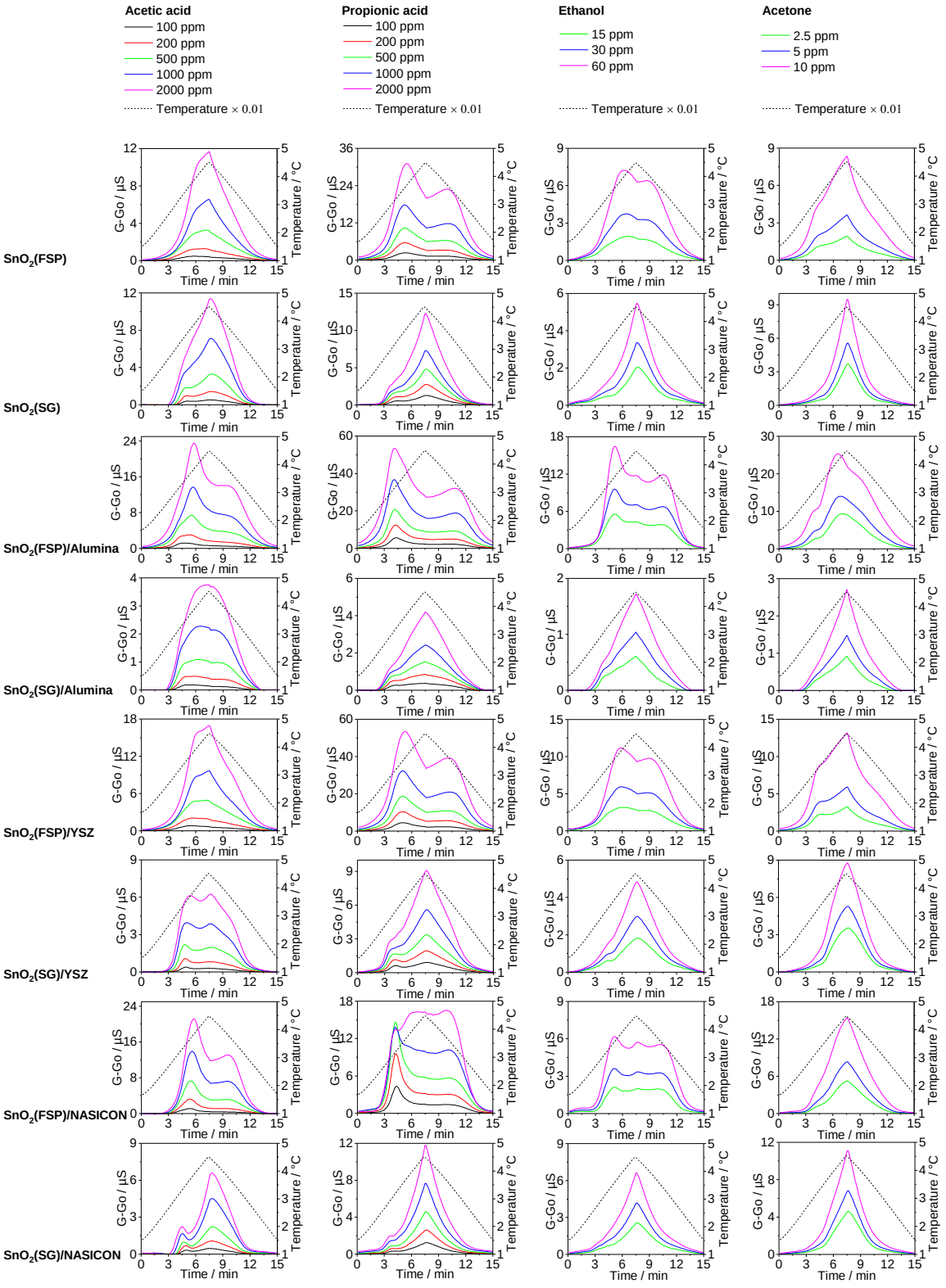

Fig. 46: Complete sensor responses of chip SA#1 and chip SA#2: CTPs given as (G-Go) values for eight different sensitive layers (in columns) measured at various concentration of different VOCs (in rows). Go is Go(hum. air) i.e. the CTP measured in DI water at pH 7. G is the CTP response measured in presence of the VOC-analyte dissolved in DI water at pH 3. Data pre-published in [63].

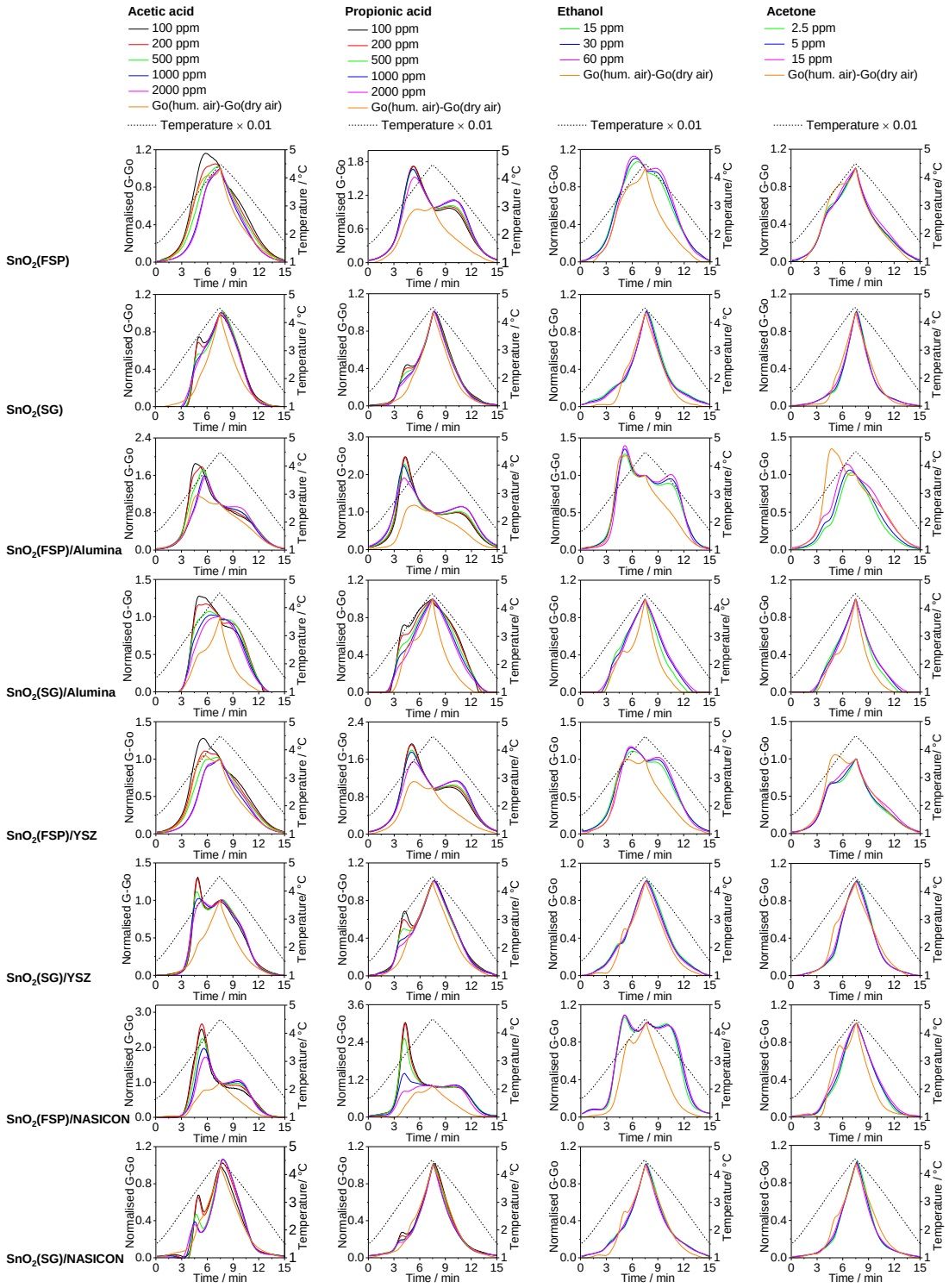

Fig. 47: Normalised G-Go plots: CTPs of eight different sensitive layers (in rows) measured for various concentrations of different VOCs (in columns). Normalisation is made by the (G-Go) value at the maximum temperature of temperature cycle. Go is Go(hum. air) i.e. the CTP measured in DI water at pH 7. G is the CTP response measured in presence of the VOC-analyte dissolved in DI water at pH 3. In addition, for every layer the influence of humidity on the CTPs is illustrated as normalised (Go(hum. air)-Go (dry air)) normalised plot. The humidity is related to water vapour saturation at 18°C. Data pre-published in [63].

The change of the CTP-shapes with gas concentration is even better illustrated by the normalised representation (Fig. 47). Obviously, the CTP-profiles are more or less constant with different concentrations of ethanol or acetone, whereas there is a clear decrease of the specific feature observed in the temperature range between about 300°C and 400°C with concentration of acetic acid as well as propionic acid. This behaviour is interpreted as an artefact. Faced to the question of relative CTP-increase with the course of a CTP over temperature, it tells us that in case of the carboxylic acids the reaction rate with the oxygen states is still increasing with both temperature, and concentration, even at the highest temperature of a cycle. For comparison, in case of ethanol and acetone, the reaction with the target gas and therefore the CTP-increase seems to be strongest at some temperature below the maximum temperature (T_{max}=450°C). This leads to the increase of the gas specific features with target gas concentration. The corresponding features in the same temperature range but in the second half of the CTP (cooling phase) are much less pronounced for all layers.

Such CTP-asymmetry is a well-known fact [41, 101], which could be qualitatively explained by the differences in actual gas adsorption situation correlated with the direction of temperature change in accordance with well-established theories of gas adsorption [152–155], as already discussed in Sec. 2.1. There are different adsorbed oxygen states ($O_{2\,ads}^-$, O_{ads}^-, O_{ads}^{2-}) formed at different temperature range. At a specific transition temperature, the type of dominating adsorbed oxygen state is dependent on the direction of temperature change. This means, while heating up, there exist adsorbates which are preferably formed at low temperature whereas, before cooling, the surface is more or less cleaned by intensive desorption at the top of the temperature-cycle resulting in less surface concentrations of the adsorbed reaction partners and therefore on less pronounced CTP-features.

iii. Individuality of CTP-shapes and correlation of sensor response with model VOCs

The individuality of the CTP-shapes at exposure to different analytes is even better illustrated if the normalised CTP-curves from Fig. 47 are plotted into a common diagram. This was done in Fig. 48, which gives an overview about the gas specific CTP-features of all the SnO_2-layer and SnO_2/additive–layers under investigation. The features of conductance-change by exposure of different target gas components are clearly different in shape, position, and height (integral) and these "T-spectra" vary considerably with the kind of additive and morphology of the SnO_2-matrix. The height (integral) of the feature related to the individual target gas component is a measure of the relative response to this specific gas component at temperatures below T_{max} in

relation to the response at T_{max}. The position of the feature in the range of cyclic temperature variation and its shape represents the individual molecular reactions which are responsible for the conductance change [106]. These differences of the CTP features related to the kind of target gas component and with respect to the individual SnO_2/additive-layer are clearly demonstrated in Fig. 48. Their peculiarity and reproducibility estimate the quality of chemical gas analysis by numerical analyses of these CTPs, as e.g. demonstrated in [106, 119].

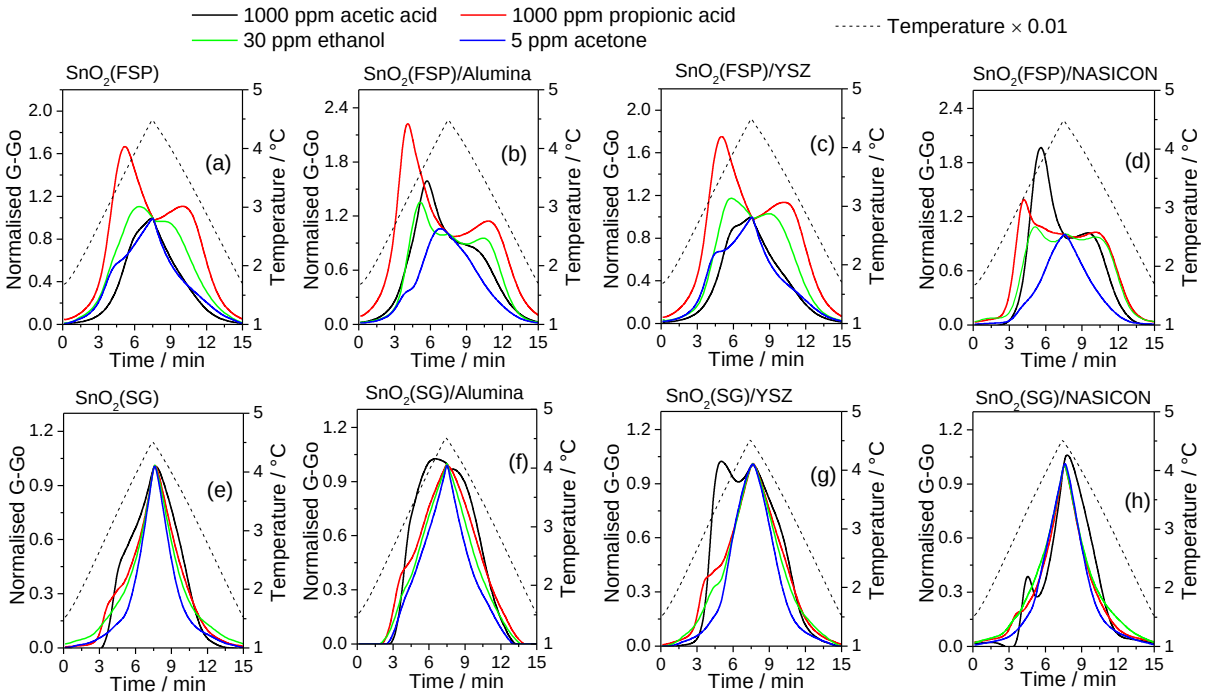

Fig. 48: Normalised gas specific CTP-features of (a) SnO_2(FSP), (b) SnO_2(FSP)/Alumina, (c) SnO_2(FSP)/YSZ, (d) SnO_2(FSP)/NASICON, (e) SnO_2(SG), (f) SnO_2(SG)/Alumina, (g) SnO_2(SG)/YSZ, (h) SnO_2(SG)/NASICON on exposure to 1000 ppm acetic acid, 1000 ppm propionic acid, 30 ppm ethanol, and 5 ppm acetone dissolved in DI water at pH 3. Normalisation is made by the (G-Go) value at the maximum temperature of temperature cycle. Data pre-published in [63].

In general, numerical analysis of the CTP of a sole layer already enables gas component analysis. The analysis quality depends mainly on the individuality of the CTP-features and on their reproducibility. Moreover, the use of a sensor array, namely simultaneous operation of different sensitive layers, provides multiple CTPs which further improves the gas identification quality by application of numerical multi-component analysis and pattern recognition methods [119]. The CTPs in Fig. 48 clearly demonstrate that the individuality of the CTP-shapes measured on the SnO_2(FSP)/additive-layers (Fig. 48a-d) related to different gas molecules is clearly better compared to the SnO_2(SG)/additive-layers (Fig. 48e-h). For example, the clear

separation of the CTP-feature (G-peak) representing propionic acid from those representing acetic acid is exhibited for all the FSP-layers (Fig. 48a-d). Correspondingly, enhanced gas analysis quality with the SnO_2(FSP)/additive-layers, for example, analysis of individual VFAs in fermentation liquids, can be expected.

iv. Comparison of sensor response to model VOCs

Although the CTPs represent reaction states at different temperatures, their integral calculated (from CTPs shown in Fig. 46) according to eq. (24) vs. VOC concentration is well fitted by a power law. As an example, the integrals and their regression curves for SnO_2(SG)/Alumina-layer and SnO_2(FSP)/Alumina-layer are shown in Fig. 49a. They clearly illustrate the higher absolute gas response $\sum$(G-Go) of the SnO_2(FSP)/Alumina-layer to acetic acid. This trend is confirmed as well by comparative measurements of the absolute gas response of the pure SnO_2-layers to propionic acid and furthermore, in the same figure it is illustrated that by admixing with YSZ- or Alumina-additive the sensitivity of the SnO_2(FSP)-layer is further enhanced (Fig. 49b). The integral vs. individual VOC (acetic acid, propionic acid, ethanol, and acetone) concentrations for all the layers of SA#1 and SA#2 is presented as matrix in Appendix 3.

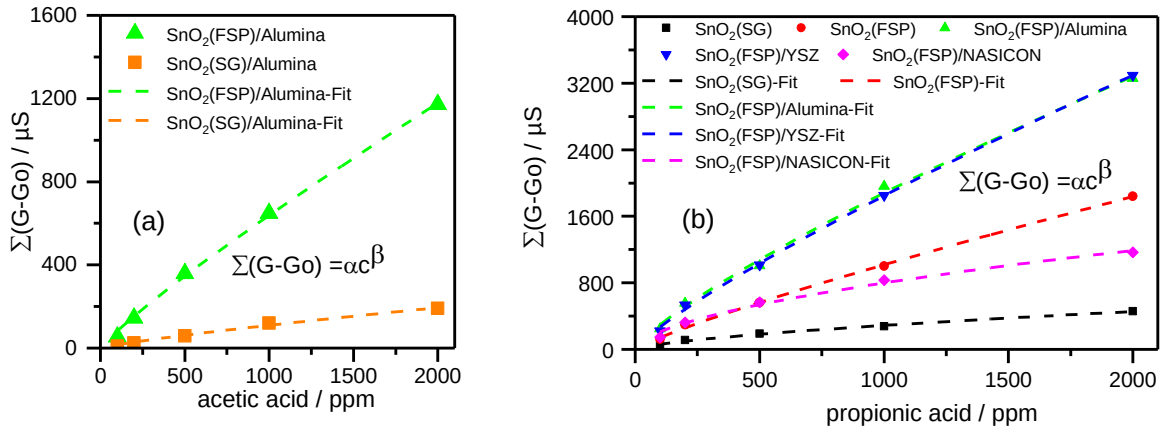

Fig. 49: CTP integral ($\sum$(G-Go)) of a) SnO_2(SG)/Alumina-layer and SnO_2(FSP)/Alumina-layer vs. concentration of acetic acid and b) of several layers vs. concentration of propionic acid. Data pre-published in [63].

As an overview, the α and β values for all studied sensitive layers are given in Table 4. Different trends of the β values for individual model VOC/layer-combinations are observed. One noticeable trend is the higher β values for FSP-layers compared to corresponding SG-layers for nearly all the investigated VOCs, except the SnO_2(FSP)/NASICON-propionic acid combination.

Table 4: Estimated α and β values for different SnO_2/additive-layers from regression analysis of $\sum$(G-Go) on exposure to different model VOCs. Data pre-published in[63].

	acetic acid		propionic acid		ethanol		acetone	
	α	β	α	β	α	β	α	β
SnO_2(FSP)	0.75	0.86	2.83	0.85	9.75	0.92	46.32	0.81
SnO_2(FSP)/Alumina	1.42	0.88	7.26	0.80	44	0.73	239	0.65
SnO_2(FSP)/YSZ	1.31	0.85	5.73	0.84	19.6	0.86	77.6	0.81
SnO_2(FSP)/NASICON	1.26	0.86	15	0.57	16.3	0.79	114.8	0.63
SnO_2(SG)	0.74	0.85	3	0.66	13.47	0.66	68.27	0.52
SnO_2(SG)/Alumina	0.37	0.83	1.34	0.65	3.33	0.77	21.27	0.58
SnO_2(SG)/YSZ	0.68	0.82	2.43	0.68	13.75	0.66	84.02	0.50
SnO_2(SG)/NASICON	0.92	0.73	2.75	0.59	17.12	0.66	100.63	0.48

The relative sensor response S (eq.(25)) of the different SnO_2/additive-layers to the different VOCs dissolved in DI water at pH 3 is illustrated in Fig. 50. As a trend, SnO_2(FSP)-layer and SnO_2(FSP)/additive-layers show significantly higher response to all the tested VOCs compared to the corresponding SG-layers. As an exception, the response of SnO_2(SG)/Alumina-layer to acetic acid is higher than the values of the SnO_2(FSP)-layer and all the SnO_2(FSP)/additive-layers. In fact, among SnO_2(SG)-layer and SnO_2(SG)/additive-layers, SnO_2(SG)/Alumina-layer shows the highest response to all the investigated VOCs. This phenomenon cannot be explained by the differences in layer thickness. As visualized in Fig. 41, SnO_2(SG)/Alumina-layer was analysed as the thinnest layer among SG-layers, however, it shows the highest response. This behaviour does not follow the trend discussed in Sec. 4.3.2 (Fig. 43) and is assumed to be due to sensitivity enhancement in SnO_2/alumina-layers in relation to pure SnO_2-layers. However, this trend cannot be confirmed by the corresponding layers prepared in FSP-technique.

Furthermore, the response of the SnO_2(SG)/NASICON-layer to acetic acid is the lowest, although its layer thickness is the highest among the other SG-layers. It is even lower than that of the pure SnO_2(SG)-layer. Surprisingly, for FSP-layers this relation is reverse. The SnO_2(FSP)/NASICON-layer is relatively thin (about 5 µm in average (Fig. 41)) but its response to acetic acid is the highest. In addition, the SnO_2(FSP)/NASICON-layer was measured to show the most pronounced CTP-features when exposed to the four different analytes. This property is very important with respect to the eligibility of those layers for gas analytical purposes and is only outscored by the SnO_2(FSP)/Alumina-layer (Fig. 46).

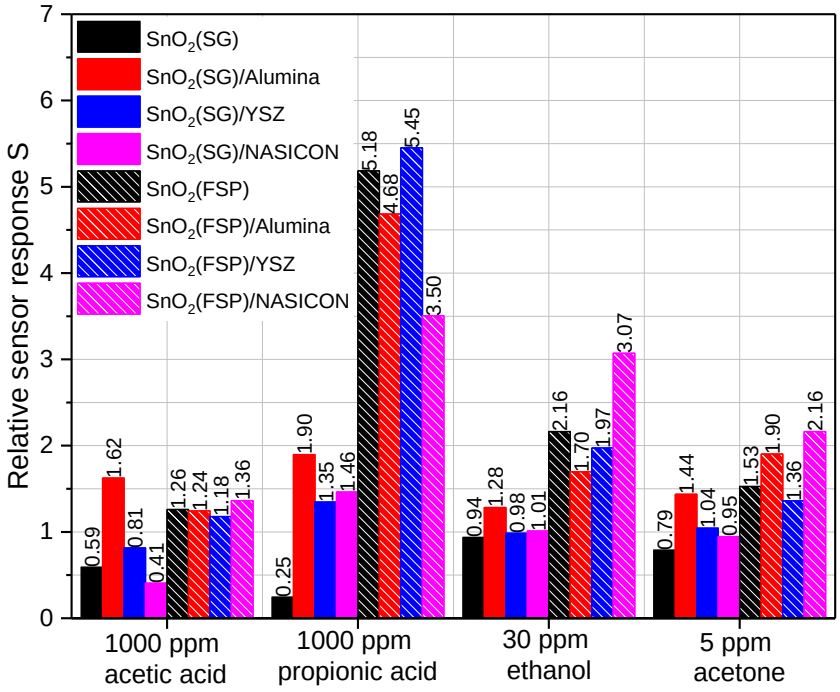

Fig. 50: Comparison of relative sensor response S (eq. (25) of different SnO_2(SG)/additive-layers and SnO_2(FSP)/additive-layers at exposure to different VOCs dissolved in water at pH 3. Data pre-published in [63].

Surprisingly, all three SnO_2(SG)/additive-layers show clearly higher response when exposed to propionic acid compared to acetic acid, although the functional reaction group of acetic and propionic acid are the same, and they differ only by the molecular chain length. This difference in response is even more enhanced in case of the FSP-layers (Fig. 50). The response of SnO_2(FSP)-layer to propionic acid is enhanced in relation to SnO_2(SG)-layer by a factor of about 20. This substantial increase of the response behaviour related to propionic acid was not observed when the layers were exposed to the non-acidic VOCs like ethanol and acetone. Further, in this context, SnO_2(FSP)/NASICON-layer seems to be an exception because the corresponding sensitivities to ethanol and acetone were measured higher in comparison to acetic and propionic acid.

As a first summary and for upcoming discussion, it must be pointed out that for both acidic analytes considerable changes in gas response are observed when the SnO_2(SG) is admixed with additives. This is not the case for the non-acidic VOCs. In the most cases, the sensitivities of the FSP-layers are clearly higher than those of the SG-layers except for the SnO_2(SG)/Alumina-layer. This is highlighted in the large absolute response difference of roughly a factor of 20 of the SnO_2(SG)-layer vs. SnO_2(FSP)-layer and of about a factor of three of the SnO_2(SG)/additive-layers vs. SnO_2(FSP)/additive-layers when they are exposed with

propionic acid. In this regard, the SnO_2(FSP)/NASICON-layer must be discussed as an exception (see Sec.4.3.4). Compared to SnO_2(FSP) and other SnO_2(FSP)/additive composites, SnO_2(FSP)/NASICON-layer showed lowest sensitivity to propionic acid but second highest to acetic acid and highest to other VOCs.

4.3.4. Discussion on gas sensing

The gas sensing mechanism of MOG is well discussed in literature and summarized in Sec.2.3. Possible reaction mechanisms related to acetic acid, propionic acid, ethanol, and acetone are listed in eqs. (27)-(30) [156–159]. They represent total reactions, which may have to be divided into several reaction steps, however, they have in common that per molecule an individual number of formerly trapped electrons (by oxygen surface states) are delocalized by the oxidation reaction.

$$CH_3COOH + 4O^-_{ads} \rightarrow 2CO_2 + 2H_2O + 4e^- \quad (27)$$

$$CH_3CH_2COOH + 7O^-_{ads} \rightarrow 3CO_2 + 3H_2O + 7e^- \quad (28)$$

$$CH_3CH_2OH + 6O^-_{ads} \rightarrow 2CO_2 + 3H_2O + 6e^- \quad (29)$$

$$CH_3COCH_3 + 8O^-_{ads} \rightarrow 3CO_2 + 3H_2O + 8e^- \quad (30)$$

At dynamic operation of the chip-temperature (thermo-cyclic operation mode), as discussed in 2.3.3, non-steady state reaction conditions must be considered even at cycle-periods beyond 15 min [101]. The fractional coverage of the adsorbed species depends not only on the actual temperature but also on the direction (positive or negative) of temperature change. This is well indicated by the un-symmetry of the CTPs visualized in Figs. 30-32.

In this work, all the sensitivity tests have been conducted in gases extracted from the CGP immersed in aqueous sample, i.e. all gas atmospheres discussed are assumed to be more or less saturated by water at the given temperature condition of 18° C. This means, for interpretation of the sensing behaviour of VOCs dissolved in water, the understanding of the role of water is a precondition because in the present context, water is obviously a constituent of the analyte. Not only the VOCs, but the water molecules can also participate in the surface reaction and increases the surface conductance according to eq. (20) as observed in Fig. 44.

Not surprising is the fact that in the same range, where characteristic CTP-features of the VOCs are observed, in most cases, some characteristic deviations of the CTP(hum. air) from the corresponding curves at dry air (CTP(hum. air) - CTP(dry air)), observed as shoulders or peaks, are located (Fig. 47). According to eqs. (27)-(30), by reactions of VOCs with oxygen states, in every case additional water is produced as a reaction product. This means that the fractional coverage of water is increased which should enhance the formation of adsorbed hydroxyl species (eq (20)). However, as further demonstrated in Fig. 47, the height (integral) of very most CTP-features sampled from carboxylic acids are clearly larger than the corresponding (CTP(hum. air) - CTP(dry air))-values. The opposite is the case for several CTPs sampled at ethanol and acetone exposure, although the gas phase concentrations are similar (Table 3).

Remarkably specific and individually structured CTP-features (Fig. 46-Fig. 48), which are clearly different in shape when exposed to different analytes, were observed for all FSP-layers. By comparison, the SG-layers generally show individual CTP-features as well, but less pronounced and with lower sensitivity (G-Go– change vs. analyte concentration). The clearly better specificity of the normalised CTPs of the FSP-layers to all analytes under investigation in relation to the SG-layers is also illustrated in Fig. 47. Another aspect is the relative sensitivity of the layers. As illustrated in Fig. 46, in nearly all cases, the FSP-layer shows the higher CTP-maximum related to the corresponding SG-layer for all analytes exposed. This interpretation is also supported by the CTPs plotted in Fig. 44, which illustrate the difference of the CTP(hum. air) related to the CTP(dry air). In this context, it is a matter of fact that the absolute conductance of these FSP-layers is not lower than those of the SG-layers, although the FSP-layers were prepared generally thinner (Fig. 41). The sensitivity enhancement due to smaller grain size of the FSP-layers with grain diameter, which is in the range of double the Debye length of the electron depletion layer, was expected (see Sec. 2.3.1), but the enhanced specification of the CTP shape structures, which reflect the individual surface molecular reactions, was surprising and discovered by those comparative gas sensing experiments for the first time.

Regarding the surface reaction processes with acetic and propionic acid, different possible reaction routes of carboxylic acids on tin oxide surfaces and reaction intermediates are described in the literature. It is well understood that at lower temperature the carboxylic acids dissociate on the MO surface forming surface carboxylate [160–162], surface acetate and propionate. Surface carboxylate may undergo ketonization reaction [163, 164] as reported for MgO [165], Al_2O_3 [164, 166], TiO_2 [166], ZrO_2 [166, 167], CeO_2 [166], Bi_2O_3 [164], PbO_2

[164], MnO_2 [164]. However, the presence of a hydrogenated oxide surface (O → OH), as could be expected in presence of atmospheres with high water vapor partial pressure, seems to suppress the ketonization reaction [168] and formation of aldehyde as confirmed by IR spectroscopy [168], was reported to prevail [80, 169] and a Mars-Van Krevelen mechanism (see Sec. 2.2.2) [169, 170] has been postulated. The catalytic oxidation reactions of carboxylic acids at highly humid atmosphere were found to start at around 150°C, forming aldehydes as intermediate products between 200-300°C. In case of propionic acid in addition to formaldehyde also acetyldehyde formation was indicated before complete oxidation at round 300-350°C takes place [80]. Similarly, the formation of ketene and acrolein from the surface acetate and propionate respectively by dehydration reaction was reported for ZnO [162] and TiO_2 [171, 172].

The temperature range of carboxylic acid oxidation reactions, as given in literature, on different oxides (200-350°C) fits quite well with the temperature range (250-400°C) of the main peaks/shoulders of the CTPs measured for acetic and propionic acid (Fig. 46) in this work. Of course, much more surface analytical investigations would be necessary to correlate these specific reactions with the specific profile structures of the CTPs (Fig. 46 and Fig. 47) of the individual layers. However, by analysing the features (reaction peaks) of the CTPs produced under well-defined atmospheric conditions, the interaction of acetic and propionic acid on thermo-cyclically operated SnO_2/additive-layers seems to occur at the temperature range of 320-390°C and 300-370°C for acetic and propionic acid, respectively. This indicates similar underlying gas reactions in all the layers under investigation and the difference in reaction temperatures of individual acid may allow analysis of the carboxylic acids by numerical analysis of the CTPs.

Typically, higher absolute G-Go values and pronounced gas specific features on CTPs when exposed to propionic acid compared to acetic acid could be related to (i) different numbers of electrons per molecule transferred to the conduction band by surface reaction with oxygen states (compare eq. (27) with (28)) and/or (ii) to the higher catalytic activity of tin oxide for propionic acid [80]. The measured overall conductance of a CTP and its profile structure reflects the specific gas reactions. In this context contributions from the grain surface, the grain bulk, the IDE/MO interface and from the grain boundaries, as discussed in Sec. 2.3.1, must be considered.

The clearly higher pronounced CTP-features, and higher gas response observed for FSP-layers compared to SG-layers at exposure to carboxylic acids as well as to ethanol and acetone (Fig. 46-Fig. 48) obviously is associated with its different morphology. As discussed in Sec. 2.3.1, smaller average grain size and higher porosity of FSP-layers (Fig. 37 and Fig. 38) provide larger active surface area for gas reaction, as well as increased contribution of the depletion layer in relation to the bulk to the overall conductivity. Furthermore, it is assumed, that agglomerates from densely packed grains as observed in SnO_2(SG)-layers (Fig. 39 and Fig. 40) provide smaller gas penetrability to the reaction sites at the interior of such agglomerates and therefore are less accessible for the gas reactions [67] resulting in reduced gas sensing.

Further, different surface reaction processes with ethanol are described in literature [173–176]. At elevated temperatures, ethanol undergoes dissociation by dehydration on acidic oxides forming ethene and water whereas on basic oxides forms acetaldehyde and hydrogen as surface intermediates by dehydrogenation process. Tin oxide is an amphoteric MO [177]. This means that both reaction paths are possible, but the formation of acetaldehyde has been observed to be the thermodynamically more stable reaction product in a temperature range of 150-300°C [173]. Having the clearly better enhanced individuality of the CTP-shapes of FSP-layers in mind (Fig. 46 and Fig. 47), it is concluded that the surface reaction processes with ethanol seem to be more strongly occurring in SnO_2(FSP) and SnO_2(FSP)/additive-layers compared to the corresponding SG-layers. This means that the reaction of products from dehydration or dehydrogenation of ethanol with adsorbed oxygen state (O^-) are clearly better reflected in specific CTP-features observed at about 350-400°C (Fig. 46 and Fig. 47). As already stated above, this aspect is of high relevance with respect to the chemical analysis capability enabled by numerical analysis of the CTPs [119].

Similar quality difference of CTPs is observed at acetone exposure. The interaction of acetone with adsorbed oxygen state (O^-) on MOs, such as SnO_2 and ZnO are reported in [71, 178–180]. At high temperatures (≥300°C), acetone reacts with adsorbed oxygen states (O^-) forming acetyl group, formaldehyde radical, methyl radical and CO in different reaction steps before forming CO_2. These reactions are represented as gas specific features for SnO_2(FSP) and SnO_2(FSP)/additive-layers at around 300-315°C as a shoulder (Fig. 46 and Fig. 47), whereas no specific reaction peaks are observed in case of SnO_2(SG) and SnO_2(SG)/additive-layers.

Coming back to the CTP-shape structures of the FSP-layers, with regard to the desired capability to analyse the formation of carboxylic acids in fermentation processes well

discriminated to other gas components by numerical analysis of such CTP-features [119], the differences of the CTP-shapes related to acetic and propionic acid vs. ethanol and acetone are mostly pronounced by the SnO_2(FSP)/NASICON-layer and the SnO_2(FSP)/Al_2O_3-layer. It seems that the surface reactions of acetic and propionic acid are catalysed by the presence of NASICON as already discussed in [38]. Much higher sensitivities of SnO_2/NASICON-layers in relation to pure SnO_2-layers and clearly different CTP-shapes were explained by a model of (i) specific Na^+–e^- interactions at the SnO_2/NASICON interface which was assumed to amplify the sensing behaviour compared to pure tin oxide [38, 143] and (ii) the catalytic properties of NASICON which may enhance the formation of intermediate products and spillover to O^{2-} surface states at the neighbouring SnO_2 grains, where they are completely oxidized taking additional influence on the surface depletion layer [143, 181]. The influence of NASICON could be further enhanced if the NASICON grains could be prepared with a grain size, at least comparable if not smaller than SnO_2 grains and could have proper dispersion of NASICON around the SnO_2 grains (Fig. 18b).

The enhanced sensitivity properties of the SnO_2(FSP)/Alumina-layer, may be explained by the existence of Lewis acid sites provided by the alumina, which may influence the dehydration and cracking of the organic molecules [182, 183] promoting intermediate products. The combination of these catalytic properties of alumina with surface processes involving those intermediate products and O^{2-} surface states at very fine SnO_2(FSP) grains, as discussed above, may result in pronounced CTP-features (Fig. 46 and Fig. 47) and also in improved gas response as illustrated in Fig. 50.

In comparison to SnO_2(FSP)/NASICON-layer, the SnO_2(FSP)/YSZ-layer shows clearly lower response to acetic acid, ethanol, and acetone but it is highest for propionic acid. YSZ is known for its oxygen ion conductivity and its catalytic properties for oxidation reactions [184]. This means, similar to the Na^+-e^- interactions in SnO_2/NASICON-layers an O^{2-}-e^- interaction over the SnO_2/YSZ-grain boundaries may be presumably assumed here, which could lead to a similar amplification of the sensing behaviour of individual carboxylic acids as already discussed for the NASICON additive. Indeed, this enhanced sensitivity of the SnO_2(FSP)/YSZ-layers to carboxylic acids was found in [38] as well. However, in this work the relative sensor response amplification vs. the pure SnO_2(FSP)-layer was found to be not significant (Fig. 50). This may be hypothetically explained by the lower O^{2-}-mobility in YSZ and, of course, the effects of e^-–(SnO_2/YSZ) interactions in the (SnO_2/YSZ)-layer has to be expected to be clearly different

related to e^- interaction in (SnO_2/NASICON)-layers. Nevertheless, the CTP-features observed for SnO_2(FSP)/YSZ-layer are somewhat enhanced as well and show some similarities with those of the SnO_2(FSP)/Al_2O_3-layer. This suggests that the decoration of SnO_2(FSP) with YSZ does not induce other additional surface reactions, but the corresponding CTP-features may be shifted due to different catalytic conditions.

Finally, a general overview about the differences in sensitivity is achieved by a closer look to the power-law exponents (β) and pre-exponential factors (α), as defined by eq.(24) and summarized in Table 4. As exemplary illustrated in Fig. 49, the enhanced sensitivity of the FSP-layers compared to corresponding SG-layers is mainly given by the bigger α-value, which is explained by the differences in morphology, as already discussed above. An exception is the SnO_2/NASICON-layer. In case of acetic acid exposure, the pre-factor α is highest of the group of SG-layers and the lowest of the group of FSP-layers. Hence, at propionic acid exposure the α -value fitted for the SnO_2/NASICON-layer is the largest in both groups of preparation (Table 4), however, the exponential values β are the lowest in each group. This is illustrated by the $\sum$G-Go plots in Fig. 49b. In relation to the other SnO_2/additive-layers the SnO_2(FSP)/NASICON-layer attracts attention by a sharp increase of response at propionic acid concentrations below 250 ppm and a markedly lower further increase of response at concentrations beyond. This specific response behaviour of the SnO_2(FSP)/NASICON-layer may give an additional hint to the special conditions of gas response of this composite as already discussed above.

4.4. Dissolved VFA analysis in fermentation samples

4.4.1. Sensor response at different pH

The response of SnO_2(FSP)/additive-layers of SA#1 and SnO_2(SG)/additive-layers of SA#2, was measured over time according to the procedure as introduced in Fig. 32b and is illustrated for different pH conditions in Fig. 51. The corresponding CTPs of different MO-layers as provided on two sensor arrays SA#1 and SA#2 are visualized in Fig. 52. Furthermore, Table 5 shows the GC analysis results sampled at different times of the sequence of sample treatment (Fig. 32). Similarly, in Appendix 5-7, results from the preliminary experiments conducted with different batches of fermentation sample (indicated as #1, #2, #3) and other MOG arrays (SA#W, SA#P, SA#T), however without GC and FTIR analysis of the samples, are presented for comparison.

Table 5: Acetic and propionic acid concentrations as estimated by the GC analysis probed at different times of the measurement sequence (Fig. 51). Data pre-published in [117].

time / h	acetic acid / ppm	propionic acid / ppm
0.2	104	48
2	138	51
8	119	45
10	113	44
22	114	44
24	115	44
27	330	44
30	636	42
32	1100	42
35	2051	43
46	2120	44

In the sample pre-conditioning phase (0-1.75 h, Fig. 51), the sensor arrays were continuously exposed to dry synthetic air. This purging treatment with N_2 (Sec. 2.6.1) was introduced to remove the un-dissociatively and physically dissolved biogas components like CH_4, H_2, CO, etc. from the analysis sample, which are expected to produce cross sensitivity at the MO-layers with respect to the VFA measurements. Immediately after N_2-purging, the sensor arrays SA#1 and SA#2 were exposed to the gas extracted from the analysis sample at pH 8 via the CGP. This moment is indicated by the rise of sensor responses at 1.75h (Fig. 51). At this pH-

condition, the VFAs are expected to be completely in dissociated state (Fig. 23) and the recorded sensor signals do not represent any VFAs but mainly represent the response to humidified air and, perhaps, to some residual physically dissolved biogas components (CO, H_2, CH_4, etc.), and very low concentrations of other residual non-dissociated VOCs in the fermentation sample. Thus, the CTPs measured at this sample condition, e.g. the CTPs pH8@3h (Fig. 52), are observed clearly higher than the CTPs measured at dry synthetic air exposure but are considered as the baseline of the VFA analysis. They do not represent the small but significant acetate and propionate concentration present in the analysis sample as indicated by GC analysis (Table 1, Fig. 51).

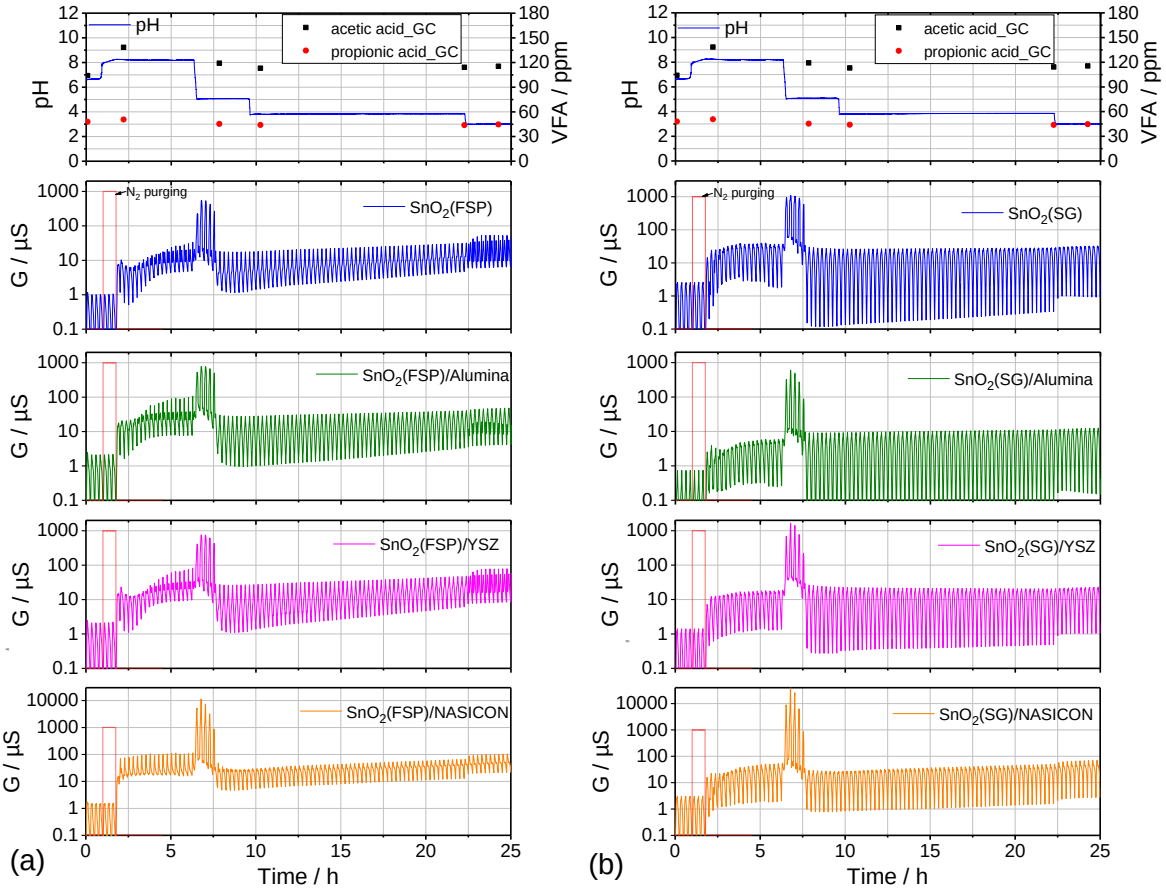

Fig. 51: GC analysis results and sensor response of different SnO_2/additive-layers vs time at different pH conditions of the fermentation sample. (a) SnO_2(FSP)/additive-layers (SA#1) and (b) SnO_2(SG)/additive-layers (SA#2). Sample pre-conditioning phase: 0-1.75h. Data pre-published in [117].

As already mentioned above, most MO-layers show a clear increase of the absolute sensor signal (Fig. 51) with time in time-interval 1.75-6.5 h. This is illustrated even better by the enhancement of specific features of the corresponding CTPs (Fig. 52) of all MO-layers at

around 1-3 min (compare CTPs pH8@3h with CTPs pH8@6.5h) at relatively constant pH 8 condition.

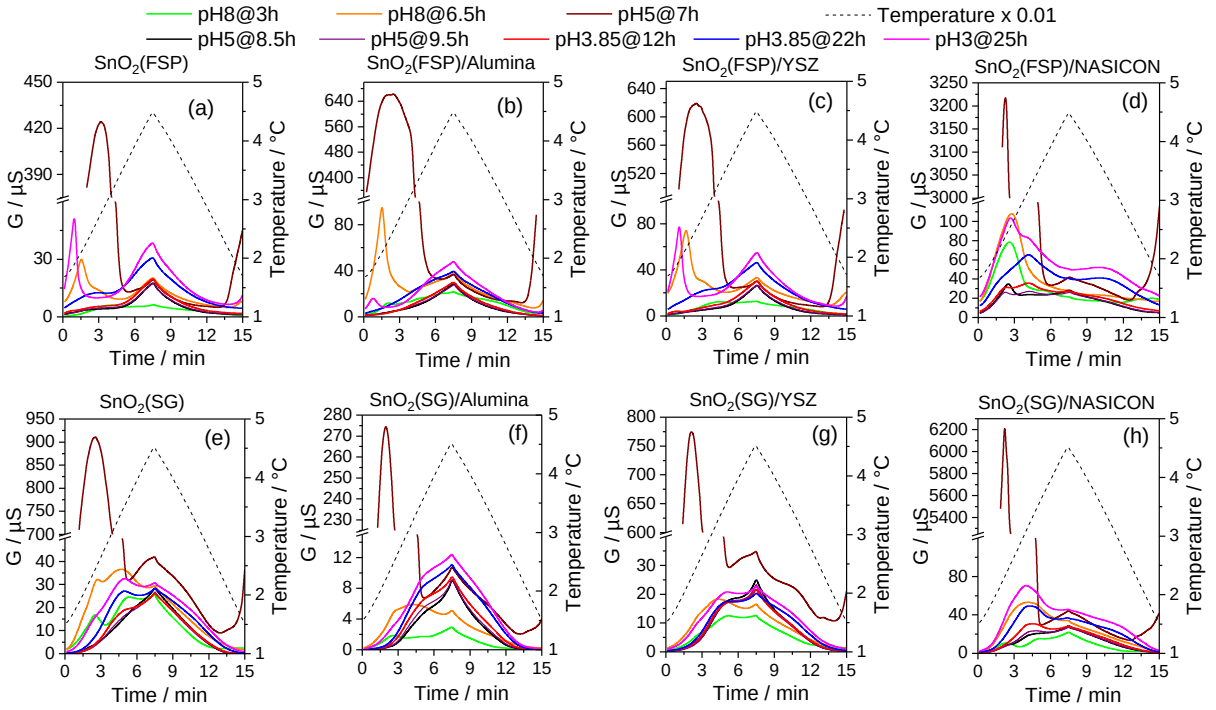

Fig. 52: CTPs of (a) SnO_2(FSP), (b) SnO_2(FSP)/Alumina, (c) SnO_2(FSP)/YSZ, (d) SnO_2(FSP)/NASICON, (e) SnO_2(SG), (f) SnO_2(SG)/Alumina, (g) SnO_2(SG)/YSZ, (h) SnO_2(SG)/NASICON as absolute conductance values at exposure to gases extracted by the CGP at different pH conditions of fermentation sample. Different times of sampling are related to the sequence presented in Fig. 51. Data pre-published in [117].

Further, the absolute conductance values of those CTP-features at a specific time in a temperature cycle is plotted over time to illustrate their progression trend in Fig. 53. For example, G(t=1 min)-values and G(t=1.5 min)-values over time, in case of SnO_2(FSP)-layer, show the trend how conductance value at specific time of CTPs are continuously increasing in time interval 1.75-6.5 h. This clearly indicates that the actual analyte gas composition is continuously changing over time. This, probably, may be due to the activity of the microorganisms in the analysis sample resulting in further production of biogas. However, G(t=3 min)-values are more or less constant in this time interval and is not influenced by the changing gas composition,

An alternative representation of sensor response over time is R' (Fig. 53). R' are calculated as the integral of the CTPs of different SnO_2/additive-layers from 3 to 12 min (i.e. from 26 to 102 sampling points) in a temperature cycle, according to eq. (31). The time interval between 3 and

12 min is chosen for the estimation of R' because the CTP-features that are more representative of the model VFAs (acetic acid and propionic acid) dissolved in DI water at pH 3 were predominantly measured during this time interval (Fig. 46).

$$R' = \sum_{x=26}^{102} G_x \tag{31}$$

Where, G_x is the conductance at a sampling point x.

The sensitive layers show stable R' values from 1.75-6.5 h suggesting that the CTP between 3 and 12 min in a temperature cycle is minimally affected by altering gas composition. However, the CTP-features observed before 3 min do reflect the change in gas composition.

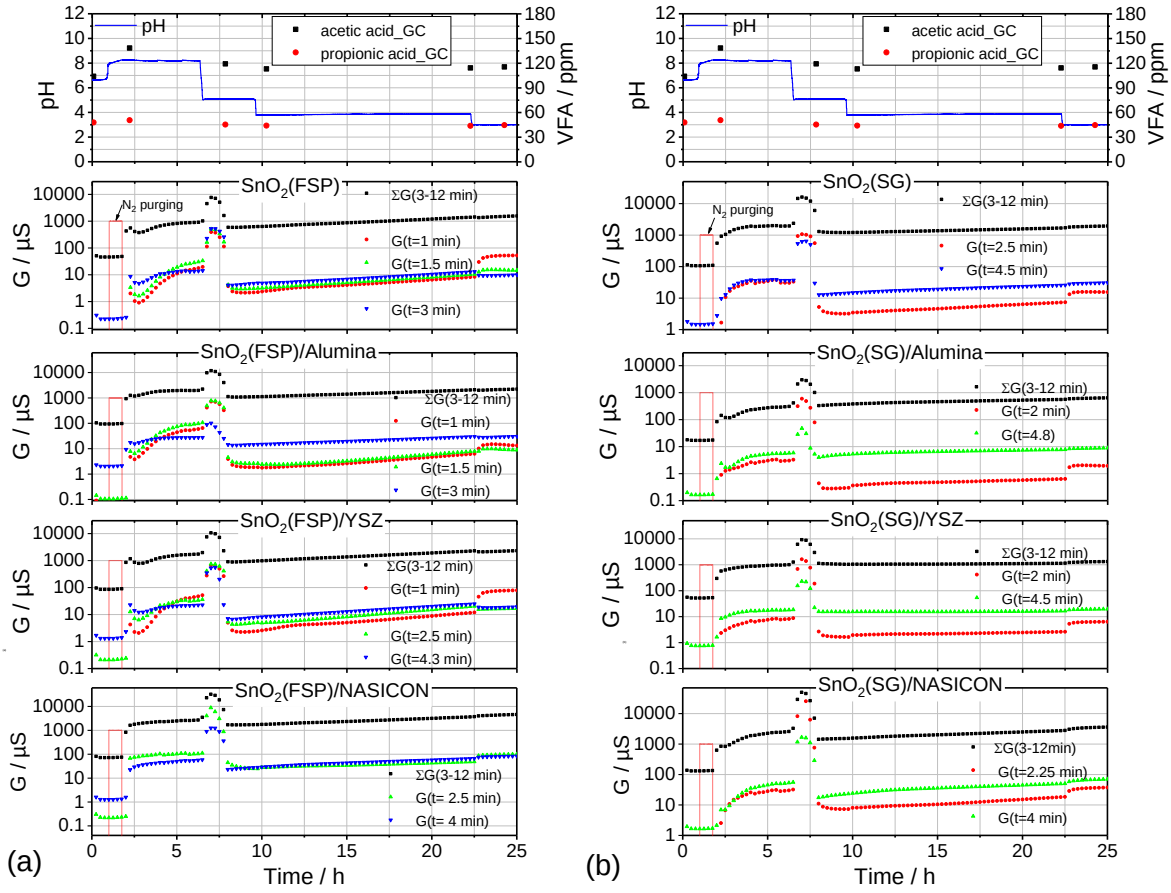

Fig. 53: Sensor response (R') and conductance values G(t=x min) measured at specific time of temperature cycle plotted over time at different pH conditions. (a) SnO_2(FSP)/additive-layers (SA#1) and (b) SnO_2(SG)/additive-layers (SA#2).

With transition to pH 5, intense gas evolution with foam formation was observed. This gas development was intense enough to escape through the backflow protection (water filled gas bubbler) (Fig. 30a) and was registered as highly increased sensor signals in time period 6.5-7.7 h (Fig. 51). It is represented in the corresponding CTPs of all MO-layers by a sharp characteristic peak between 1-3 min as e.g. observed for pH5@7h (Fig. 52).

Comparing the normalised CTPs (equalization of the conductance values at the peak temperature (Tmax)) measured at pH8@3h, pH8@6.5h and pH5@7h, for example, CTPs of SnO_2(FSP)/NASICON-layer (Fig. 55a), reveals that the characteristic peaks observed in those three CTPs are all at the same position with respect to cycle time (about 2.5 min) and sensor temperature (230°C). This observation suggests that the surface reaction of the same gas component could be responsible for those sharp peaks. Besides, those characteristic features are in good resemblance to the CTP-features observed in normalised CTP of SnO_2(FSP)/NASICON-layer (Fig. 55a) at exposure to 2000 ppm CO with 50% relative humidity measured in the automated gas sensor test system [41]. Furthermore, the result (Fig. 54b) of an offline FTIR analysis experiment (Fig. 33c) of the gas collected during this intense gas development at pH 5 condition confirmed the presence of a small concentration of CO admixed with high amount of CO_2 and water vapor. However, the FTIR spectrum does not contain any absorption bands representing VFAs (acetic acid or propionic acid), but small characteristic features of the VFAs are already observed in the CTPs (Fig. 55) at this pH-value. As a first conclusion, this means that at transition from pH 8 to pH 5 not only more and more undissociated VFA is formed (Fig. 23), but also this transition seems to trigger an alteration of the microbiological culture activity, which is observed as an intensive development of CO/CO_2 and, perhaps, other gas components like H_2, which are not IR-active. From the IR-spectrum (Fig. 54) it is concluded as well that the intense gas development is related to the formation of a high amount of gaseous CO_2 as pH is decreased from 8 to 5. The latter pH-value is clearly lower than the pKa=6.5 of the H_2CO_3/HCO_3^--dissociation equilibrium (eq. (32)) and, consequently, formation of CO_2 gas at pH-transition indicates a high concentration of bicarbonate dissolved at pH 8.

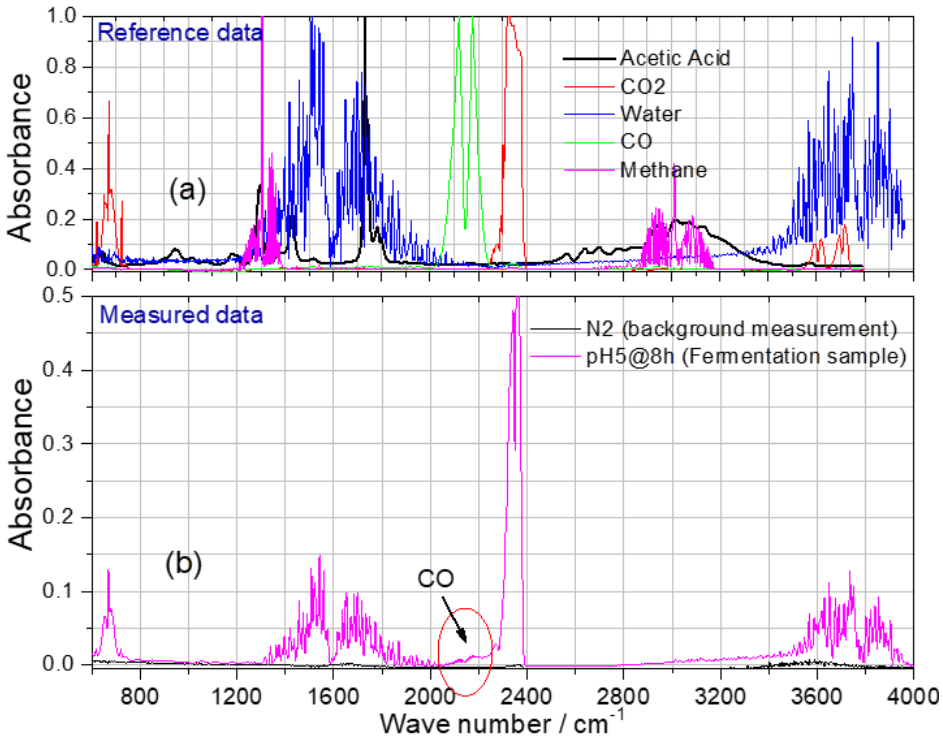

Fig. 54: FTIR analysis data sampled from intense gas evolution at pH5. (a) Reference FTIR absorbance spectrum of acetic acid, CO_2, water, CO and CH_4 [41]. (b) Measured FTIR background spectrum with N_2 and FTIR spectrum of the gas extracted from the analysis sample. Data pre-published in [117].

$$CO_2 + H_2O \leftrightarrow H_2CO_3 \overset{pK_a=6.5}{\longleftrightarrow} H^+ + HCO_3^- \overset{pK_a=10.5}{\longleftrightarrow} 2H^+ + CO_3^{2-} \qquad (32)$$

This, however, is not in contradiction to the interpretation of the high sensor signals observed at this time period of foam forming (see discussion above), because the sensitivity of MOG is well known to be very low to CO_2 but quite high to CO.

The intense gas development ended abruptly without further change of pH at about 7.7h. This is clearly indicated by a sharp drop of the response of all eight MO-layers (Fig. 51) and, correspondingly, by less characteristic peak shape at around 2-3 min in CTPs of all MO-layers (CTPs pH5@8.5h, Fig. 52). The response of most of the MO-layers is now, in fact, lower than the response recorded at pH 8 (6.5 h) except for SnO_2(SG)/Alumina-layer and SnO_2(SG)/YSZ-layer. This is due to the fact that the CTP-response of the two latter layers is observed relatively low at pH 8 (6.5 h) in relation to the other layers. Further, CTP-shape at pH5@8.5h is clearly different compared to the CTP-shape at pH8@6.5h and, of course, also to the CTP-shape at pH5@7h (gas development, Fig. 52). These differences may be explained by the escaping of gases from the analysis reactor during the intense gas development. The escaped gas may

contain residual physically dissolved gases after N_2 purging, newly developed biogas components including other byproducts over time (1.75-6.5 h) and even some portion of undissociated VFAs equilibrated with the dissociated form at pH 5. The intense evolution of CO_2 and correspondingly its high portion in the gas development may have an additional purging effect of the other (low concentrated) gas components. The latter assumption is supported by the GC-analysis results (Fig. 51), which show a small, but significant decrease of the acetic and propionic acid concentrations after the foam formation/gas development event.

Post intense gas development (7.75-9.5 h), the response of the MO-layers seems to be very stable (Fig. 51) at constant pH 5 condition. However, more detailed study of the CTP-shapes (Fig. 52) revealed significant changes, in particular, measured on the SnO_2(FSP)/NASICON, SnO_2(SG)/NASICON-layer and the SnO_2(SG)/Alumina-layer in the time interval over one hour from pH5@8.5h to pH5@9.5h. This is even better illustrated by the plot of the normalised CTPs of SnO_2(FSP)/NASICON-layer and SnO_2(SG)/NASICON-layer (Fig. 55a and Fig. 55c). The response of these layers seems to reflect the change in gas composition over time in good agreement with the former investigations with model VOCs (Fig. 46). Theoretically, substantial activity of methane-forming bacteria is not expected below pH 6 [122, 125]. However, significant activity of acid-forming bacteria occurs above pH 5 [122]. Thus, development of biogas along with other byproducts cannot be excluded in this period of process.

After next step of pH-decrease to pH 3.85 (Fig. 51), namely to a value well below the pKa of the VFAs (4.87 and 4.76 for acetic and propionic acid, respectively), almost 90% of the VFAs are transformed to the undissociated state (Fig. 23) and, as expected, there is an increase of the response of all the MO-layers, which is better visualized as CTPs at pH3.85@12h (Fig. 52). These relatively small CTP-changes of all of the MO-layers (e.g. related to CTPs at pH5@9.5h) increased significantly over the time span of 10 h at constant pH 3.85 condition, and the CTPs became more and more characteristic (compare CTPs at pH3.85@12h with those CTPs at pH3.85@22h (Fig. 52)). Assuming that the small but significant increase of the CTP is not a consequence of a very slow signal response, this observation has to be interpreted as a slow increase of the VFA-concentrations (or other gas components) over time. At pH 3 which is now far below the pKa value of the VFAs, almost all the VFAs are in undissociated state (Fig. 23) and, as expected, the sensitivity of the measurement is highest for all the MO-layers resulting in highly specific CTP-shape represented as pH3@25h (Fig. 52). But the CTPs of the different SnO_2/additive-layers are observed very different in intensity and shape specificity. The CTPs

at pH3@25h of the FSP-layers (Fig. 52a-d) have an additional sharp peak at about 1 min in common, which is shifted to about 2.5 min in case of the SnO_2(FSP)/NASICON-layer. This sharp peak is developed immediately after the pH is lowered to 3 as indicated by G(t=1 min) and G(t=2.5 min) plot over time (Fig. 53) for corresponding layers. The position of those peaks with respect to time and temperature is clearly different to the peaks observed in the CTPs pH8@6.5 and pH5@7h and they may represent the undissociated VFAs and/or other byproducts formed in state of pH 3. However, the CTP-shape of SnO_2(FSP)/NASICON-layer (Fig. 52d) at pH3@25h shows a very similar structure (double peak vs. peak and shoulder) as those observed at pH3.85@12h and even at pH5@9.5h. This indicates again that SnO_2(FSP)/NASICON-layer enables very sensitive VFA-analysis even at pH-states at which only a lower portion of the analyte can be measured in the undissociated state. The SnO_2(SG)/additive-layers show similar signal trends, but the CTP-shapes are clearly less structured and therefore less specific.

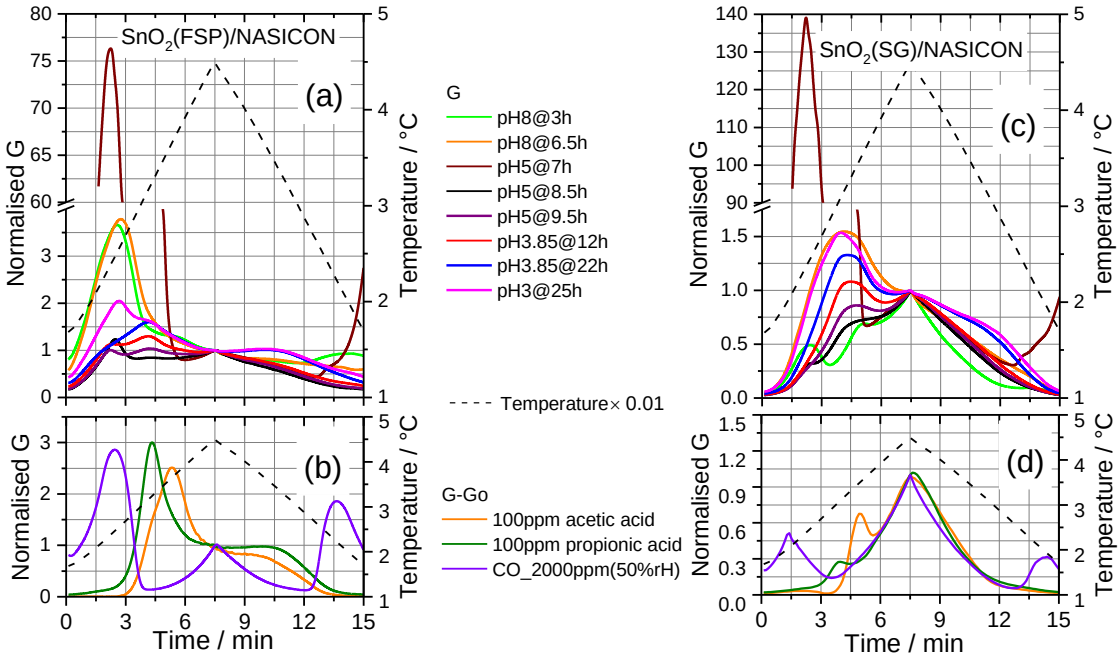

Fig. 55: Normalised CTPs of (a) SnO_2(FSP)/NASICON and (c) SnO_2(SG)/NASICON at different pH conditions of the fermentation sample. Normalisation is made by the (G-Go) value at the maximum temperature of temperature cycle. For comparison, the corresponding normalised CTPs, given as G-Go-values measured on model gases, are illustrated in (b) and (d). Go (used for CTP at 2000ppm CO) is the reference CTP measured at synthetic air with 50%rH, whereas for the CTP-measurements of the dissolved acids Go was measured via CGP in DI water at pH 7. Data pre-published in [117].

The exceptional sensing behaviour of the SnO_2(FSP)/NASICON-layer and SnO_2(SG)/NASICON-layer is even more impressively illustrated by comparing the normalised CTPs at pH5@9.5h, pH3.85@22h and pH3@25h (Fig. 55a and Fig. 55c). Comparing those normalised CTPs with those CTPs recorded at exposure with 100 ppm model acetic acid and propionic acid dissolved in DI water (Fig. 55b and Fig. 55d) reveals that the CTP-features observed at different pH conditions of the fermentation samples are in good resemblance with the position of the peaks observed in measurements with the model VFAs. For instance, the peak observed at about 4 min of CTP pH5@9.5h, in case of SnO_2(FSP)/NASICON-layer, is specifically at the same position as observed for the propionic acid. Similarly, the relatively wide maxima observed in CTP pH5@9.5h at about 4.3 min for SnO_2(SG)/NASICON-layer represents both propionic and acidic acid peaks.

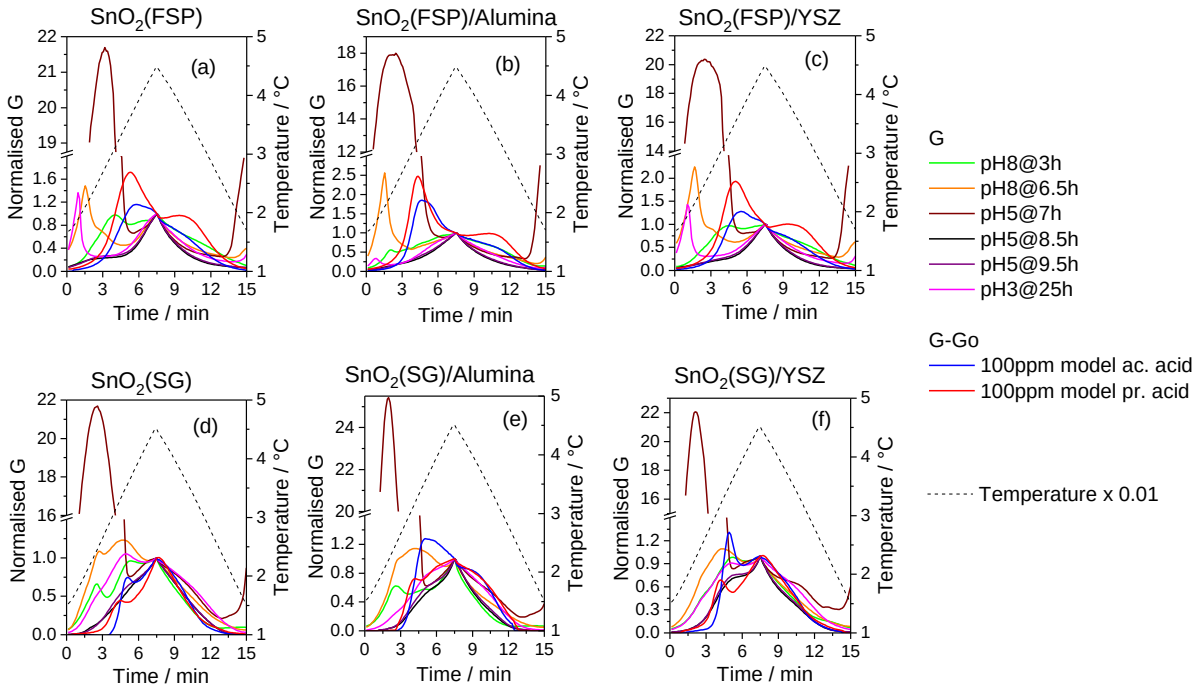

Fig. 56: Normalised CTPs of (a) SnO_2(FSP), (b) SnO_2(FSP)/Alumina, (c) SnO_2(FSP)/YSZ, (d) SnO_2(SG), (e) SnO_2(SG)/Alumina, (f) SnO_2(SG)/YSZ measured at different pH conditions (pH 8, pH 5 and pH 3). Normalisation is made by the (G-Go) value at the maximum temperature of temperature cycle. For comparison, the CTPs of 100 ppm acetic acid and 100 ppm propionic acid dissolved in DI water at pH 3 are visualized as normalised G-Go-values. Here, Go is the CTP measured in DI water at pH 7 (Fig. 46). Data pre-published in [117].

As already stated above, it is quite impressive that SnO_2(FSP)/NASICON-layer and SnO_2(SG)/NASICON-layer show such clear variation in CTP-shape and integral even for such small changes in undissociated VFA concentration at pH5 (Fig. 55), with only around 36% and 43% (Fig. 23) of the dissolved acetate (115 ppm) and propionate (44 ppm) (Fig. 51), respectively, in un-dissociated state. This could be associated with the enhanced sensing behaviour induced by NASICON as discussed in Sec. 4.3.4 and in previous studies [181]. The other SnO_2/additive-layers do not show this correlation of the CTP-shapes with the model acids so clearly (Fig. 56).

As an intermediate summary, these results clearly demonstrate the proof-of-concept that use of CGP after sample pre-conditioning (increase of pH for N_2-purging and then lowering of the pH value below pKa value of VFAs) enables the applicability of well selected SnO_2/additive-layers for acetic/propionic acid analysis in biogas fermentation processes. Further, the MOG could be used even for monitoring of the actual process conditions as well. As shown by the results, the response of the MO-layers to any change in the gas composition is rather fast (at least two temperature cycles i.e. around 30 min). However, the time required for sample conditioning (N_2-purging) must be considered as well. The detection limit of the MO-layers, for e.g. SnO_2(FSP)/NASICON-layer and SnO_2(SG)/NASICON-layer is well below 100 ppm as shown by the results from the measurements at pH 5. In Sec. 4.4.2, the MO-layers response to higher changes in the VFA concentration will be discussed.

4.4.2. Sensor response at varying VFA concentrations

In this section. the sensor responses to additional dosage of acetic and propionic acids into the fermentation sample are studied in relation to the CTPs measured at pH3@25h (Sec. 4.4.1). By comparison of the corresponding CTP-shapes some disclosure about the correlations between those CTP-shapes representing the “original fermentation sample” and those achieved by increase of the acetic/propionic acid content in the fermentation sample is expected.

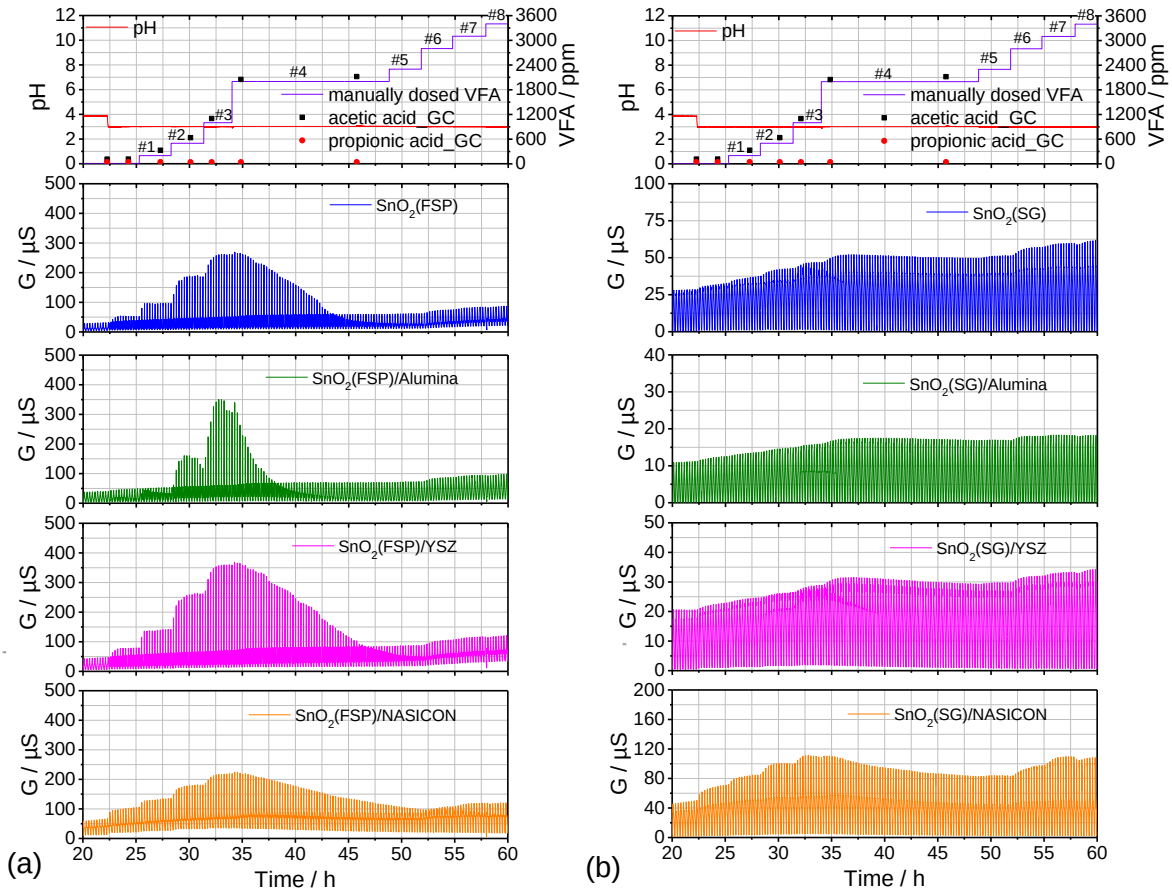

Fig. 57: Sensor response over time of (a) SnO_2(FSP)/additive-layers and (b) SnO_2(SG)/additive-layers to different VFA concentrations (#1: 200 ppm acetic acid, #2: 500 ppm acetic acid, #3: 1000 ppm acetic acid, #4: 2000 ppm acetic acid, #5: 2300 ppm acetic acid, #6: 2300 ppm acid + 500 ppm propionic acid, #7: 2300 ppm acid + 800 ppm propionic acid, #8: 2600 ppm acid + 800 ppm propionic acid) at pH 3 provided by additional dosage of the corresponding VFAs. Data pre-published in [117].

An overview of the responses of the FSP and SG prepared layers at differently adjusted acetic acid and propionic acid concentrations at pH 3 is given in Fig. 57. As a general trend, a clear stepwise increase of sensor response upon pH-change from 3.85 to 3, as already discussed in Sec. 4.4.1, and further addition of acetic acid (200ppm, 500ppm ,1000ppm and 2000ppm) up to around 35th h was observed in all the MO-layers, however, with different individual sensitivity. This stepwise response is more clearly illustrated for the FSP-layers compared to the SG-layers, except for SnO_2(FSP)/Alumina-layer, which shows no response to pH-change and to the first acetic acid dosage (1#).

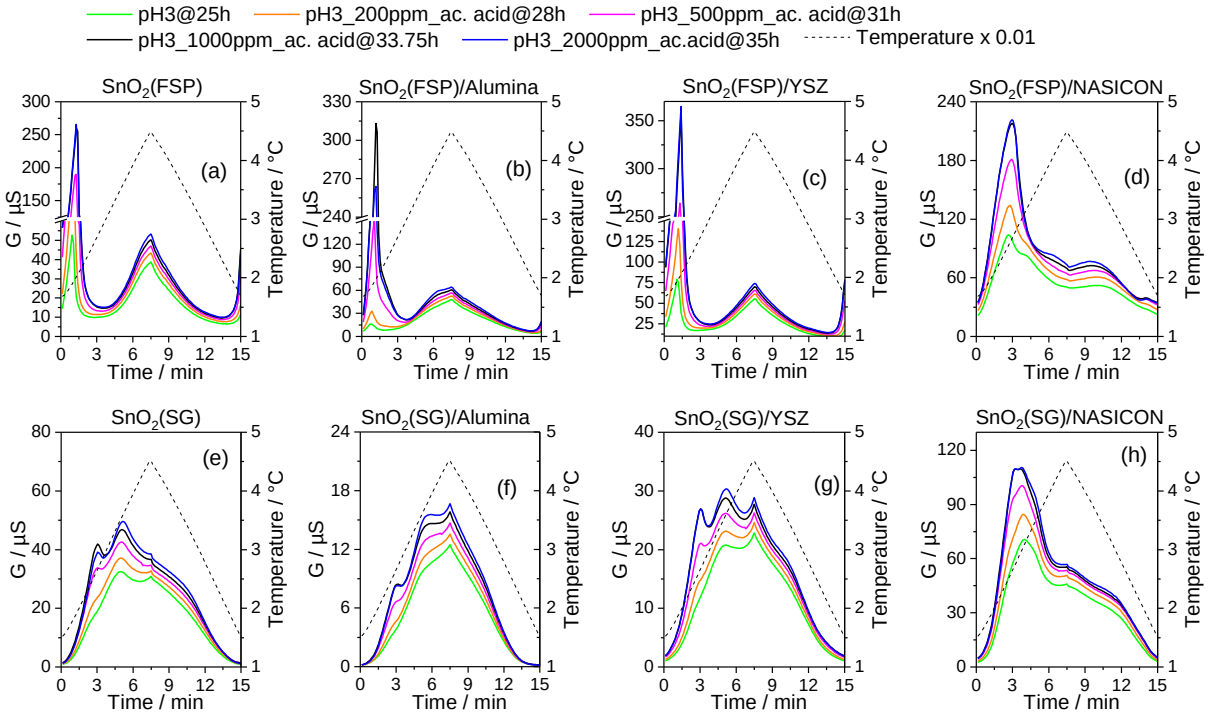

Fig. 58: CTPs measured on (a) SnO_2(FSP), (b) SnO_2(FSP)/Alumina, (c) SnO_2(FSP)/YSZ, (d) SnO_2(FSP)/NASICON, (e) SnO_2(SG), (f) SnO_2(SG)/Alumina, (g) SnO_2(SG)/YSZ, (h) SnO_2(SG)/NASICON illustrating absolute conductance G while exposure to different concentrations (200 ppm, 500 ppm, 1000 ppm, and 2000 ppm) produced by dosage of acetic acid to the fermentation sample at pH 3. Data pre-published in [117].

The corresponding CTPs measured at different acetic acid concentrations, increased in steps by manual dosage, are visualized in Fig. 58. As a matter of fact, there is a monotonic increase of all the CTPs observed in relation to the CTPs measured at pH3@25h. In good agreement with the discussion in Sec. 4.4.1, this indicates that indeed, the CTP-structure at pH3@25h is dominated by some acetic acid-content. The characteristic feature of FSP prepared layers is predominantly the sharp increase of the peak at about 1 min with increasing acetic acid concentration, which is shifted to about 3 min in case of the SnO_2(FSP)/NASICON-layer (Fig. 58d). In contrast, the SG-layers (Fig. 58e-h) are characterized by a double peak or shoulder/peak during heating phase (about 3 min and 5 min) of the temperature cycle. This characteristic structure becomes more pronounced with increasing acetic acid concentration. Hypothetically, this may indicate roughly two different kinds of reaction sites, which may be a consequence of the much broader SnO_2 grain size distribution of the SG-prepared layers (Fig. 39, Sec. 4.2). In case of SnO_2(SG)/NASICON-layer, those two features are not well separated for lower acetic acid concentrations but could be clearly distinguished, for example, as double peak in CTP pH3_2000ppm_ac.acid_35h (Fig. 58h).

The sensor response of FSP-layers and SnO_2(SG)/NASICON (Fig. 57) started to decrease abruptly without further change of pH or acetic acid concentration after the acetic acid concentration had reached 2000 ppm, with individual rate beyond around 35h but with much lower rate beyond 37.5h for the other SG-layers. The reason for this decrease of the sensor response is not clear up to now. It may indicate the change in gas composition over time by still running bio-fermentation processes. Such a change in the gas composition could be represented by the decrease of the most characteristic CTP-peak of the FSP-layers at about 1 min (Fig. 59a-c) and at about 2.5 min measured on the SnO_2(FSP)/NASICON-layer (Fig. 59d), respectively. Additionally, the SG-layers show systematic decrease of the corresponding CTP-features, but with lower rate. Regarding the FSP-layers, this trend of CTP-change is opposite to that observed by dosage of acetic acid (Fig. 58), which could give rise to the assumption that decomposition of VFA is observed here (Fig. 59). However, this assumption is not so clearly confirmed by the CTP-changes of the SG-layers (Fig. 59).

Further addition of acetic acid at 48.8h (Fig. 57) resulted in small but significant increase of the response of FSP layers (Fig. 57a) compared to SG-layers (Fig. 57b), which is better visualised in Fig. 60(e.g. compare CTPs pH3_2000ppm_ac.acid@48.5h and pH_2300ppm_ac.acid@51.5h). The response of SG-layers to acetic acid appears to be saturated which may be related to their lower signal range and lower sensitivity to acetic acid compared to the FSP layers (Fig. 50, Sec. 4.3.3iv). However, the addition of 500 ppm and 800 ppm propionic acid at 51.5 h and 54.5 h respectively, resulted in a clear stepwise increase of the response of all the MO-layers (Fig. 57), which is even better illustrated in the CTPs (Fig. 60) by clear increase of the absolute conductance in the temperature range between 3 min (about 250°C) and the peak temperature, i.e. clearly beyond the temperature where the main response to acetic acid was observed. This effect could be related to the higher sensitivity to propionic acid compared to acetic acid (Fig. 50, Sec. 4.3.3iv) and gives some hint for some ability to discriminate between both kinds of acids. Again, CTPs of SnO_2(FSP)/NASICON-layer and SnO_2(SG)/NASICON-layer, but also SnO_2(FSP)/YSZ-layer and SnO_2(SG)/YSZ-layer, show excellent sensing behaviour and specificity to acetic acid and propionic acid which will now be discussed a little bit closer.

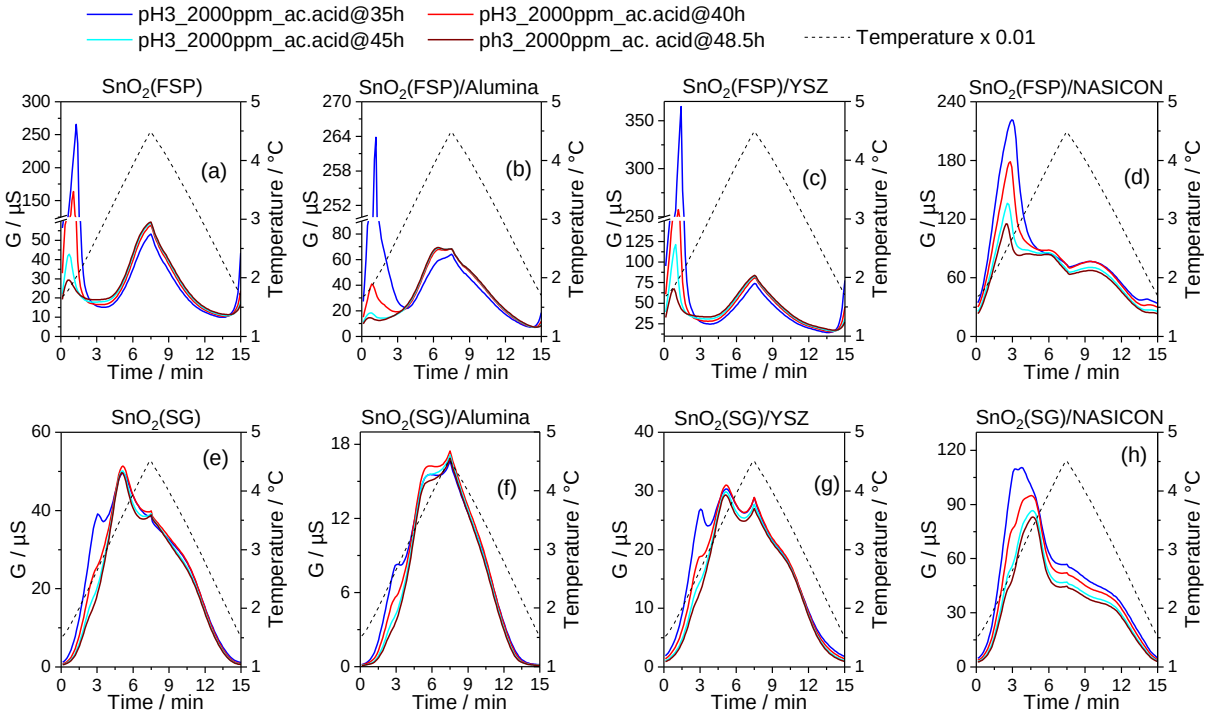

Fig. 59: CTPs measured as absolute conductance G on (a) SnO_2(FSP), (b) SnO_2(FSP)/Alumina, (c) SnO_2(FSP)/YSZ, (d) SnO_2(FSP)/NASICON, (e) SnO_2(SG), (f) SnO_2(SG)/Alumina, (g) SnO_2(SG)/YSZ, (h) SnO_2(SG)/NASICON at constant acetic acid concentration (2000ppm) of the fermentation sample at pH 3. Data pre-published in [117].

Further increase of acetic acid concentration (2000 ppm to 2300 ppm) shows decrease of the CTPs at the lower temperatures i.e. at around 1-1.5 min (Fig. 60c-d). Additional dosing of propionic acid results in a general increase of the CTPs, but major increase at the higher temperatures between about 250°C and 400°C. Finally, further increase to 2600 ppm acetic acid leads to further decrease of the peak at 1.5 min measured on SnO_2(FSP)/NASICON-layer (Fig. 60d), but to a general increase of conductance in the whole CTP-range in case of SnO_2(FSP)/YSZ-layer (Fig. 60c).

These results show that there seems to exist a correlation between the dosed VFA type and the CTP-features, but different kind of correlations are observed at different layers, i.e. these may represent different surface processes dependent on the additive. In case of SnO_2(FSP)/NASICON-layer increase of acetic acid concentration seams to depress surface reactions represented by the CTP-peak at 1.5 min. This is not observed in the CTPs measured on SnO_2(SG)/NASICON-layer (Fig. 60h), perhaps, due to less pronounced CTP-shape specificity.

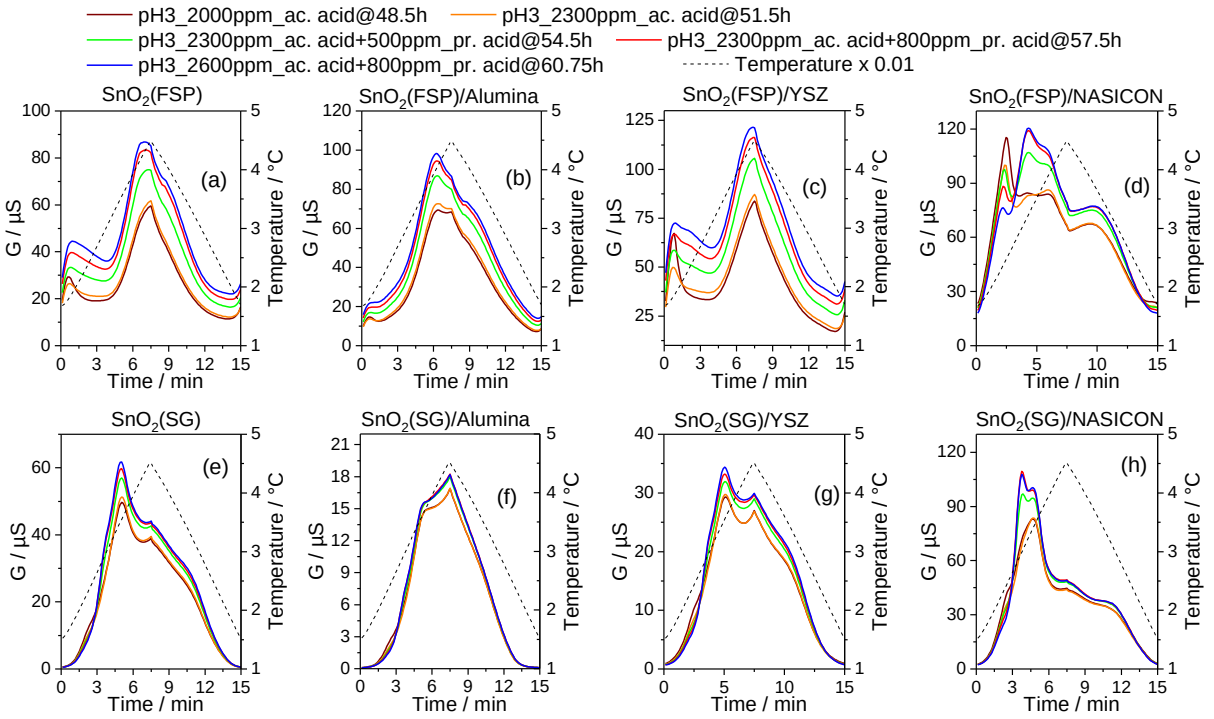

Fig. 60: CTPs measured as absolute conductance G on (a) SnO_2(FSP), (b) SnO_2(FSP)/Alumina, (c) SnO_2(FSP)/YSZ, (d) SnO_2(FSP)/NASICON, (e) SnO_2(SG), (f) SnO_2(SG)/Alumina, (g) SnO_2(SG)/YSZ, (h) SnO_2(SG)/NASICON after further increase of acetic acid and propionic acid concentrations in steps by manual dosage to the fermentation sample at pH 3. Data pre-published in [117].

A better overview of sensor response vs. total VFA-dosage (both, acetic and propionic acid) at pH 3 condition may be given by the dependency of the CTP integral (R'') on dosed VFA (Fig. 61), calculated as the integral of the CTPs of different SnO_2/additive-layers according to eq.(33).

$$R'' = \sum_{x=1}^{n} G_x \tag{33}$$

Where, G_x is the conductance at a sampling point x and n is the total number of the sampling points in one measurement cycle, in this case n=128.

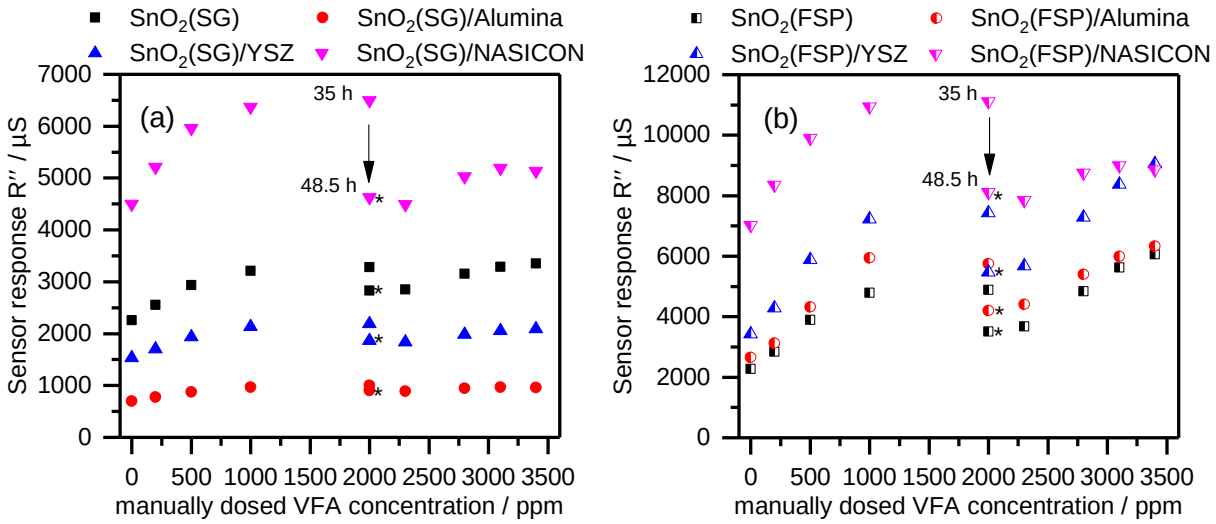

Fig. 61: CTP integrals of (a) different SG prepared layers and, (b) FSP prepared layers vs. manually dosed VFAs concentration in fermentation sample at pH 3 condition as given in Fig. 58 and Fig. 60. Zero concentration value represents the total VFA concentration at pH 3 condition before dosage i.e. the sum of acetic and propionic acid concentrations as analysed by GC analysis. The next concentration values represent the additional VFA concentration (acetic and propionic acid) manually dosed according to Fig. 32b. For 2000 ppm manually dosed VFA concentration two absolute sensor responses of each of the sensitive layers are presented. They represent the absolute sensor response at 35 h and 48.5h (marked by *) and clearly indicate the decrease of the sensor response within this time span as observed in the CTPs in Fig. 57 and Fig. 59. Data pre-published in [117].

In general, two different dependencies could be observed, one up to 1200 ppm, which represent pure acetic acid dosage, and the other at 2000 ppm VFA and beyond. The first dependency represents the situation between 20 h and 35 h (Fig. 57) of measurement whereas, the second dependency represents the CTP increase vs. acetic/propionic acid dosage (Fig. 60) after the considerable decrease of the CTPs and change of their profile shapes within 13.5 h (35 h – 48.5 h) at constant acetic acid concentration (2000 ppm, Fig. 59).

Obviously, SnO_2(FSP)/additive-layers (Fig. 61b) show clearly higher absolute sensor response compared to the SnO_2(SG)/additive-layers (Fig. 61a). However, among SnO_2(SG)/additive-layers (Fig. 61a) the CTP integrals of the SnO_2(SG)/NASICON-layer are clearly the highest (Fig. 58 and Fig. 60). whereas among the FSP-layers (Fig. 61b) the SnO_2(FSP)/NASICON-layer shows highest absolute sensor response only to dosed acetic acid, but beyond 2000 ppm acetic acid SnO_2(FSP)/YSZ-layer shows highest sensitivity (CTP-integral change) vs. dosed propionic acid (Fig. 61b).

4.4.3. Comparison of sensor response to VFA dissolved in DI water and in fermentation sample

The absolute sensor response (R), calculated as integral of whole CTP (from CTPs shown in Fig. 52) according to eq. (24) vs acetic acid concentration in fermentation sample between 25 h and 35 h (Fig. 57), as estimated by GC analysis, is well fitted by a power law. Here, Go is the CTP measured at pH8@3h (Fig. 52). As an example, the integrals and their regression curves for SnO_2(FSP)/NASICON-layer and SnO_2(SG)/NASICON-layer are shown in Fig. 62.

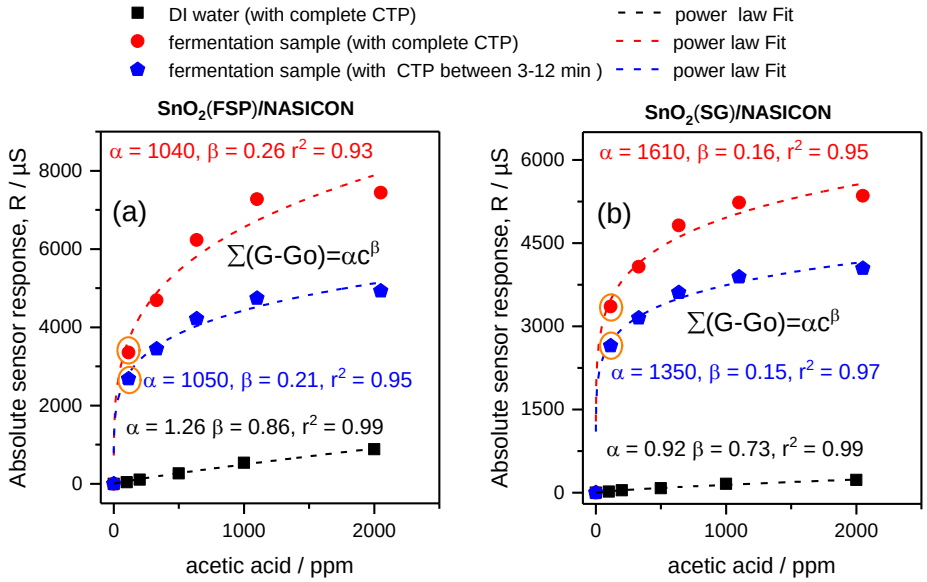

Fig. 62: Absolute sensor response (R) calculated as CTP integral (∑(G-Go)) of (a) SnO_2(FSP)/NASICON, (b) SnO_2(SG)/NASICON vs acetic acid concentration in DI water and of a fermentation sample. For the measurements with DI water, Go is the CTP measured at pH 7, whereas for the measurements with fermentation sample, Go is the CTP measured at pH8@3h (Fig. 52). Integral values for fermentation sample marked by orange circles represent the integral of the CTP measured at pH3@25h.

The value of R, as calculated from the same CTPs, but estimated from 3 to 12 min, is fitted by a power law with better quality as compared to the entire CTPs Fig. 62. Moreover, the CTPs integrated between 3 to 12 min in a temperature cycle are more sensitive to VFAs related to the CTP-integrals based on the model VFAs measured in DI water (Fig. 46, Fig. 62). The enhanced quality of fitting is as expected. Similar results are obtained for other layers as well. This is shown in Appendix 4. Since the CTP-features before 3 min and after 12 min are excluded, obviously R calculated from CTPs from 3 to 12 min is lower than that of whole CTP (Fig. 62).

However, the estimated R-values from CTPs measured between 3 and 12 min as calculated for the fermentation sample are clearly higher than the R-values calculated for DI water measured at a similar concentration range of acetic acid. This offset is most likely to be caused by the propionic acid (44 ppm) in the fermentation sample at pH 3, which remains constant for higher acetic acid concentrations as given by the GC analysis. Further, it should be noted that SnO_2(FSP)/NASICON-layer and SnO_2(SG)/NASICON-layer are more sensitive to propionic acid than acetic acid, as observed in measurement with model VFAs (Fig. 46, Fig. 50, and Appendix 3). Furthermore, the possibility of cross-sensitivity to biogas components (CO, H_2) and other trace VOCs like alcohols and ketones in fermentation samples that may have developed over time between 25 h and 35 h can also contribute to the observed offset.

The above discussion implies that based on the power law regression curve (Fig. 62), a very impressive dependency of the CTP-integrals on the real VFA concentration in the fermentation liquid was found. However, having a quantitative estimation of VFA-concentrations in fermentation samples in mind, this function is not comparable with a model-calibration function using power law generated from model acetic acids dissolved in DI water but can be used to monitor qualitative trends of VFA-developments during biogas fermentation processes.

5. SUMMARY AND OUTLOOK

The aim of this work was to investigate for the first time if thermo-cyclically operated metal oxide gas sensors (MOGs) of the tin oxide type can be qualified for continuous monitoring of the development of volatile fatty acids (VFAs) in biogas fermentation liquids. The investigations were two-fold:

First, with respect to the need to analyse very low VFA-concentrations, the influence of the tin oxide morphology as well as the influence of the different additives on the sensing behaviour had to be studied. For identification of dissolved VOC special emphasis was taken on visualization and validation of the features of the sensor signals. This means the features of the resulting conductance over time profiles (CTPs) of thermo-cyclically (150(±5) °C- 450(±5) °C) operated tin oxide gas sensors to analyse acetic acid, propionic acid, ethanol, and acetone, dissolved in water had to be studied and evaluated. Dissolved VOCs were extracted from the liquid using a carrier gas probe consisting of a gas permeable silicon rubber membrane, which separates the liquid sample from the carrier gas flow (synthetic air). Based on the literature survey, several SnO_2/additive gas sensing composites were prepared and screened. Finally, with respect to their remarkably high sensitivity and most characteristic CTPs, alumina, YSZ and NASICON(x=2) were selected as additives for further investigations.

The second part of this work was to investigate experimentally, whether the quasi-online analysis of VFAs, such as acetic and propionic acid, in biogas fermentation processes is possible by continuous sampling of those CTPs and analysis of their features, if well suitable MOG-layers are available.

For this purpose, pure SnO_2 nanoscaled powders were produced using two different synthesis routes, (i) sol-gel (SG) method and (ii) Flame spray pyrolysis (FSP) method, which ensured very different morphologies. Each type of SnO_2 powder was admixed with different additives (alumina, YSZ, and NASICON(x=2)) and were converted into dispensable thick film pastes. By micro-dispensing of these pastes on self-fabricated, pre-prepared thin-film Pt-Interdigtal Electrodes (IDE) of a fourfold sensor-chip with a Pt thin-film heater, two sensor arrays, each comprising four different sensitive layers (a pure SnO_2-layer and three different SnO_2/additive composites) were fabricated simultaneously but the sensor arrays differ by the SnO_2 preparation routes. To get deeper insight of the influence of layer thickness on the sensing behaviour, a third sensor array was prepared comprising SG prepared SnO_2-layers with different thickness.

The structural properties of the SnO_2 powders and NASICON powder were characterized by X-ray diffraction analysis (XRD). The morphological properties of each SnO_2-layer and SnO_2/additives were investigated by environmental scanning electron microscopy (ESEM) and the distribution of the additives in the respective SnO_2 was additionally studied with energy dispersive spectroscopy (EDS/EDX). FSP prepared SnO_2-layers consist of very homogenous fine grains with very narrow grain size distribution producing highly porose layers. The average grain diameter was estimated to be about 15nm. However, SG prepared SnO_2 consist of grains with a wide distribution of block sizes. The crystal blocks show a sub-structure consisting of densely packed fine grains with an average grain size of about 20 nm, well comparable with that of the FSP prepared SnO_2-layer. EDS analysis revealed that the additives are not homogenously distributed in the SnO_2 matrix. The grain blocks of SG prepared SnO_2 were bigger or comparable in size with the additives whereas in case of the FSP prepared SnO_2, the grain size of the additives was found to be clearly larger in relation to the SnO_2-grains. This is especially valid for the NASICON-grains. Further, the thickness of all the sensitive layers of the three sensor arrays prepared were characterized by confocal microscopy. Due to limited reproducibility of the dispensing process, each layer shows an individual thickness profile and varies in absolute thickness. The influence of these individual thickness properties on the sensing characteristics of the metal oxide-layer was also a matter of extensive tests before the major investigations with model VOCs were started. FSP-prepared layers were prepared clearly thinner in comparison to SG prepared layers.

The experiments with model VOCs (acetic acid, propionic acid, acetone, and ethanol) have impressively shown that SnO_2/additive-layers with SnO_2-powder prepared by FSP technique provide considerably better sensitivity to all VOCs tested compared to those SnO_2/additive-layers with SnO_2-powder prepared by SG technique. Surprisingly, there is not only better sensitivity but also more enhanced specificity of the CTP-features of FSP-prepared SnO_2/additive-layers versus SG prepared SnO_2/additive-layers when the sensors are thermo-cyclically operated. This was interpreted as the result of the different SnO_2-morphologies consisting of fine grain networks with high porosity, as provided by the FSP-layers, in relation to the SG prepared layers. It is well known that the FSP-layers provide highly active surface sites for gas reactions which seem to be one of the key factors favouring target gas–metal oxide interactions which ultimately result in enhanced gas specific CTP-features. This is highlighted by very distinctive CTP-features when exposed to acetic or propionic acid in comparison to CTPs measured for ethanol and acetone vapours.

Furthermore, a characteristic influence of each additives (alumina, YSZ, NASICON(x = 2)) on the CTP-features could be disclosed, respectively. This may be a result of catalytic effects, but also of specific electron-mobile ion interactions at SnO_2-additive interfaces when the additive is a solid electrolyte, such as YSZ or NASICON, as already reported in earlier studies. It is supposed that those interactions may take influence on the target gas reactions with the oxygen surface states. These specific CTP-features with clearly higher sensor signal even at low concentrations (100 ppm) of dissolved acetic and propionic acid make the SnO_2(FSP)/additive-layers (additives: alumina, YSZ, NASICON) very promising candidates for monitoring of VFAs (acetic and propionic acid) development in different processes like biogas fermentation.

Thus, in the later part of the study, a potential quasi-online method for VFAs (acetic and propionic acid) analysis in biogas fermentation processes using thermo-cyclically operated MOG arrays complemented by a carrier gas probe was conceptualized and implemented in a laboratory setup. For demonstration and characterization of this advanced monitoring concept, the same two sensor arrays were used for the measurements of the dissolved VFAs in the fermentation sample as prepared in the laboratory for the studies of the model VOCs. The fermentation sample was prepared at room temperature condition by regular feeding of the biological substrate as extracted from the sewage plant. 10 mg of dried beer marc and 50 ml of wood juice were fed to the substrate in the intervals of three to four days for several months. 1 l of fermentation sample was used per sensitivity characterisation tests of the MOG arrays. About 6 sensitivity test experiments were conducted using different batch of fermentation samples.

The major challenge was to analyse the VFAs developed in the fermentation sample in presence of high concentrations of biogas (CO, H_2, CH_4, etc.). Faced to the well-known cross-sensitivities of MOG to those biogas components and to their high concentrations as expected, a pre-treatment process had to be introduced to get rid of the biogas components without loss of the VFAs. This was made possible by extraction of a small volume (1l) of sample from the main fermentation reactor and purging with N_2 for 45 min at pH 8. After decrease of the pH to three in several steps by dosage of phosphoric acid, the gas sensing behaviour of the SnO_2/additive-layers could be investigated by analysis of the CTPs measured. These measurements at different pH conditions (pH 8, pH 5, pH 3.85 and pH 3) allowed variation of the fraction of undissociatively dissolved VFAs in the fermentation sample, their concentration in the carrier gas, and consequently, their influence on the CTPs. This means, by analysis of the

corresponding CTP-shapes, the CTP-features representing the VFAs could be identified. All these experiments were referenced by GC-analysis. Obviously, CTPs measurements at pH 3, which is well below the pKa value of the VFAs (about pH 4.8) and in this sample condition all the VFAs are completely in undissociated state, yield most pronounced CTP-features representing the VFAs. For better verification of the CTPs representation of VFAs, CTPs at different VFA-concentrations experimentally simulated by manual dosage of acetic acid and propionic acid to the fermentation sample at pH 3 were measured as well. Their rather similar shape characteristics to the CTPs measured for the original fermentation liquid at pH 3 was impressively confirmed. The high significance of the CTPs for VFA-analysis was further confirmed by a power law dependency of the CTP-integrals vs. VFA-concentration. However, this dependency is not comparable with a model calibration function generated from model acetic acids dissolved in DI water but could be used to monitor qualitative trends of VFA-developments during biogas fermentation process.

Essential results of this work are the experimental facts that the additives and the SnO_2/additive-layer morphology take profound influence on the CTPs. The FSP-based layer show clearly better sensitivity compared to SG prepared layers and provide CTP specificity of higher quality. As mentioned before, this is related to the particular morphology consisting of nano-scaled fine SnO_2-grains with extremely high surface/volume ratio of the grains, very narrow grain size distribution, very high porosity, and probably, high surface state energy.

Some preliminary investigation results showed that the gas development triggered by lowering of the pH value of the fermentation liquid from pH 8 to pH 5 and the continuous change of the analyte gas composition over time take clear influence on the CTPs of the SnO_2/additive-layers. This means that these changes of the CTP-shape reflect changes of the actual biochemical situation, although the underlying biochemical reaction processes are not known in detail up to now and was not focus of the present study. In particular, the CTPs of SnO_2(FSP)/NASICON-layer and SnO_2(SG)/NASICON-layer were found to show very high sensitivity and strikingly enhanced specificity to acetic and propionic acid and are remarkably well reproducible. These outstanding sensing characteristics were related to special e^-–Na^+interactions across the SnO_2-NASICON interface, as already reported in earlier studies.

Although an applicable measurement setup for field analysis tests could not be realized in the frame of this work, these preliminary studies clearly show that some well selected, thermo-cyclically operated SnO_2/additive-layers are very interesting candidates for early in-situ

monitoring of developing VFA in biogas fermentation processes, if appropriate additives well adapted to the analysis problem, such as highly sensitive SnO_2(FSP)/NASICON-layers, allow the extraction of representative CTP-features of the target gas component.

To make the novel VFA monitoring system more feasible in real biogas plants, there are a few aspects that need to be investigated further. The current study involved a long sample conditioning process, involving purging the sample with N_2 gas for 45 min and gradually reducing the pH level down to 3 (starting from 8 and going down to 5, 3.85, and eventually 3).The first approach to streamline the measurement duration is to design a smaller analysis reactor that can fully immerse the CGP in the sample while using less sample volume. With the reduced sample volume, the duration of purging with N_2 gas is assumed to be substantially reduced.

The measurements at different pH conditions pH 5, pH 3.85 and pH 3 allowed variation in the fraction of undissociatvely dissolved VFAs in the fermentation sample and enabled investigation of their influence on the CTPs. Considering that the CTPs measured at pH 3 are more representative of VFAs, for the practical applications, signal measurement at pH 8 after N_2 purging (base line) and pH 3, would be sufficient for the analysis. With this approach, the measurement duration can be further shortened to about one to two hours. This means, as fermentation processes are rather slow, even conducting 3-4 VFA-analysis per day would be a significant improvement in monitoring quality related to the state of the art.

Hence, further studies will be necessary in future (i) to correlate CTP-features with the underlying biochemical processes, (ii) to develop an efficient calibration method and numerical CTP-analysis procedure to quantify the VFA-concentrations. (iii) For instance, implementing machine learning approaches could help to make most of the manifold information from the sensor arrays and enhance analysis capabilities. In this context, further enhancement of the sensitivities to specific gas components, the specificities of the corresponding CTP-features and the analysis quality provided by the SnO_2(FSP)/NASICON-layers, as observed in these studies is expected, if the homogeneity of the SnO_2(FSP)/NASICON-layers could be considerably enhanced, i.e. the NASICON powder could be prepared even finer (e.g. by extended ball-milling or by modification of the preparation route) similar to those of the SnO_2-powder as prepared by the FSP technique. This would probably further enhance the sensitivity amplification effect, as already assumed in a hypothetical model in the past.

BIBLIOGRAPHY

[1] L. Björnsson, M. Murto, and B. Mattiasson, "Evaluation of parameters for monitoring an anaerobic co-digestion process," *Applied Microbiology and Biotechnology*, vol. 54, no. 6, pp. 844–849, 2000, doi: 10.1007/s002530000471.

[2] P. F. Pind, I. Angelidaki, and B. K. Ahring, "A new VFA sensor technique for anaerobic reactor systems," *Biotechnology and Bioengineering*, vol. 82, no. 1, pp. 54–61, 2003, doi: 10.1002/bit.10537.

[3] H. M. Falk, P. Reichling, C. Andersen, and R. Benz, "Online monitoring of concentration and dynamics of volatile fatty acids in anaerobic digestion processes with mid-infrared spectroscopy," *Bioprocess and Biosystems Engineering*, vol. 38, no. 2, pp. 237–249, 2015, doi: 10.1007/s00449-014-1263-9.

[4] J. Kretzschmar, L. F. M. Rosa, J. Zosel, M. Mertig, J. Liebetrau, and F. Harnisch, "A Microbial Biosensor Platform for Inline Quantification of Acetate in Anaerobic Digestion: Potential and Challenges," *Chemical Engineering & Technology*, vol. 39, no. 4, pp. 637–642, 2016, doi: 10.1002/ceat.201500406.

[5] D.-J. Lee, S.-Y. Lee, J.-S. Bae, J.-G. Kang, K.-H. Kim, S.-S. Rhee, J.-H. Park, J.-S. Cho, J. Chung, and D.-C. Seo, "Effect of Volatile Fatty Acid Concentration on Anaerobic Degradation Rate from Field Anaerobic Digestion Facilities Treating Food Waste Leachate in South Korea," *Journal of Chemistry*, vol. 2015, pp. 1–9, 2015, doi: 10.1155/2015/640717.

[6] H. Sun, J. Guo, S. Wu, F. Liu, and R. Dong, "Development and validation of a simplified titration method for monitoring volatile fatty acids in anaerobic digestion," *Waste management*, vol. 67, pp. 43–50, 2017, doi: 10.1016/j.wasman.2017.05.015.

[7] B. K. Ahring, M. Sandberg, and I. Angelidaki, "Volatile fatty acids as indicators of process imbalance in anaerobic digestors," *Applied Microbiology and Biotechnology*, vol. 43, no. 3, pp. 559–565, 1995, doi: 10.1007/BF00218466.

[8] A. O. Wagner, C. Reitschuler, and P. Illmer, "Effect of different acetate:propionate ratios on the methanogenic community during thermophilic anaerobic digestion in batch experiments," *Biochemical Engineering Journal*, vol. 90, pp. 154–161, 2014, doi: 10.1016/j.bej.2014.05.014.

[9] P. Weiland, "Biogas production: current state and perspectives," *Applied Microbiology and Biotechnology*, vol. 85, no. 4, pp. 849–860, 2010, doi: 10.1007/s00253-009-2246-7.

[10] L. Martín-González, X. Font, and T. Vicent, "Alkalinity ratios to identify process imbalances in anaerobic digesters treating source-sorted organic fraction of municipal wastes," *Biochemical Engineering Journal*, vol. 76, pp. 1–5, 2013, doi: 10.1016/j.bej.2013.03.016.

[11] H. Nielsen, H. Uellendahl, and B. K. Ahring, "Regulation and optimization of the biogas process: Propionate as a key parameter," *Biomass and Bioenergy*, vol. 31, 11-12, pp. 820–830, 2007, doi: 10.1016/j.biombioe.2007.04.004.

[12] *EBIPREP*. [Online]. Available: www.ebiprep.eu (accessed: Jun. 12 2023).

[13] B. Ojha, M. Schober, S. Turad, J. Jochum, and H. Kohler, "Gasification of Biomass: The Very Sensitive Monitoring of Tar in Syngas by the Determination of the Oxygen Demand—A Proof of Concept," *Processes*, vol. 10, no. 7, p. 1270, 2022, doi: 10.3390/pr10071270.

[14] N. J. Pineau, F. Krumeich, A. T. Güntner, and S. E. Pratsinis, "Y-doped ZnO films for acetic acid sensing down to ppb at high humidity," *Sensors and Actuators B: Chemical*, vol. 327, p. 128843, 2021, doi: 10.1016/j.snb.2020.128843.

[15] V. Ambardekar, T. Bhowmick, P. P. Bandyopadhyay, and S. B. Majumder, "Understanding on the effect of morphology towards the hydrogen and carbon monoxide sensing characteristics of tin oxide sensing elements," *International Journal of Hydrogen Energy*, vol. 46, no. 44, pp. 23113–23123, 2021, doi: 10.1016/j.ijhydene.2021.04.085.

[16] J. Knoblauch, N. Illyaskutty, and H. Kohler, "Early detection of fires in electrical installations by thermally modulated SnO2/additive-multi sensor arrays," *Sensors and Actuators B: Chemical*, vol. 217, pp. 36–40, 2015, doi: 10.1016/j.snb.2015.02.014.

[17] B. Ojha, N. Illyaskutty, J. Knoblauch, M. R. Balachandran, and H. Kohler, "High-temperature CO / HC gas sensors to optimize firewood combustion in low-power fireplaces," *Journal of Sensors and Sensor Systems*, vol. 6, no. 1, pp. 237–246, 2017, doi: 10.5194/jsss-6-237-2017.

[18] V. Galstyan, M. Bhandari, V. Sberveglieri, G. Sberveglieri, and E. Comini, "Metal Oxide Nanostructures in Food Applications: Quality Control and Packaging," *Chemosensors*, vol. 6, no. 2, p. 16, 2018, doi: 10.3390/chemosensors6020016.

[19] P. J. D. Peterson, A. Aujla, K. H. Grant, A. G. Brundle, M. R. Thompson, J. Vande Hey, and R. J. Leigh, "Practical Use of Metal Oxide Semiconductor Gas Sensors for Measuring Nitrogen Dioxide and Ozone in Urban Environments," *Sensors*, vol. 17, no. 7, 2017, doi: 10.3390/s17071653.

[20] N. Yamazoe, "Toward innovations of gas sensor technology," *Sensors and Actuators B: Chemical*, vol. 108, 1-2, pp. 2–14, 2005, doi: 10.1016/j.snb.2004.12.075.

[21] A. T. Güntner, S. Abegg, K. Königstein, P. A. Gerber, A. Schmidt-Trucksäss, and S. E. Pratsinis, "Breath Sensors for Health Monitoring," *ACS sensors*, vol. 4, no. 2, pp. 268–280, 2019, doi: 10.1021/acssensors.8b00937.

[22] P. H. Rogers and S. Semancik, "Development of optimization procedures for application-specific chemical sensing," *Sensors and Actuators B: Chemical*, vol. 163, no. 1, pp. 8–19, 2012, doi: 10.1016/j.snb.2011.11.015.

[23] F. Sarf, "Metal Oxide Gas Sensors by Nanostructures," in *Gas Sensors*, S. Bahadar Khan, A. M. Asiri, and K. Akhtar, Eds.: IntechOpen, 2020.

[24] L. Gajdošík, "The concentration measurement with gas sensor operated in the dynamic regime," *Sensors and Actuators B: Chemical*, vol. 106, no. 2, pp. 691–699, 2005, doi: 10.1016/j.snb.2004.09.017.

[25] B. Sowmya, J. Athira, and P. K. Panda, "A review on metal-oxide based p-n and n-n heterostructured nano-materials for gas sensing applications," *Sensors International*, vol. 2, p. 100085, 2021, doi: 10.1016/j.sintl.2021.100085.

[26] J. F. McAleer, P. T. Moseley, J. O. W. Norris, D. E. Williams, and B. C. Tofield, "Tin dioxide gas sensors. Part 2.—The role of surface additives," *Journal of the Chemical Society, Faraday Transactions 1: Physical Chemistry in Condensed Phases*, vol. 84, no. 2, p. 441, 1988, doi: 10.1039/f19888400441.

[27] J. Walker, P. Karnati, S. A. Akbar, and P. A. Morris, "Selectivity mechanisms in resistive-type metal oxide heterostructural gas sensors," *Sensors and Actuators B: Chemical*, vol. 355, p. 131242, 2022, doi: 10.1016/j.snb.2021.131242.

[28] G. Eranna, B. C. Joshi, D. P. Runthala, and R. P. Gupta, "Oxide Materials for Development of Integrated Gas Sensors—A Comprehensive Review," *Critical Reviews in Solid State and Materials Sciences*, vol. 29, 3-4, pp. 111–188, 2004, doi: 10.1080/10408430490888977.

[29] C. Delpha, M. Siadat, and M. Lumbreras, "Discrimination of a refrigerant gas in a humidity controlled atmosphere by using modelling parameters," *Sensors and Actuators B: Chemical*, vol. 62, no. 3, pp. 226–232, 2000, doi: 10.1016/S0925-4005(99)00389-5.

[30] J. Getino, M. C. Horrillo, J. Gutiérrez, L. Arés, J. I. Robla, C. García, and I. Sayago, "Analysis of VOCs with a tin oxide sensor array," *Sensors and Actuators B: Chemical*, vol. 43, 1-3, pp. 200–205, 1997, doi: 10.1016/S0925-4005(97)00152-4.

[31] A. K. Srivastava, "Detection of volatile organic compounds (VOCs) using SnO2 gas-sensor array and artificial neural network," *Sensors and Actuators B: Chemical*, vol. 96, 1-2, pp. 24–37, 2003, doi: 10.1016/S0925-4005(03)00477-5.

[32] A. Shahid, J.-H. Choi, A. U. H. S. Rana, and H.-S. Kim, "Least Squares Neural Network-Based Wireless E-Nose System Using an SnO_2 Sensor Array," *Sensors (Basel, Switzerland)*, vol. 18, no. 5, 2018, doi: 10.3390/s18051446.

[33] E. Llobet, J. Brezmes, X. Vilanova, J. E. Sueiras, and X. Correig, "Qualitative and quantitative analysis of volatile organic compounds using transient and steady-state responses of a thick-film tin oxide gas sensor array," *Sensors and Actuators B: Chemical*, vol. 41, 1-3, pp. 13–21, 1997, doi: 10.1016/S0925-4005(97)80272-9.

[34] E. Llobet, R. Ionescu, S. Al-Khalifa, J. Brezmes, X. Vilanova, X. Correig, N. Barsan, and J. W. Gardner, "Multicomponent gas mixture analysis using a single tin oxide sensor and

dynamic pattern recognition," *IEEE Sensors J.*, vol. 1, no. 3, pp. 207–213, 2001, doi: 10.1109/JSEN.2001.954833.

[35] U. Weimar, K. D. Schierbaum, W. Göpel, and R. Kowalkowski, "Pattern recognition methods for gas mixture analysis: Application to sensor arrays based upon SnO2," *Sensors and Actuators B: Chemical*, vol. 1, 1-6, pp. 93–96, 1990, doi: 10.1016/0925-4005(90)80179-4.

[36] K. Frank, V. Magapu, V. Schindler, H. Kohler, H. B. Keller, and R. Seifert, "Chemical Analysis with Tin Oxide Gas Sensors: Choice of Additives, Method of Operation and Analysis of Numerical Signal," *Sensor Letters*, vol. 6, no. 6, pp. 908–911, 2008, doi: 10.1166/sl.2008.527.

[37] S. Nakata, H. Okunishi, and Y. Nakashima, "Distinction of gases with a semiconductor sensor under a cyclic temperature modulation with second-harmonic heating," *Sensors and Actuators B: Chemical*, vol. 119, no. 2, pp. 556–561, 2006, doi: 10.1016/j.snb.2006.01.009.

[38] A. Hetznecker, H. Kohler, U. Schönauer, and U. Guth, "Investigation of SnO2/Na+-ionic conductor composites for new gas sensitive layers," *Sensors and Actuators B: Chemical*, vol. 99, 2-3, pp. 373–383, 2004, doi: 10.1016/j.snb.2003.11.035.

[39] A. Lee, "Temperature modulation in semiconductor gas sensing," *Sensors and Actuators B: Chemical*, vol. 60, no. 1, pp. 35–42, 1999, doi: 10.1016/S0925-4005(99)00241-5.

[40] M. Roth, R. Hartinger, R. Faul, and H.-E. Endres, "Drift reduction of organic coated gas-sensors by temperature modulation," *Sensors and Actuators B: Chemical*, vol. 36, 1-3, pp. 358–362, 1996, doi: 10.1016/S0925-4005(97)80096-2.

[41] N. Illyaskutty, J. Knoblauch, M. Schwotzer, and H. Kohler, "Thermally modulated multi sensor arrays of SnO2/additive/electrode combinations for enhanced gas identification," *Sensors and Actuators B: Chemical*, vol. 217, pp. 2–12, 2015, doi: 10.1016/j.snb.2015.03.018.

[42] A. Schievano, G. D'Imporzano, and F. Adani, "Substituting energy crops with organic wastes and agro-industrial residues for biogas production," *Journal of environmental management*, vol. 90, no. 8, pp. 2537–2541, 2009, doi: 10.1016/j.jenvman.2009.01.013.

[43] D. A. Putri, R. R. Saputro, and Budiyono., "Biogas Production from Cow Manure," *International Journal of Renewable Energy Development*, vol. 1, no. 2, pp. 61–64, 2012.

[44] A. M. Pérez-Chávez, L. Mayer, and E. Albertó, "Mushroom cultivation and biogas production: A sustainable reuse of organic resources," *Energy for Sustainable Development*, vol. 50, pp. 50–60, 2019, doi: 10.1016/j.esd.2019.03.002.

[45] B. Dhungana, S. P. Lohani, and M. Marsolek, "Anaerobic Co-Digestion of Food Waste with Livestock Manure at Ambient Temperature: A Biogas Based Circular Economy and Sustainable Development Goals," *Sustainability*, vol. 14, no. 6, p. 3307, 2022, doi: 10.3390/su14063307.

[46] L. Deressa, S. Libsu, R. B. Chavan, D. Manaye, and A. Dabassa, "Production of Biogas from Fruit and Vegetable Wastes Mixed with Different Wastes," *Environment and Ecology Research*, vol. 3, no. 3, pp. 65–71, 2015, doi: 10.13189/eer.2015.030303.

[47] N. H. Garcia, A. Mattioli, A. Gil, N. Frison, F. Battista, and D. Bolzonella, "Evaluation of the methane potential of different agricultural and food processing substrates for improved biogas production in rural areas," *Renewable and Sustainable Energy Reviews*, vol. 112, pp. 1–10, 2019, doi: 10.1016/j.rser.2019.05.040.

[48] D. T. Hill, S. A. Cobb, and J. P. Bolte, "Using Volatile Fatty Acid Relationships to Predict Anaerobic Digester Failure," *Transactions of the ASAE*, vol. 30, no. 2, pp. 496–501, 1987, doi: 10.13031/2013.31977.

[49] K. Boe, D. J. Batstone, and I. Angelidaki, "An innovative online VFA monitoring system for the anerobic process, based on headspace gas chromatography," *Biotechnology and Bioengineering*, vol. 96, no. 4, pp. 712–721, 2007, doi: 10.1002/bit.21131.

[50] A. Patel, A. Mahboubi, I. S. Horváth, M. J. Taherzadeh, U. Rova, P. Christakopoulos, and L. Matsakas, "Volatile Fatty Acids (VFAs) Generated by Anaerobic Digestion Serve as Feedstock for Freshwater and Marine Oleaginous Microorganisms to Produce Biodiesel and Added-Value Compounds," *Frontiers in microbiology*, vol. 12, p. 614612, 2021, doi: 10.3389/fmicb.2021.614612.

[51] A. T. Giduthuri and B. K. Ahring, "Current Status and Prospects of Valorizing Organic Waste via Arrested Anaerobic Digestion: Production and Separation of Volatile Fatty Acids," *Fermentation*, vol. 9, no. 1, p. 13, 2023, doi: 10.3390/fermentation9010013.

[52] K. Szacherska, P. Oleskowicz-Popiel, S. Ciesielski, and J. Mozejko-Ciesielska, "Volatile Fatty Acids as Carbon Sources for Polyhydroxyalkanoates Production," *Polymers*, vol. 13, no. 3, 2021, doi: 10.3390/polym13030321.

[53] B. J. J. Purser, S.-M. Thai, T. Fritz, S. R. Esteves, R. M. Dinsdale, and A. J. Guwy, "An improved titration model reducing over estimation of total volatile fatty acids in anaerobic digestion of energy crop, animal slurry and food waste," *Water research*, vol. 61, pp. 162–170, 2014, doi: 10.1016/j.watres.2014.05.020.

[54] M. J. Playne, "Determination of ethanol, volatile fatty acids, lactic and succinic acids in fermentation liquids by gas chromatography," *Journal of the Science of Food and Agriculture*, vol. 36, no. 8, pp. 638–644, 1985, doi: 10.1002/jsfa.2740360803.

[55] T. Becker, R. Kittsteiner-Eberle, T. Luck, and H.-L. Schmidt, "On-line determination of acetic acid in a continuous production of Acetobacter aceticus," *Journal of Biotechnology*, vol. 31, no. 3, pp. 267–275, 1993, doi: 10.1016/0168-1656(93)90073-V.

[56] N. Tippkötter, A. Deterding, and R. Ulber, "Determination of Acetic Acid in Fermentation Broth by Gas-Diffusion Technique," *Engineering in Life Sciences*, vol. 8, no. 1, pp. 62–67, 2008, doi: 10.1002/elsc.200820227.

[57] C. Wolf, D. Gaida, A. Stuhlsatz, S. McLoone, and M. Bongards, "Organic Acid Prediction in Biogas Plants Using UV/vis Spectroscopic Online-Measurements," in *Communications in Computer and Information Science, Life System Modeling and Intelligent Computing*, K. Li, X. Li, S. Ma, and G. W. Irwin, Eds., Berlin, Heidelberg: Springer, Berlin, Heidelberg, 2010, pp. 200–206.

[58] H. F. Jacobi, C. R. Moschner, and E. Hartung, "Use of near infrared spectroscopy in monitoring of volatile fatty acids in anaerobic digestion," *Water Science and Technology*, vol. 60, no. 2, pp. 339–346, 2009, doi: 10.2166/wst.2009.345.

[59] Andrea Stockl, Daniel Loeffler, Hans Oechsner, Thomas Jungbluth, Klaus Fischer, and Martin Kranert, "Near-infrared-reflection spectroscopy as measuring method to determine the state of the process for automatic control of anaerobic digestion," *International Journal of Agricultural and Biological Engineering*, vol. 6, no. 2, pp. 63–72, 2013, doi: 10.25165/ijabe.v6i2.732.

[60] E. Palacio-Barco, F. Robert-Peillard, J.-L. Boudenne, and B. Coulomb, "On-line analysis of volatile fatty acids in anaerobic treatment processes," *Analytica chimica acta*, vol. 668, no. 1, pp. 74–79, 2010, doi: 10.1016/j.aca.2009.12.019.

[61] X. Jin, X. Li, N. Zhao, I. Angelidaki, and Y. Zhang, "Bio-electrolytic sensor for rapid monitoring of volatile fatty acids in anaerobic digestion process," *Water research*, vol. 111, pp. 74–80, 2017, doi: 10.1016/j.watres.2016.12.045.

[62] D. L. Röhlen, J. Pilas, M. Dahmen, M. Keusgen, T. Selmer, and M. J. Schöning, "Toward a Hybrid Biosensor System for Analysis of Organic and Volatile Fatty Acids in Fermentation Processes," *Frontiers in chemistry*, vol. 6, p. 284, 2018, doi: 10.3389/fchem.2018.00284.

[63] B. Ojha, M. Aleksandrova, M. Schwotzer, M. Franzreb, and H. Kohler, "Thermo-cyclically operated metal oxide gas sensor arrays for analysis of dissolved volatile organic compounds in fermentation processes: Part I – Morphology aspects of the sensing behavior," *Sensing and Bio-Sensing Research*, vol. 40, p. 100558, 2023, doi: 10.1016/j.sbsr.2023.100558.

[64] S. Turad, A. Wilke, and J. Jochum, "Increasing efficiency and profitability of biogas plants by reducing the residence time and using a waste material-wood juice," in *Proceedings of 6th International Environmental Best Practices Conference, 24-26 September 2019*, University of Warmia and Mazury, Olsztyn, Poland, 2019, p. 181.

[65] M. E. Franke, T. J. Koplin, and U. Simon, "Metal and metal oxide nanoparticles in chemiresistors: does the nanoscale matter?," *Small*, vol. 2, no. 1, pp. 36–50, 2006, doi: 10.1002/smll.200500261.

[66] T. Toupance, O. Babot, B. Jousseaume, and G. Vilaça, "Nanocrystalline Mesoporous Tin Dioxide Prepared by the Sol−Gel Route from a Dialkoxydi(β-Diketonato)tin Complex," *Chemistry of Materials*, vol. 15, no. 24, pp. 4691–4697, 2003, doi: 10.1021/cm0344459.

[67] G. Korotcenkov, "The role of morphology and crystallographic structure of metal oxides in response of conductometric-type gas sensors," *Materials Science and Engineering: R: Reports*, vol. 61, 1-6, pp. 1–39, 2008, doi: 10.1016/j.mser.2008.02.001.

[68] G. B. González, "Investigating the Defect Structures in Transparent Conducting Oxides Using X-ray and Neutron Scattering Techniques," *Materials (Basel, Switzerland)*, vol. 5, no. 5, pp. 818–850, 2012, doi: 10.3390/ma5050818.

[69] B. Kamp, R. Merkle, and J. Maier, "Chemical diffusion of oxygen in tin dioxide," *Sensors and Actuators B: Chemical*, vol. 77, 1-2, pp. 534–542, 2001, doi: 10.1016/S0925-4005(01)00694-3.

[70] J. F. McAleer, P. T. Moseley, J. O. W. Norris, and D. E. Williams, "Tin dioxide gas sensors. Part 1.—Aspects of the surface chemistry revealed by electrical conductance variations," *Journal of the Chemical Society, Faraday Transactions 1: Physical Chemistry in Condensed Phases*, vol. 83, no. 4, p. 1323, 1987, doi: 10.1039/F19878301323.

[71] D. Kohl, "Surface processes in the detection of reducing gases with SnO2-based devices," *Sensors and Actuators*, vol. 18, no. 1, pp. 71–113, 1989, doi: 10.1016/0250-6874(89)87026-X.

[72] P. Atkins and P. Julio de, *Atkin's Physical Chemistry*, 8th ed.: W. H. Freeman and Company, 2006.

[73] J. Watson, "The tin oxide gas sensor and its applications," *Sensors and Actuators*, vol. 5, no. 1, pp. 29–42, 1984, doi: 10.1016/0250-6874(84)87004-3.

[74] N. Barsan and U. Weimar, "Conduction Model of Metal Oxide Gas Sensors," *Journal of Electroceramics*, vol. 7, no. 3, pp. 143–167, 2001, doi: 10.1023/A:1014405811371.

[75] M. Batzill, "Surface Science Studies of Gas Sensing Materials: SnO2," *Sensors*, vol. 6, no. 10, pp. 1345–1366, 2006, doi: 10.3390/s6101345.

[76] S. Morrison, "Selectivity in semiconductor gas sensors," *Sensors and Actuators*, vol. 12, no. 4, pp. 425–440, 1987, doi: 10.1016/0250-6874(87)80061-6.

[77] I. Langmuir, "The adsorption of gases on plane surfaces of glass, mica and platinum," *Journal of the American Chemical Society*, vol. 40, no. 9, pp. 1361–1403, 1918, doi: 10.1021/ja02242a004.

[78] P. Mora-Briseño, G. Jiménez-García, C.-O. Castillo-Araiza, H. González-Rodríguez, R. Huirache-Acuña, and R. Maya-Yescas, "Mars van Krevelen Mechanism for the Selective Partial Oxidation of Ethane," *International Journal of Chemical Reactor Engineering*, vol. 17, no. 7, 2019, doi: 10.1515/ijcre-2018-0085.

[79] Z.-Z. Pan, Y. Li, Y. Zhao, C. Zhang, and H. Chen, "Bulk phase charge transfer in focus – And in sequential along with surface steps," *Catalysis Today*, vol. 364, pp. 2–6, 2021, doi: 10.1016/j.cattod.2020.09.023.

[80] J. Tamaki, T. Hayashi, Y. Yamamoto, and M. Matsuoka, "Detection of Aliphatic Carboxylic Acids Using Tin Oxide Based Gas Sensors," *Electrochemistry*, vol. 71, no. 6, pp. 468–474, 2003, doi: 10.5796/electrochemistry.71.468.

[81] P. Manjunathan and G. V. Shanbhag, "Application of tin oxide-based materials in catalysis," in *Tin Oxide Materials*: Elsevier, 2020, pp. 519–553.

[82] H.-Y. Xu, Z.-R. Chen, C.-Y. Liu, Q. Ye, X.-P. Yang, J.-Q. Wang, and B.-Q. Cao, "Preparation of {200} crystal faced SnO2 nanorods with extremely high gas sensitivity at lower temperature," *Rare Metals*, vol. 40, no. 8, pp. 2004–2016, 2021, doi: 10.1007/s12598-021-01720-5.

[83] X. Bai, Z. Li, C. Yang, J. Fang, J. Liu, Y. Zhang, D. Wang, and Y. Qie, "Study on gas sensitive behavior of SnO2(221) and (110) crystal planes," *Vacuum*, vol. 218, p. 112648, 2023, doi: 10.1016/j.vacuum.2023.112648.

[84] D. Degler, U. Weimar, and N. Barsan, "Current Understanding of the Fundamental Mechanisms of Doped and Loaded Semiconducting Metal-Oxide-Based Gas Sensing Materials," *ACS sensors*, vol. 4, no. 9, pp. 2228–2249, 2019, doi: 10.1021/acssensors.9b00975.

[85] D. Filatova and M. Rumyantseva, "Additives in Nanocrystalline Tin Dioxide: Recent Progress in the Characterization of Materials for Gas Sensor Applications," *Materials (Basel, Switzerland)*, vol. 16, no. 20, 2023, doi: 10.3390/ma16206733.

[86] N. Yamazoe, "New approaches for improving semiconductor gas sensors," *Sensors and Actuators B: Chemical*, vol. 5, 1-4, pp. 7–19, 1991, doi: 10.1016/0925-4005(91)80213-4.

[87] D. Koziej, N. Bârsan, U. Weimar, J. Szuber, K. Shimanoe, and N. Yamazoe, "Water–oxygen interplay on tin dioxide surface: Implication on gas sensing," *Chemical Physics Letters*, vol. 410, 4-6, pp. 321–323, 2005, doi: 10.1016/j.cplett.2005.05.107.

[88] N. Bârsan, M. Huebner, and U. Weimar, "Conduction mechanism in semiconducting metal oxide sensing films: impact on transduction," in *Semiconductor Gas Sensors*, R. Jaaniso and O. K. Tan, Eds.: Woodhead Publishing, an imprint of Elsevier, 2020, pp. 39–69.

[89] N. Barsan, M. Schweizer-Berberich, and W. Göpel†, "Fundamental and practical aspects in the design of nanoscaled SnO 2 gas sensors: a status report," *Fresenius' Journal of Analytical Chemistry*, vol. 365, no. 4, pp. 287–304, 1999, doi: 10.1007/s002160051490.

[90] G. Eranna, *Metal oxide nanostructures as gas sensing devices*, 1st ed.: CRC Press, 2016.

[91] C. Xu, J. Tamaki, N. Miura, and N. Yamazoe, "Grain size effects on gas sensitivity of porous SnO2-based elements," *Sensors and Actuators B: Chemical*, vol. 3, no. 2, pp. 147–155, 1991, doi: 10.1016/0925-4005(91)80207-Z.

[92] G. Neri, "First Fifty Years of Chemoresistive Gas Sensors," *Chemosensors*, vol. 3, no. 1, pp. 1–20, 2015, doi: 10.3390/chemosensors3010001.

[93] D. Kohl, "The role of noble metals in the chemistry of solid-state gas sensors," *Sensors and Actuators B: Chemical*, vol. 1, 1-6, pp. 158–165, 1990, doi: 10.1016/0925-4005(90)80193-4.

[94] N. Yamazoe, Y. Kurokawa, and T. Seiyama, "Effects of additives on semiconductor gas sensors," *Sensors and Actuators*, vol. 4, pp. 283–289, 1983, doi: 10.1016/0250-6874(83)85034-3.

[95] N. Yamazoe and K. Shimanoe, "Theory of power laws for semiconductor gas sensors," *Sensors and Actuators B: Chemical*, vol. 128, no. 2, pp. 566–573, 2008, doi: 10.1016/j.snb.2007.07.036.

[96] J. W. Gardner, "A non-linear diffusion-reaction model of electrical conduction in semiconductor gas sensors," *Sensors and Actuators B: Chemical*, vol. 1, 1-6, pp. 166–170, 1990, doi: 10.1016/0925-4005(90)80194-5.

[97] D. E. Williams and K. F. Pratt, "Microstructure effects on the response of gas-sensitive resistors based on semiconducting oxides," *Sensors and Actuators B: Chemical*, vol. 70, 1-3, pp. 214–221, 2000, doi: 10.1016/S0925-4005(00)00572-4.

[98] N. Barsan and U. Weimar, "Understanding the fundamental principles of metal oxide based gas sensors; the example of CO sensing with SnO2 sensors in the presence of humidity," *Journal of Physics: Condensed Matter*, vol. 15, no. 20, R813-R839, 2003, doi: 10.1088/0953-8984/15/20/201.

[99] Y. Fu, Y. Jiang, S. Poizeau, A. Dutta, A. Mohanram, J. D. Pietras, and M. Z. Bazant, "Multicomponent Gas Diffusion in Porous Electrodes," *J. Electrochem. Soc.*, vol. 162, no. 6, F613-F621, 2015, doi: 10.1149/2.0911506jes.

[100] W. M. Sears, K. Colbow, and F. Consadori, "General characteristics of thermally cycled tin oxide gas sensors," *Semiconductor Science and Technology*, vol. 4, no. 5, pp. 351–359, 1989, doi: 10.1088/0268-1242/4/5/004.

[101] K. Frank, H. Kohler, and U. Guth, "Influence of the measurement conditions on the sensitivity of SnO2 gas sensors operated thermo-cyclically," *Sensors and Actuators B: Chemical*, vol. 141, no. 2, pp. 361–369, 2009, doi: 10.1016/j.snb.2009.07.001.

[102] J. Knoblauch, K. Murugavel, H. Kohler, and U. Guth, "Separation of Sensitivity Contributions in Tin Oxide Thick Film Sensors by Transmission Line Model Measurements at Isothermal and Thermally Modulated Operation," in *Proceedings of Eurosensors 2017, Paris, France, 3–6 September 2017*, p. 476.

[103] W. M. Sears, K. Colbow, R. Slamka, and F. Consadori, "Surface adsorption and gas consumption in restricted flow, thermally driven, gas sensors," *Semiconductor Science and Technology*, vol. 5, no. 1, pp. 45–53, 1990, doi: 10.1088/0268-1242/5/1/005.

[104] S. Nakata, E. Ozaki, and N. Ojima, "Gas sensing based on the dynamic nonlinear responses of a semiconductor gas sensor: dependence on the range and frequency of a

cyclic temperature change," *Analytica chimica acta*, vol. 361, 1-2, pp. 93–100, 1998, doi: 10.1016/s0003-2670(98)00013-0.

[105] A. Heilig, N. Bârsan, U. Weimar, M. Schweizer-Berberich, J. W. Gardner, and W. Göpel, "Gas identification by modulating temperatures of SnO2-based thick film sensors," *Sensors and Actuators B: Chemical*, vol. 43, 1-3, pp. 45–51, 1997, doi: 10.1016/S0925-4005(97)00096-8.

[106] H. Kohler, J. Röber, N. Link, and I. Bouzid, "New applications of tin oxide gas sensors: I. Molecular identification by cyclic variation of the working temperature and numerical analysis of the signals," *Sensors and Actuators B: Chemical*, vol. 61, 1-3, pp. 163–169, 1999, doi: 10.1016/S0925-4005(99)00286-5.

[107] A. Jerger, H. Kohler, F. Becker, H. B. Keller, and R. Seifert, "New applications of tin oxide gas sensors," *Sensors and Actuators B: Chemical*, vol. 81, 2-3, pp. 301–307, 2002, doi: 10.1016/S0925-4005(01)00970-4.

[108] Y. Kato, K. Yoshikawa, and M. Kitora, "Temperature-dependent dynamic response enables the qualification and quantification of gases by a single sensor," *Sensors and Actuators B: Chemical*, vol. 40, no. 1, pp. 33–37, 1997, doi: 10.1016/S0925-4005(97)80196-7.

[109] X. Huang, F. Meng, Z. Pi, W. Xu, and J. Liu, "Gas sensing behavior of a single tin dioxide sensor under dynamic temperature modulation," *Sensors and Actuators B: Chemical*, vol. 99, 2-3, pp. 444–450, 2004, doi: 10.1016/j.snb.2003.12.013.

[110] M. Schweizer-Berberich, M. Zdralek, U. Weimar, W. Göpel, T. Viard, D. Martinez, A. Seube, and A. Peyre-Lavigne, "Pulsed mode of operation and artificial neural network evaluation for improving the CO selectivity of SnO2 gas sensors," *Sensors and Actuators B: Chemical*, vol. 65, 1-3, pp. 91–93, 2000, doi: 10.1016/S0925-4005(99)00333-0.

[111] T. Amamoto, T. Yamaguch, Y. Matsuura, and Y. Kajiyama, "Development of pulse-drive semiconductor gas sensor," *Sensors and Actuators B: Chemical*, vol. 14, 1-3, pp. 587–588, 1993, doi: 10.1016/0925-4005(93)85103-h.

[112] Z. Ankara, T. Kammerer, A. Gramm, and A. Schütze, "Low power virtual sensor array based on a micromachined gas sensor for fast discrimination between H2, CO and relative humidity," *Sensors and Actuators B: Chemical*, vol. 100, 1-2, pp. 240–245, 2004, doi: 10.1016/j.snb.2003.12.072.

[113] A. Vergara, E. Llobet, J. Brezmes, P. Ivanov, X. Vilanova, I. Gracia, C. Cané, and X. Correig, "Optimised temperature modulation of metal oxide micro-hotplate gas sensors through multilevel pseudo random sequences," *Sensors and Actuators B: Chemical*, 111-112, pp. 271–280, 2005, doi: 10.1016/j.snb.2005.06.039.

[114] X. Huang, J. Liu, D. Shao, Z. Pi, and Z. Yu, "Rectangular mode of operation for detecting pesticide residue by using a single SnO2-based gas sensor," *Sensors and Actuators B: Chemical*, vol. 96, no. 3, pp. 630–635, 2003, doi: 10.1016/j.snb.2003.07.006.

[115] J. Ding, T. J. McAvoy, R. E. Cavicchi, and S. Semancik, "Surface state trapping models for SnO2-based microhotplate sensors," *Sensors and Actuators B: Chemical*, vol. 77, no. 3, pp. 597–613, 2001, doi: 10.1016/s0925-4005(01)00765-1.

[116] S. Nakata, S. Akakabe, M. Nakasuji, and K. Yoshikawa, "Gas Sensing Based on a Nonlinear Response: Discrimination between Hydrocarbons and Quantification of Individual Components in a Gas Mixture," *Analytical chemistry*, vol. 68, no. 13, pp. 2067–2072, 1996, doi: 10.1021/ac9510954.

[117] B. Ojha, A. Wilke, R. Brämer, M. Franzreb, and H. Kohler, "Thermo-cyclically operated metal oxide gas sensor arrays for analysis of dissolved volatile organic compounds in fermentation processes: Part II – Quasi online monitoring in biogas fermentation," *Sensing and Bio-Sensing Research*, vol. 43, p. 100606, 2024, doi: 10.1016/j.sbsr.2023.100606.

[118] R. Seifert, H. B. Keller, and H. Kohler, "SimSens – A new mathematical procedure for simultaneous analysis of gases with resistive gas sensors," *Sensors and Actuators B: Chemical*, vol. 209, pp. 203–207, 2015, doi: 10.1016/j.snb.2014.10.133.

[119] R. Seifert, H. B. Keller, K. Frank, and H. Kohler, "ProSens—An Efficient Mathematical Procedure for Calibration and Evaluation of Tin Oxide Gas Sensor Data," *Sensor Letters*, vol. 9, no. 1, pp. 7–10, 2011, doi: 10.1166/sl.2011.1408.

[120] K. Haarstad, O. Bergersen, and R. Sørheim, "Occurrence of carbon monoxide during organic waste degradation," *Journal of the Air & Waste Management Association (1995)*, vol. 56, no. 5, pp. 575–580, 2006, doi: 10.1080/10473289.2006.10464470.

[121] A. Nsair, S. Onen Cinar, A. Alassali, H. Abu Qdais, and K. Kuchta, "Operational Parameters of Biogas Plants: A Review and Evaluation Study," *Energies*, vol. 13, no. 15, p. 3761, 2020, doi: 10.3390/en13153761.

[122] K. Boe, "Online monitoring and control of the biogas process," Dissertation, Technical University of Denmark, 2006. [Online]. Available: https://www.osti.gov/etdeweb/biblio/20833720

[123] L. Appels, J. Baeyens, J. Degrève, and R. Dewil, "Principles and potential of the anaerobic digestion of waste-activated sludge," *Progress in Energy and Combustion Science*, vol. 34, no. 6, pp. 755–781, 2008, doi: 10.1016/j.pecs.2008.06.002.

[124] D. Platošová, J. Rusín, J. Platoš, K. Smutná, and R. Buryjan, "Case Study of Anaerobic Digestion Process Stability Detected by Dissolved Hydrogen Concentration," *Processes*, vol. 9, no. 1, p. 106, 2021, doi: 10.3390/pr9010106.

[125] M. H. Gerardi, Ed., *The Microbiology of Anaerobic Digesters*: John Wiley & Sons, Inc, 2003.

[126] S. Theuerl, J. Klang, and A. Prochnow, "Process Disturbances in Agricultural Biogas Production—Causes, Mechanisms and Effects on the Biogas Microbiome: A Review," *Energies*, vol. 12, no. 3, p. 365, 2019, doi: 10.3390/en12030365.

[127] R. F. Hickey and M. S. Switzenbaum, "The response and utility of hydrogen and carbon monoxide as process indicators of anaerobic digesters subject to organic and hydraulic overloads," *Research Journal of the Water Pollution Control Federation*, vol. 63, pp. 129–140, 1991.

[128] M. Bott and R. K. Thauer, "Proton-motive-force-driven formation of CO from CO2 and H2 in methanogenic bacteria," *European Journal of Biochemistry*, vol. 168, no. 2, pp. 407–412, 1987, doi: 10.1111/j.1432-1033.1987.tb13434.x.

[129] R. F. Hickey and M. S. Switzenbaum, "Behavior of carbon monoxide as a trace component of anaerobic digester gases and methanogenesis from acetate," *Environmental Science & Technology*, vol. 24, no. 11, pp. 1642–1648, 1990, doi: 10.1021/es00081a003.

[130] I. Angelidaki, L. Ellegaard, and B. K. Ahring, "A mathematical model for dynamic simulation of anaerobic digestion of complex substrates: focusing on ammonia inhibition," *Biotechnology and Bioengineering*, vol. 42, no. 2, pp. 159–166, 1993, doi: 10.1002/bit.260420203.

[131] A. Costa, F. Maria Tangorra, M. Zaninelli, R. Oberti, A. Guidobono Cavalchini, G. Savoini, and M. Lazzari, "Evaluating an e-nose ability to detect biogas plant efficiency: a case study," *Italian Journal of Animal Science*, vol. 15, no. 1, pp. 116–123, 2016, doi: 10.1080/1828051X.2016.1147930.

[132] A. Diéguez, A. Romano-Rodríguez, J. R. Morante, J. Kappler, N. Bârsan, and W. Göpel, "Nanoparticle engineering for gas sensor optimisation: improved sol–gel fabricated nanocrystalline SnO2 thick film gas sensor for NO2 detection by calcination, catalytic metal introduction and grinding treatments," *Sensors and Actuators B: Chemical*, vol. 60, 2-3, pp. 125–137, 1999, doi: 10.1016/S0925-4005(99)00258-0.

[133] N. J. Pineau, S. D. Keller, A. T. Güntner, and S. E. Pratsinis, "Palladium embedded in SnO2 enhances the sensitivity of flame-made chemoresistive gas sensors," *Mikrochimica acta*, vol. 187, no. 1, p. 96, 2020, doi: 10.1007/s00604-019-4080-7.

[134] A. T. Güntner, N. J. Pineau, and S. E. Pratsinis, "Flame-made chemoresistive gas sensors and devices," *Progress in Energy and Combustion Science*, vol. 90, p. 100992, 2022, doi: 10.1016/j.pecs.2022.100992.

[135] H.-P. Hong, "Crystal structures and crystal chemistry in the system Na1+xZr2SixP3−xO12," *Materials Research Bulletin*, vol. 11, no. 2, pp. 173–182, 1976, doi: 10.1016/0025-5408(76)90073-8.

[136] H. Kohler and H. Schulz, "NASICON solid electrolytes part I: The Na+-diffusion path and its relation to the structure," *Materials Research Bulletin*, vol. 20, no. 12, pp. 1461–1471, 1985, doi: 10.1016/0025-5408(85)90164-3.

[137] H. Kohler and H. Schulz, "NASICON solid electrolytes Part II - X-ray diffraction experiments on sodium-zirconium-phosphate single crystals at 295K and at 993K," *Materials Research Bulletin*, vol. 21, no. 1, pp. 23–31, 1986, doi: 10.1016/0025-5408(86)90025-5.

[138] K.-D. Kreuer, H. Kohler, and J. Maier, "Sodium ion conductors with NASICON framework structure," in *High Conductivity Solid Ionic Conductors*, T. Takahashi, Ed.: World Scientific Publishing, 1989, pp. 242–279.

[139] M. Guin, F. Tietz, and O. Guillon, "New promising NASICON material as solid electrolyte for sodium-ion batteries: Correlation between composition, crystal structure and ionic conductivity of Na3+xSc2SixP3−xO12," *Solid State Ionics*, vol. 293, pp. 18–26, 2016, doi: 10.1016/j.ssi.2016.06.005.

[140] B. Zhang, K. Ma, X. Lv, K. Shi, Y. Wang, Z. Nian, Y. Li, L. Wang, L. Dai, and Z. He, "Recent advances of NASICON-Na3V2(PO4)3 as cathode for sodium-ion batteries: Synthesis, modifications, and perspectives," *Journal of Alloys and Compounds*, vol. 867, p. 159060, 2021, doi: 10.1016/j.jallcom.2021.159060.

[141] T. Maruyama, Y. Saito, Y. Matsumoto, and Y. Yano, "Potentiometric sensor for sulfur oxides using NASICON as a solid electrolyte," *Solid State Ionics*, vol. 17, no. 4, pp. 281–286, 1985, doi: 10.1016/0167-2738(85)90072-4.

[142] Wang, B., Liang, X. S., Liu, F. M., Zhong, T. G., Zhao, C., Lu, G. Y., & Quan, B. F., "Synthesis and characterization of NASICON nanoparticles by sol-gel method," *Chemical Research in Chinese Universities*, vol. 25, no. 1, pp. 13–16, 2009.

[143] A. Hetznecker, "Untersuchung der gassensitiven Eigenschaften von SnO2/NASICON-Kompositen," Dissertation, Faculty of Electrical and Computer Engineering, Technische Universität Dresden, 2005.

[144] I. Khan and P. Brimblecombe, "Henry's law constants of low molecular weight (<130) organic acids," *Journal of Aerosol Science*, vol. 23, pp. 897–900, 1992, doi: 10.1016/0021-8502(92)90556-B.

[145] J. R. Snider and G. A. Dawson, "Tropospheric light alcohols, carbonyls, and acetonitrile: Concentrations in the southwestern United States and Henry's Law data," *Journal of Geophysical Research*, vol. 90, D2, p. 3797, 1985, doi: 10.1029/JD090iD02p03797.

[146] A. H. Harvey and F. L. Smith, "Avoid common pitfalls when using Henry's law," *Chemical engineering progress*, vol. 103, no. 9, pp. 33–39, 2007.

[147] S. Ciesielski, E. O. Adu, J. Mozejko-Ciesielska, T. Pokoj, and A. Wilke, "Wood Juice Valorization through Production of Poly(3-hydroxybutyrate- co -3-hydroxyvalerate) Using Bacillus sp. G8_19," *ACS Sustainable Chem. Eng.*, vol. 9, no. 50, pp. 16870–16873, 2021, doi: 10.1021/acssuschemeng.1c06856.

[148] Q. Zhang, Q. Zhou, Y. Lu, Y. Shao, Y. Qi, X. Qi, G. Zhong, Y. Yang, L. Chen, and Y.-S. Hu, "Modification of NASICON Electrolyte and Its Application in Real Na-Ion Cells," *Engineering*, vol. 8, pp. 170–180, 2022, doi: 10.1016/j.eng.2021.04.028.

[149] B. J. McEntire, R. A. Bartlett, G. R. Miller, and R. S. Gordon, "Effect of Decomposition on the Densification and Properties of Nasicon Ceramic Electrolytes," *Journal of the*

American Ceramic Society, vol. 66, no. 10, pp. 738–742, 1983, doi: 10.1111/j.1151-2916.1983.tb10541.x.

[150] T. Becker, S. Ahlers, C. Bosch-v.Braunmühl, G. Müller, and O. Kiesewetter, "Gas sensing properties of thin- and thick-film tin-oxide materials," *Sensors and Actuators B: Chemical*, vol. 77, 1-2, pp. 55–61, 2001, doi: 10.1016/S0925-4005(01)00672-4.

[151] P. Montmeat, R. Lalauze, J.-P. Viricelle, G. Tournier, and C. Pijolat, "Model of the thickness effect of SnO2 thick film on the detection properties," *Sensors and Actuators B: Chemical*, vol. 103, 1-2, pp. 84–90, 2004, doi: 10.1016/j.snb.2004.04.039.

[152] F. S. Stone, "Chemisorption and Catalysis on Metallic Oxides," *Advances in Catalysis*, vol. 13, pp. 1–53, 1962, doi: 10.1016/S0360-0564(08)60285-0.

[153] A. Rothschild, Y. Komem, and N. Ashkenasy, "Quantitative evaluation of chemisorption processes on semiconductors," *Journal of Applied Physics*, vol. 92, no. 12, pp. 7090–7097, 2002, doi: 10.1063/1.1519946.

[154] S. Gomri, J.-L. Seguin, J. Guerin, and K. Aguir, "Adsorption–desorption noise in gas sensors: Modelling using Langmuir and Wolkenstein models for adsorption," *Sensors and Actuators B: Chemical*, vol. 114, no. 1, pp. 451–459, 2006, doi: 10.1016/j.snb.2005.05.033.

[155] A. Šetkus, "Heterogeneous reaction rate based description of the response kinetics in metal oxide gas sensors," *Sensors and Actuators B: Chemical*, vol. 87, no. 2, pp. 346–357, 2002, doi: 10.1016/S0925-4005(02)00269-1.

[156] Y. Kwon, H. Kim, S. Lee, I.-J. Chin, T.-Y. Seong, W. in Lee, and C. Lee, "Enhanced ethanol sensing properties of TiO2 nanotube sensors," *Sensors and Actuators B: Chemical*, vol. 173, pp. 441–446, 2012, doi: 10.1016/j.snb.2012.07.062.

[157] Z. El khalidi, B. Hartiti, M. Siadat, E. Comini, H. M. M. M. Arachchige, S. Fadili, and P. Thevenin, "Acetone sensor based on Ni doped ZnO nanostructues: growth and sensing capability," *Journal of Materials Science: Materials in Electronics*, vol. 30, no. 8, pp. 7681–7690, 2019, doi: 10.1007/s10854-019-01083-9.

[158] V. Khorramshahi, J. Karamdel, and R. Yousefi, "Acetic acid sensing of Mg-doped ZnO thin films fabricated by the sol–gel method," *Journal of Materials Science: Materials in Electronics*, vol. 29, no. 17, pp. 14679–14688, 2018, doi: 10.1007/s10854-018-9604-0.

[159] A. Mirzaei, S. G. Leonardi, and G. Neri, "Detection of hazardous volatile organic compounds (VOCs) by metal oxide nanostructures-based gas sensors: A review," *Ceramics International*, vol. 42, no. 14, pp. 15119–15141, 2016, doi: 10.1016/j.ceramint.2016.06.145.

[160] D. Kohl, W. Thoren, U. Schnakenberg, G. Schüll, and G. Heiland, "Decomposition of gaseous acetic acid on SnO 2," *Journal of the Chemical Society, Faraday Transactions*, vol. 87, no. 16, pp. 2647–2653, 1991, doi: 10.1039/FT9918702647.

[161] H. Gong, Y. J. Wang, S. C. Teo, and L. Huang, "Interaction between thin-film tin oxide gas sensor and five organic vapors," *Sensors and Actuators B: Chemical*, vol. 54, no. 3, pp. 232–235, 1999, doi: 10.1016/S0925-4005(99)00119-7.

[162] J. M. Vohs and M. A. Barteau, "Reaction pathways and intermediates in the decomposition of acetic and propionic acids on the polar surfaces of zinc oxide," *Surface Science*, vol. 201, no. 3, pp. 481–502, 1988, doi: 10.1016/0039-6028(88)90499-2.

[163] N. Mansir, H. Mohd Sidek, S. H. Teo, N.-A. Mijan, A. Ghassan Alsultan, C. H. Ng, M. R. Shamsuddin, and Y. H. Taufiq-Yap, "Catalytically active metal oxides studies for the conversion technology of carboxylic acids and bioresource based fatty acids to ketones: A review," *Bioresource Technology Reports*, vol. 17, p. 100988, 2022, doi: 10.1016/j.biteb.2022.100988.

[164] R. Pestman, R. M. Koster, A. van Duijne, J. Pieterse, and V. Ponec, "Reactions of Carboxylic Acids on Oxides: 2. Biomolecular Reaction of Aliphatic Acids to Ketones," *Journal of Catalysis*, vol. 168, no. 2, pp. 265–272, 1997, doi: 10.1006/jcat.1997.1624.

[165] G. Mekhemer, S. Halawy, M. Mohamed, and M. Zaki, "Ketonization of acetic acid vapour over polycrystalline magnesia: in situ Fourier transform infrared spectroscopy and kinetic studies," *Journal of Catalysis*, vol. 230, no. 1, pp. 109–122, 2005, doi: 10.1016/j.jcat.2004.09.030.

[166] S. T. Almutairi, E. F. Kozhevnikova, and I. V. Kozhevnikov, "Ketonisation of acetic acid on metal oxides: Catalyst activity, stability and mechanistic insights," *Applied Catalysis A: General*, vol. 565, pp. 135–145, 2018, doi: 10.1016/j.apcata.2018.08.008.

[167] K. Parida and H. K. Mishra, "Catalytic ketonisation of acetic acid over modified zirconia," *Journal of Molecular Catalysis A: Chemical*, vol. 139, no. 1, pp. 73–80, 1999, doi: 10.1016/S1381-1169(98)00184-8.

[168] Z.-F. Pei and V. Ponec, "On the intermediates of the acetic acid reactions on oxides: an IR study," *Applied Surface Science*, vol. 103, no. 2, pp. 171–182, 1996, doi: 10.1016/0169-4332(96)00453-9.

[169] E. J. Grootendorst, R. Pestman, R. M. Koster, and V. Ponec, "Selective Reduction of Acetic Acid to Acetaldehyde on Iron Oxides," *Journal of Catalysis*, vol. 148, no. 1, pp. 261–269, 1994, doi: 10.1006/jcat.1994.1207.

[170] R. Pestman, R. M. Koster, J. Pieterse, and V. Ponec, "Reactions of Carboxylic Acids on Oxides: 1. Selective Hydrogenation of Acetic Acid to Acetaldehyde," *Journal of Catalysis*, vol. 168, no. 2, pp. 255–264, 1997, doi: 10.1006/jcat.1997.1623.

[171] H. Onishi, Y. Yamaguchi, K. Fukui, and Y. Iwasawa, "Temperature-Jump STM Observation of Reaction Intermediate on Metal−Oxide Surfaces," *The Journal of Physical Chemistry*, vol. 100, no. 23, pp. 9582–9584, 1996, doi: 10.1021/jp960861n.

[172] K. S. Kim and M. A. Barteau, "Pathways for carboxylic acid decomposition on titania," *Langmuir*, vol. 4, no. 4, pp. 945–953, 1988, doi: 10.1021/la00082a028.

[173] T. Jinkawa, G. Sakai, J. Tamaki, N. Miura, and N. Yamazoe, "Relationship between ethanol gas sensitivity and surface catalytic property of tin oxide sensors modified with acidic or basic oxides," *Journal of Molecular Catalysis A: Chemical*, vol. 155, 1-2, pp. 193–200, 2000, doi: 10.1016/S1381-1169(99)00334-9.

[174] E. M. Cordi and J. L. Falconer, "Oxidation of Volatile Organic Compounds on Al2O3, Pd/Al2O3, and PdO/Al2O3Catalysts," *Journal of Catalysis*, vol. 162, no. 1, pp. 104–117, 1996, doi: 10.1006/jcat.1996.0264.

[175] C. O. Park and S. A. Akbar, "Ceramics for chemical sensing," *Journal of Materials Science*, vol. 38, no. 23, pp. 4611–4637, 2003, doi: 10.1023/A:1027402430153.

[176] T. Maekawa, J. Tamaki, N. Miura, N. Yamazoe, and S. Matsushima, "Development of SnO2-based ethanol gas sensor," *Sensors and Actuators B: Chemical*, vol. 9, no. 1, pp. 63–69, 1992, doi: 10.1016/0925-4005(92)80195-4.

[177] L. Shao-you, C. Yuan-dao, Z. Cheng-gang, O. Li-hui, Z. Wei-guo, and F. Qing-ge, "Solid-Phase Synthesis and Photocatalytic Property of Sulfur and Nickel Doped Tin Oxide Powder Materials by Isomeric Surfactant as Template," *Journal of Inorganic and Organometallic Polymers and Materials*, vol. 30, no. 2, pp. 457–468, 2020, doi: 10.1007/s10904-019-01204-1.

[178] N. Banerjee, B. Bhowmik, S. Roy, C. K. Sarkar, and P. Bhattacharyya, "Anomalous recovery characteristics of Pd modified ZnO nanorod based acetone sensor," *Journal of nanoscience and nanotechnology*, vol. 13, no. 10, pp. 6826–6834, 2013, doi: 10.1166/jnn.2013.7786.

[179] W. X. Jin, S. Y. Ma, Z. Z. Tie, J. J. Wei, J. Luo, X. H. Jiang, T. T. Wang, W. Q. Li, L. Cheng, and Y. Z. Mao, "One-step synthesis and highly gas-sensing properties of hierarchical Cu-doped SnO2 nanoflowers," *Sensors and Actuators B: Chemical*, vol. 213, pp. 171–180, 2015, doi: 10.1016/j.snb.2015.02.075.

[180] S. Shao, H. Wu, S. Wang, Q. Hong, R. Koehn, T. Wu, and W.-F. Rao, "Highly crystalline and ordered nanoporous SnO 2 thin films with enhanced acetone sensing property at room temperature," *Journal of Materials Chemistry C*, vol. 3, no. 41, pp. 10819–10829, 2015, doi: 10.1039/C5TC02188J.

[181] A. Hetznecker, H. Kohler, and U. Guth, "Enhanced studies on the mechanism of gas selectivity and electronic interactions of SnO2/Na+-ionic conductors," *Sensors and Actuators B: Chemical*, vol. 120, no. 2, pp. 378–385, 2007, doi: 10.1016/j.snb.2006.02.026.

[182] M. Saha, A. Banerjee, A. K. Halder, J. Mondal, A. Sen, and H. S. Maiti, "Effect of alumina addition on methane sensitivity of tin dioxide thick films," *Sensors and Actuators B: Chemical*, vol. 79, 2-3, pp. 192–195, 2001, doi: 10.1016/S0925-4005(01)00874-7.

[183] T. K. Phung, A. A. Casazza, B. Aliakbarian, E. Finocchio, P. Perego, and G. Busca, "Catalytic conversion of ethyl acetate and acetic acid on alumina as models of vegetable

oils conversion to biofuels," *Chemical Engineering Journal*, 215-216, pp. 838–848, 2013, doi: 10.1016/j.cej.2012.11.057.

[184] M. N. Tsampas, F. M. Sapountzi, and P. Vernoux, "Applications of yttria stabilized zirconia (YSZ) in catalysis," *Catalysis Science & Technology*, vol. 5, no. 11, pp. 4884–4900, 2015, doi: 10.1039/C5CY00739A.

APPENDIX

Appendix 1: Overview of different metal oxide/additive composites investigated in screening procedure.

S.N.	metal oxide/additive
1	SnO_2(FSP)
2	SnO_2(FSP)/SiO_2*
3	SnO_2(FSP)/Pd
4	SnO_2(FSP)/Alumina
5	SnO_2(FSP)/YSZ
6	SnO_2(FSP)/NASICON(x=2)
7	ZnO(FSP)/Y_2O_3
8	ZnO(SG)
9	ZnO(SG)/Y_2O_3
10	SnO_2(SG)/Alumina
11	SnO_2(SG)/YSZ
12	SnO_2(SG)/NASICON(x=2)
13	SnO_2(SG)/Y_2O_3

*Composite directly deposited on IDEs of sensor array chip by FSP technique

Each of these composites were transformed to a paste, dispensed on already prepared four-fold IDEs of a sensor-array chip, sintered, mounted on a TO8-housing, and then exposed to different volume of acetic acid extracted from the aqueous liquid phase via a carrier gas probe.

Appendix 2: Process details of fabrication of 4-fold sensor array chips.

A2.1: DC sputtering settings used for platinum deposition.

Working pressure / mbar	DC power / W	Duration / min
5×10^{-3}	200	6

A2.2: Process parameters used for photoresist (ma-P 1240, micro resist technology GmbH, Berlin) coating using WS-650Mz-23NPPB spin coater (Laurell Technologies, USA).

Rotation / rpm	Duration / s
2000	10

A2.3: Process parameters used for plasma etching using RIE etcher SI 591(SENTECH Instruments GmbH, Germany).

Duration / h		DC power / W
Heater side	IDE side	
3.25	3.5	100

A2.4: UV exposure dosage used for photolithography process using EVG 620 mask aligner (EV Group, Austria).

UV exposure dosage / $mJcm^{-2}$	300

Appendix 3: Absolute sensor response ∑(G-Go) of eight different sensitive layers

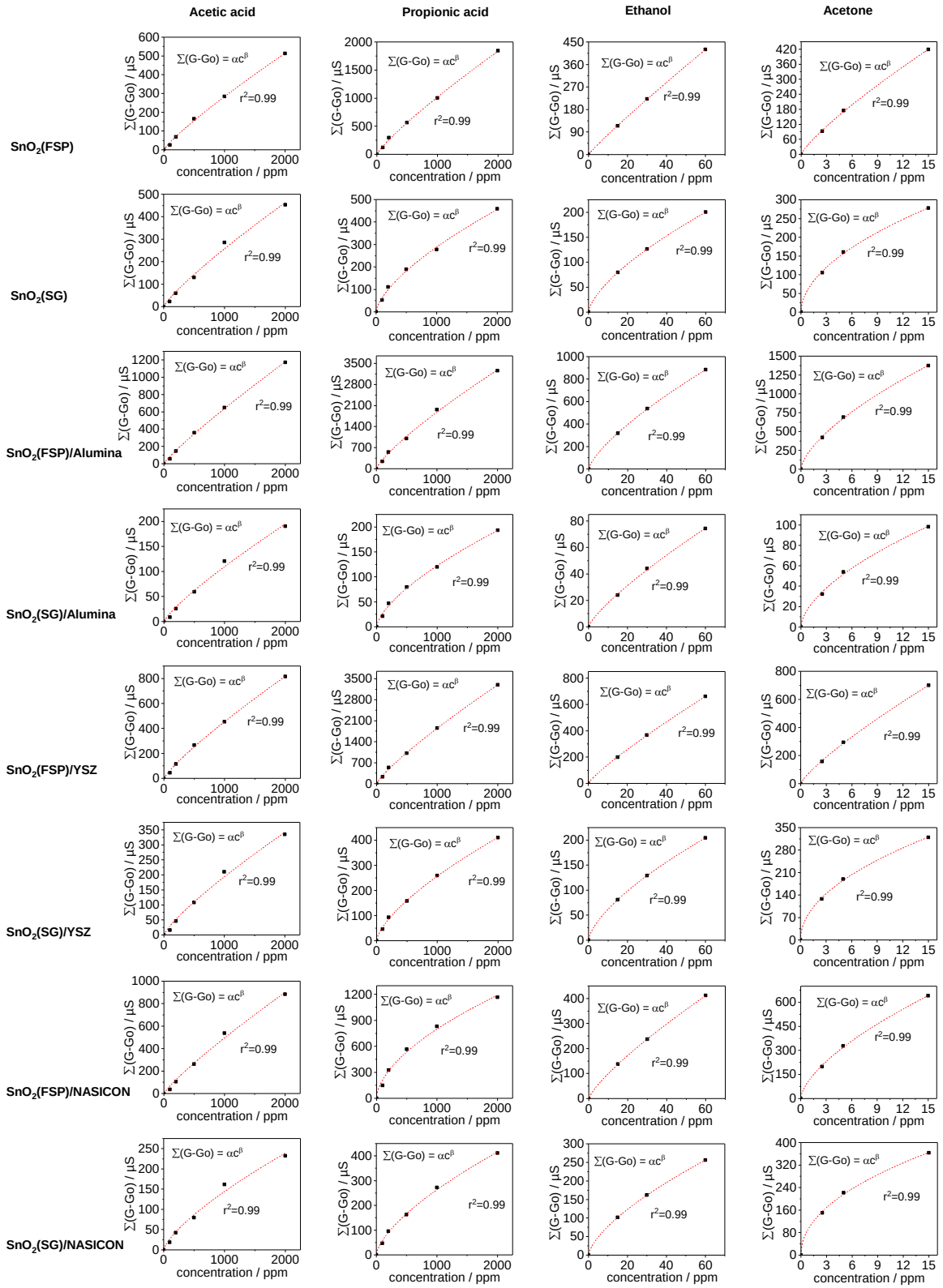

A3.1: Absolute sensor response ∑(G-Go) of eight different sensitive layers (in rows) vs. various concentrations of different VOCs (in column) dissolved in DI water at pH 3 condition.

Appendix 4: CTP integral and power law fit of different SnO_2/(additive)-layers of sensor arrays, SA#1 and SA#2, measured for fermentation samples with different manually dosed acetic acid concentrations.

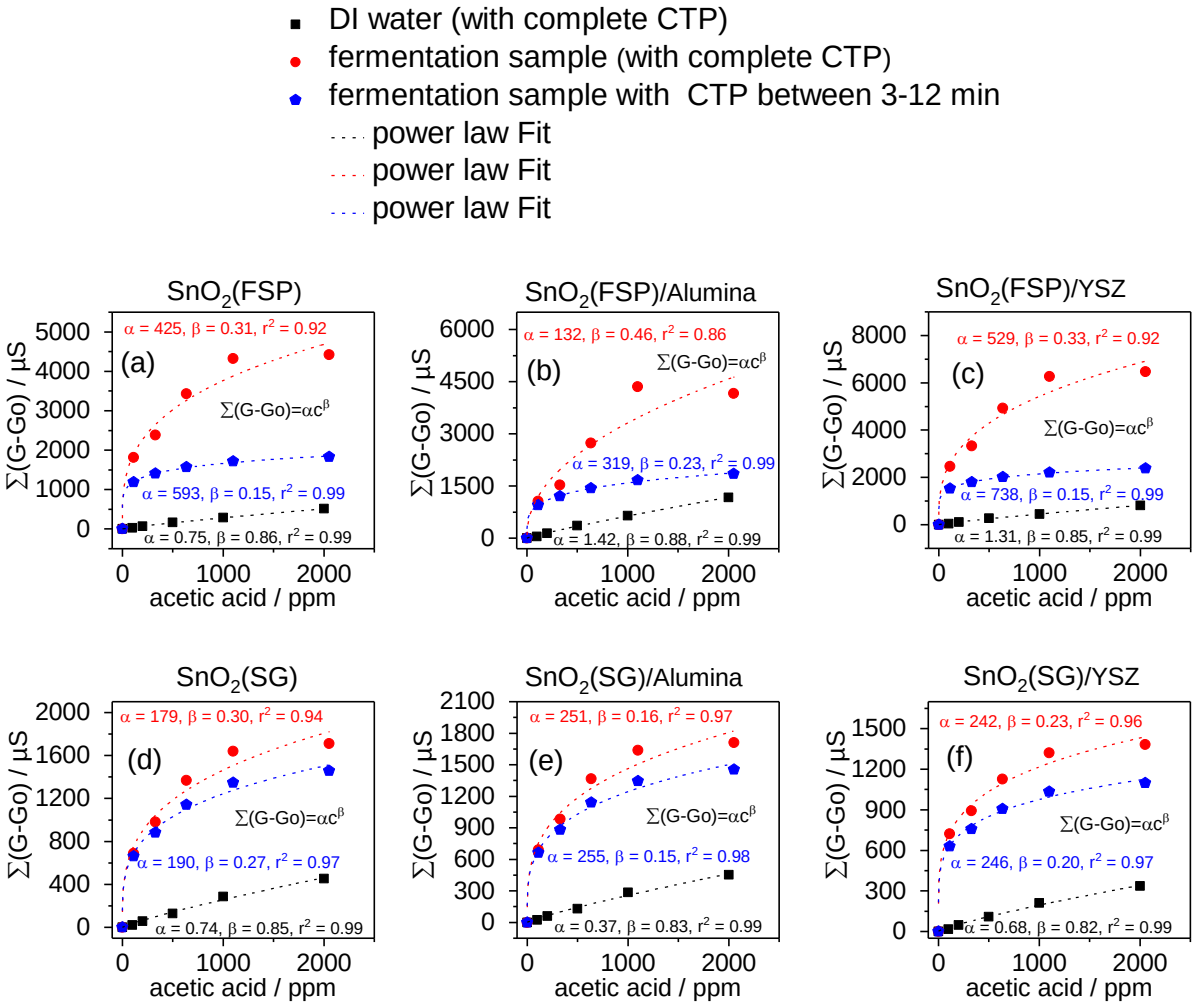

A4.1: CTP integral ∑(G-Go) of (a) SnO_2(FSP), (b) SnO_2(FSP)/Alumina, (c) SnO_2(FSP)/YSZ, (d) SnO_2(SG), (e) SnO_2(SG)/Alumina, (f) SnO_2(SG)/YSZ vs acetic acid concentration in DI water and fermentation sample. For the measurements with DI water, Go is the CTP measured at pH 7, whereas for the measurements with fermentation sample, Go is the CTP measured at pH8@3h (Fig. 52). Acidic acid concentration in fermentation sample was verified by GC analysis.

Appendix 5: Sensor response of different SnO_2/additive-layers of sensor arrays, SA#P and SA#T, over time at different pH conditions of the fermentation sample (#1).

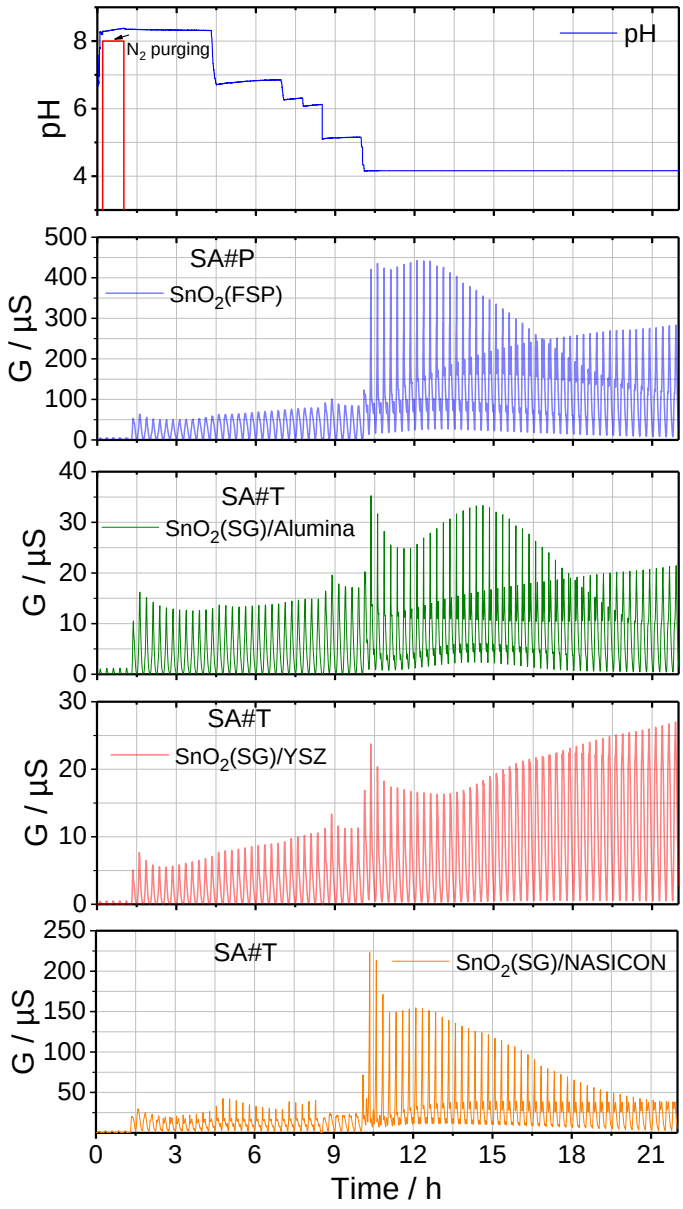

A5.1: Sensor response of SnO_2(FSP), SnO_2(SG)/Alumina, and SnO_2(SG)/YSZ, SnO_2(SG)/NASICON over time at different pH conditions of the fermentation sample.

After purging of the fermentation sample with N_2 (0.2-0.8 h) at pH 8.2, pH of the sample was gradually reduced to 4.4 in multiple steps (8.2→6.75→6.3→6→5→4.2) by the dosage of phosphoric acid. Transition from pH 5 to 4.2 triggered the gas development as indicated by the sharp increase of the response of all the SnO_2/additive-layers.

Appendix 6: Sensor response of different SnO_2/additive-layers of sensor arrays, SA#P and SA#T, over time at different pH conditions of the fermentation sample (#2).

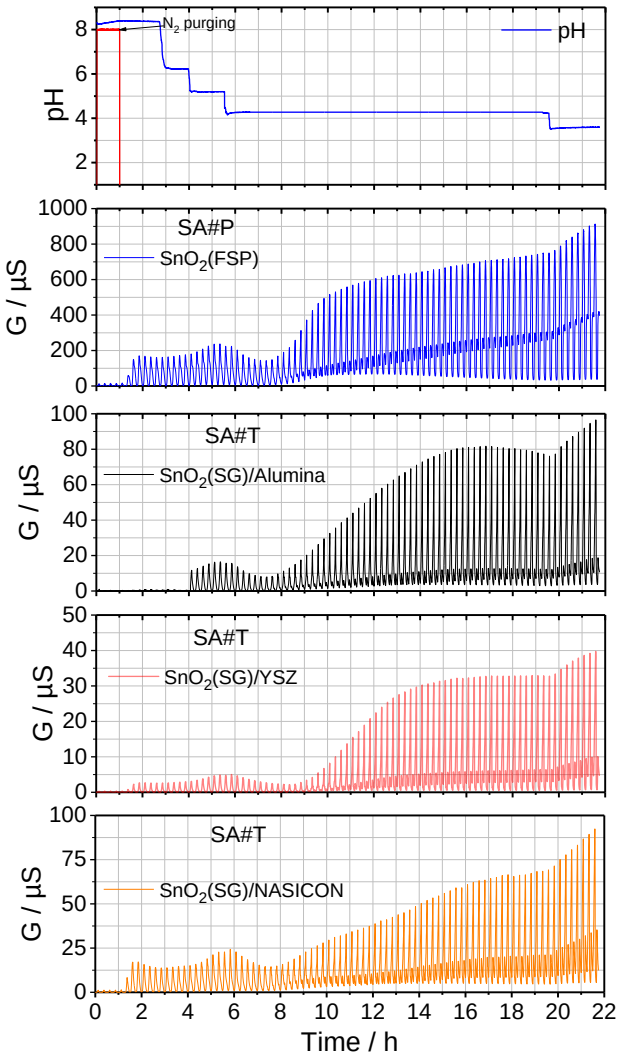

A6.1: Sensor response of SnO_2(FSP), SnO_2(SG)/Alumina, and SnO_2(SG)/YSZ, SnO_2(SG)/NASICON over time at different pH conditions of the fermentation sample.

After purging of the fermentation sample with N_2 (0.2-1 h) at pH 8.2, pH of the sample was gradually reduced to 3.5 in multiple steps (8.2→6.2→5.5→4→3.5) by the dosage of phosphoric acid. Gas development was observed at 8 h as indicated by the continuous increase of the response of all the SnO_2/additive-layers.

Appendix 7: Sensor response of different SnO_2/additive-layers of sensor array, SA#W, over time at different pH conditions of the fermentation sample (#3).

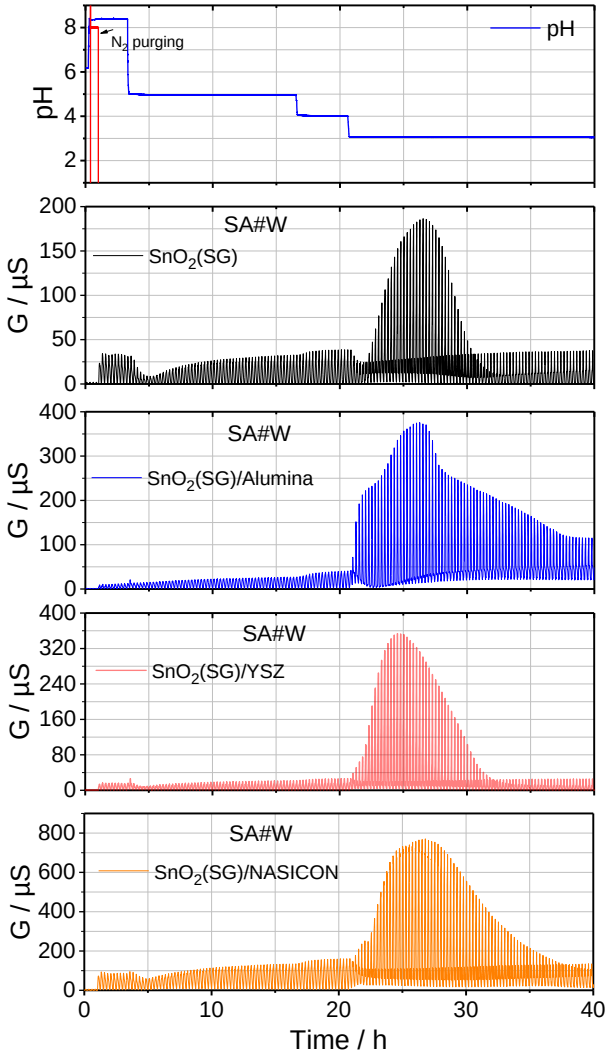

A7.1: Sensor response of SnO_2(SG), SnO_2(SG)/Alumina, and SnO_2(SG)/YSZ, SnO_2(SG)/NASICON over time at different pH conditions of the fermentation sample.

After purging of the fermentation sample with N_2 (0.3-1 h) at pH 8.4, pH of the sample was gradually reduced to 3 in multiple steps (8.4→5→4→3), but in less steps compared to experiments shown in A5 and A6, by the dosage of phosphoric acid. After transition of pH to 3 from 4, gas development was observed at 21 h as indicated by the continuous increase of the response of all the SnO_2/additive-layers.